NANOCRYSTALLINE GOLD ARYLTHIOLATE MOLECULES

A Dissertation
Presented to
The Academic Faculty

by

Ryan Cameron Price

In Partial Fulfillment
of the Requirements for the Degree
Doctor of Philosophy in the
School of Chemistry and Biochemistry

Georgia Institute of Technology
December 2006

NANOCRYSTALLINE GOLD ARYLTHIOLATE MOLECULES

Approved by:

Dr. Robert L. Whetten, Advisor
School of Chemistry
Georgia Institute of Technology

Dr. Christoph Fahrni
School of Chemistry
Georgia Institute of Technology

Dr. Angus Wilkinson
School of Chemistry
Georgia Institute of Technology

Dr. Walt DeHeer
School of Physics
Georgia Institute of Technology

Dr. Kent Barefield
School of Chemistry
Georgia Institute of Technology

Dr. Phillip First
School of Physics
Georgia Institute of Technology

Date Approved: August 23, 2006

To Melissa Arredondo

ACKNOWLEDGEMENTS

I first wish to thank the following former and current graduate students for their advice, support, and professionalism. James Bradshaw, you have been extremely supportive, great for discussing new ideas, kept me motivated these last two years, and taught me some physics in exchange for some chemistry knowledge. Dr. Richard Wyrwas, Dr. Christy Vestal, Dr. Tony Belcher, Dr. Bryan Herger, I am grateful for your advice, assistance, and friendship over the years. Dr. Kathy White, Mehmet Cetinkov, and Liqun (Ruth) Wang, I thank you for being generous with your time and the assistance you provided when needed. Melissa Arredondo, thank you for convincing me to pursue a doctoral degree with Professor Rob. Melissa, I wouldn't have made it this far without you and you are my foundation. Thankfully, the light at the end of the tunnel is finally upon us and far better times lie ahead.

The following faculty and staff members provided invaluable assistance and I am greatly indebted: Dr. Les Gelbaum, Dr. Angus Wilkinson, Dr Larry Bottomley, Dr. Christine Kranz, Dr. Mira Josowitz, and Dr. Robert Braga, Dr. Cam Tyson, and Kay Gilstrap. I would also like to thank Dr. Phil First, Dr. Jianfei Shao, and Dr. Sameh Dardona for their support and efforts to produce STM data for the quantum dots I generated. I am also most grateful to Dr. Greg Schaaff for helping me start the research within this thesis through his mentorship and collaboration. It was essential to the work contained within. Dr. Sidney Gordon, thank you for all of the advice and wisdom.

To my parents, siblings and all of my dear friends, thank you for your continued understanding of my prolonged absence, failure to return phone calls, ignored e-mails,

sporadic rants, and general malaise. This journey began in 1998 with an intended end in 2002, but like many paths, it has been winding and unpredictable. I am now ready to return to my proper role, for those who will have me back. I owe much to all of my grandparents and great-grandparents who worked so very hard to better the lot in life of their descendants while providing invaluable moral and ethical clarity that I have utilized nearly every day of my life, serving me well in the darker moments of graduate school. You are sorely missed. I'd also like to thank Charles Riner and Mary Roberson for recognizing my strong scientific curiosity at the age of 10 and patiently nurturing it throughout high school. You both provided inspiration that carried me through my undergraduate degree and beyond. Floyd Walker and Ray Gaster, thank you for nurturing a strong work ethic that kept me focused and self-motivated. Jan and Hector Arredondo, your support has been incalculably valuable for the last three months.

Lastly, Professor Rob Whetten, thank you for taking me as research assistant and believing in my ability to succeed. You were patient, did not pressure me for results, and let me explore my own ideas. This experience taught great humility and persistence when facing intellectual challenges. Although there were many failures, we can now see ways to succeed with the new knowledge gained. You expanded my perspective in ways I could not imagine five years ago. I appreciate being allowed to form my own "bigger" picture, rather than simply re-iterating another persons' pre-conceived notions. You provided intellectual freedom in the truest sense, allowing personal ownership of both success and failure, completely satisfying my deep-seated need for personal responsibility. The experience has been profound and will shape the rest of my life.

TABLE OF CONTENTS

Page

ACKNOWLEDGEMENTS iv

LIST OF TABLES ix

LIST OF FIGURES x

LIST OF SYMBOLS AND ABBREVIATIONS xiii

SUMMARY xiv

CHAPTER

1 Introduction 1

Gold Quantum Dots: A Historical Perspective 3

References 27

2 Gold:Arylthiolate Quantum Dots with 1.7 and 1.5 Nanometer Cores 32

2.1 Previous Syntheses of Gold:Arylthiolate MPCs 32

2.2 A Route to 1.7 nm and 1.5 nm Au:SPh Quantum Dots 34

2.3 Physical Properties of 1.5 and 1.7 nm $Au_x(SPh)_y$ Quantum Dots 37

2.3.1 Optical Spectroscopy 37

2.3.2 Powder X-Ray Diffraction 43

2.3.2.1 Large Angle Diffraction 43

2.3.2.2 Small Angle Diffraction 48

2.3.3 Matrix Assisted Laser Desorption Ionization MS 52

2.3.4 Elemental and Thermogravimetric Analysis 56

2.3.4.1 Elemental Analysis 56

2.3.4.2 Thermogravimetric Analysis 56

2.3.5 Proton Nuclear Magnetic Resonance 59

2.3.6 Infrared and Raman Spectroscopy 67

2.3.6.1 Infrared Spectroscopy 67

2.3.6.2 Raman Spectroscopy 71

2.4 Summary 79

References 80

3 1.1 Nanometer Core $TOA_2[Au_{44}(SPh)_{28}]$ Quantum Dots 84

3.1 Size Reduction of 1.5 and 1.7 nm $Au_x(SPh)_y$ MPCs to 1.1 nm 84

3.2 Physical Properties of $TOA_2[Au_{44}(SPh)_{28}]$ Quantum Dots 87

3.2.1 Optical Properties 87

3.2.2 Powder X-ray Diffraction 93

3.2.2.1 Large Angle Diffraction 93

3.2.2.2 Small Angle Diffraction 94

3.2.3 MALDI Mass Spectrometry of $TOA_2[Au_{44}(SPh)_{28}]$ 95

3.2.4 Nuclear Magnetic Resonance Spectroscopy 99

3.2.5 Infrared and Raman Spectroscopy 106

3.2.5.1 Infrared Spectroscopy 106

3.2.5.2 Raman Spectroscopy 106

3.3 Summary 107

References 111

4 Smaller Gold:Alkanethiolate MPCs by etching 112

4.1 Size Reduction of 2.0 $\pm$ 0.5 nm $Au_x(dodecanethiolate)_y$ MPCs 112

4.2 Optical Characterization of Etched $Au_x(dodecanethiolate)_y$ QDs 113

References 116

5 Alkanethiol Passivated 1.5 nm Gold Core Quantum Dots 117

5.1 Production of 1.5 nm $Au_x(tert\text{-}butylmercaptan)_y$ MPCs 117

5.2 Physical Properties of $Au_x(tbm)_y$ MPCs 119
5.2.1 Optical Spectroscopy 119
5.2.2 Powder X-ray Diffraction 122
5.2.2.1 Large Angle Diffraction 122
5.2.2.2 Small Angle Diffraction 122
5.2.3 MALDI Mass Spectrometry 126
5.2.4 ^{1}H NMR Spectroscopy 128
5.2.5 Infrared Spectroscopy 130
5.3 Summary 130
References 132
6 Conclusions 133
References 136
APPENDIX Presentation of Optical and X-ray Diffraction Data Presentation 137
A.1 Optical Absorbance Spectra 137
A.2 Optical Absorbance Spectra 138
References 140

LIST OF TABLES

Page

Table 2.1: ^{1}H-NMR chemical shifts, peak types, and J_H-J_H coupling constants 62

Table 2.2: IR bands observed for 1.5 and 1.7 nm $Au_x(SPh)_y$ MPCs. 70

Table 2.3: Intensity normalized Raman modes for 1.5 and 1.7 nm $Au_x(SPh)_y$ MPCs. 74

Table 3.1: Dominant bands from derivative optical spectrum of $TOA_2[Au_{44}(SPh)_{28}]$. 92

Table 3.2: ^{1}H-NMR aromatic peak assignments for $[Au_{44}(SPh)_{28}]^{2-}$. 102

Table 3.3: ^{13}C-NMR peak assignments for $[Au_{44}(SPh)_{28}]^{2-}$. 105

LIST OF FIGURES

Page

Figure 1.1: Cadmium selenide nanocrystal photoluminescence. 2

Figure 1.2: Optical spectra of various core diameter gold clusters. 4

Figure 1.3: Large Angle XRD pattern of various core diameter gold clusters. 5

Figure 1.4: STM and Coulomb staircase I-V curve at 83 K a gold MPCs. 7

Figure 1.5: DPV for small gold MPCs. 8

Figure 1.6: Highly structured optical spectrum of $Au_{75}[P(\text{-Ph-}CONHCH_3)_3]_{16}Cl_x$. 10

Figure 1.7: Optical spectrum of 5.6 kDa $Au_{28}(glutathionate)_{16}$. 10

Figure 1.8: Schematic energy level diagram for 8 kDa (~Au_{38}) gold MPCs. 11

Figure 1.9: Schematic energy level diagram for $Au_{28}(glutathionate)_{16}$. 15

Figure 1.10: Optical absorbance and photoemission for $Au_x(glutathionate)_y$ MPCs. 17

Figure 1.11: Optical spectra of arylthiolate passivated 'Au_{38}' clusters. 21

Figure 1.12: Optical Anisotropy of L and D penicillamine passivated gold clusters. 24

Figure 1.13 Schematic diagram of nuclear level shell theory applied to gold clusters. 26

Figure 2.1: Brust reaction synthetic scheme for gold MPCs . 32

Figure 2.2: Modified Brust-type scheme for $\leq$ 2.0 nm $Au_x(SPh)_y$ MPCs. 34

Figure 2.3: Optical spectra of Au_x(SPh)y MPCs compared to $Au_x(S\text{-hexyl})_y$ MPCs. 39

Figure 2.4: Derivative optical spectral plot from Figure 2.3. 40

Figure 2.5: Molar absorptivity (ε) coefficients of 1.5 and 1.7 nm $Au_x(SPh)_y$ MPCs 42

Figure 2.6: LAXRD patterns of 1.5 and 1.7 nm $Au_x(SPh)_y$ MPCs. 44

Figure 2.7:Gaussian data it to illustrative 1.5 nm LAXRD data. 45

Figure 2.8: Theoretical diffraction patterns and structural models with experimental results for 1.5 nm and 1.7 nm $Au_x(S\text{-hexyl})_y$ MPCs. 47

Figure 2.9: TEM image of ~Au_{140}(S-hexyl)$_{56}$ quantum dot with Marks decahedral structural model. 48

Figure 2.10: Logarithmic SAXRD plots for two 1.7 nm ~Au_{140}(S-alkyl)$_{56}$ MPC nanocrystalline superlattices. 49

Figure 2.11: SAXRD data for 1.5 and 1.7 nm $Au_x(SPh)_y$ MPCs. 50

Figure 2.12: STM images of 1.5 nm $Au_x(SPh)_y$ MPCs. 52

Figure 2.13: MALDI-TOF-MS of 1.5 and 1.7 nm $Au_x(SPh)_y$ MPCs. 54

Figure 2.14: TGA plots of 1.5 and 1.7 nm $Au_x(SPh)_y$ MPCs and reaction by-products. 58

Figure 2.15: ^{1}H-NMR aromatic region of 1.5 and 17 nm $TOA_N[Au_x(SPh)_y]^{N-}$. 61

Figure 2.16: Full ^{1}H-NMR of 1.5 and 17 nm $TOA_N[Au_x(SPh)_y]^{N-}$. 63

Figure 2.17: ^{1}H-NMR spectra of four ~$TOA_N[Au_{110}(SPh)_{62}]$MPC samples. 65

Figure 2.18: ^{1}H-NMR spectrum of 1.7 nm ~$TOA_N[Au_{140}(SPh)_{78}]$ clusters. 66

Figure 2.19: Infrared spectra of $TOA_N[Au_x(SPh)_y]$ MPCs with standards. 68

Figure 2.20: Raman spectra of $Au_x(SPh)_y$ MPCs with reference samples. 73

Figure 2.21: Graphical representations of benzenethiol vibrational modes. 75

Figure 2.22: Stokes and anti-Stokes Raman temperature estimation compared to TGA decomposition temperature. 78

Figure 3.1: Optical spectrum of $[Au_{44}(SPh)_{28}]^{2-}$ with similarly sized clusters. 88

Figure 3.2: Colored optical spectrum of $[Au_{44}(SPh)_{28}]^{2-}$ and its precursor. 90

Figure 3.3: Molar absorptivity coefficient plot for $[Au_{44}(SPh)_{28}]^{2-}$. 91

Figure 3.4: Derivate optical spectrum of $[Au_{44}(SPh)_{28}]^{2-}$. 92

Figure 3.5: LAXRD for $TOA_2[Au_{44}(SPh)_{28}]^{2-}$. 93

Figure 3.6: SAXRD for $TOA_2[Au_{44}(SPh)_{28}]$. 95

Figure 3.7: MALDI-MS for $TOA_2[Au_{44}(SPh)_{28}]$. 96

Figure 3.8: Fragmentation pattern for $TOA_2[Au_{44}(SPh)_{28}]$. 97

Figure 3.9: Integrated ^{1}H-NMR spectrum of $TOA_2[Au_{44}(SPh)_{28}]$. 99

Figure 3.10: Integrated aromatic ^{1}H-NMR spectrum of $TOA_2[Au_{44}(SPh)_{28}]$. 100

Figure 3.11: COSY-^{1}H-NMR spectrum of $TOA_2[Au_{44}(SPh)_{28}]$. 101

Figure 3.12: Comparison of $[Au_{44}(SPh)_{28}]^{2-}$ peaks to reference standards. 103

Figure 3.13: HSQCE ^{13}C-^{1}H-NMR spectrum of $[Au_{44}(SPh)_{28}]^{2-}$. 104

Figure 3.14: Infrared spectrum of $TOA_2[Au_{44}(SPh)_{28}]$ with reference standards. 108

Figure 3.15: Photoluminescence of $TOA_2[Au_{44}(SPh)_{28}]$ under Raman excitation. 109

Figure 3.16: Photographs of gold quantum dot dilute solutions. 110

Figure 4.1: Optical spectrum of small $Au_x(ddt)_y$ quantum dots. 114

Figure 4.2: Optical spectrum of small $Au_x(ddt)_y$ quantum dots with reference QDs. 115

Figure 5.1: Optical spectrum of ~$[Au_{122}(tbm)_{62}]$. 120

Figure 5.2: Derivative optical spectrum of ~$[Au_{122}(tbm)_{62}]$. 121

Figure 5.3: LAXRD for ~$[Au_{122}(tbm)_{62}]$. 124

Figure 5.4: SAXRD for ~$[Au_{122}(tbm)_{62}]$. 125

Figure 5.5: MALDI-MS for ~$[Au_{122}(tbm)_{62}]$. 127

Figure 5.6: ^{1}H-NMR of ~$TOA_2[Au_{122}(tbm)_{62}]$ with estimated peak integrals. 128

Figure 5.7: FTIR spectrum of ~$TOA_2[Au_{122}(tbm)_{62}]$ with reference molecules. 131

LIST OF SYMBOLS AND ABBREVIATIONS

SPh^-	benzenethiolate
CV	cyclic voltammetry
DPV	differential pulsed voltammetry
$(PhS)_2$,DPDS, or PhSSPh	diphenyldisulfide
ddt	dodecanethiol
FTIR	Fourier Transform Infrared
SG	glutathionate
LAXRD	large angle x-ray diffraction
MS	mass spectrometry
MALDI	matrix-assisted laser desorption ionization
MPC(s)	monolayer protected cluster(s)
^{1}H-NMR	proton nuclear magnetic resonance
QD	quantum dot
STM	scanning tunneling microscopy
SAXRD	small angle x-ray diffraction
tbm	tert-butylmercaptan
TOA	tetraoctylammonium
PPh_4^+	tetraphenylphosphonium

SUMMARY

This research focuses on generating, isolating, and characterizing nanophase gold clusters with diameters below two nanometers. In this size regime, the metal cores exhibit electronic and optical properties very different from those of colloidal and bulk gold, arising from quantum size confinement. The unoccupied molecular orbitals of the cores are known to accept electrons, analogous to a capacitor, but with discrete electrochemical potentials. This work describes the novel production of gold clusters with structurally rigid benzenethiolate bound to the surface, rather than typically used alkanethiolates.

The Au_x(benzenethiolate)$_y$ clusters are anionic and charged balanced by tetraoctylammonium cations. They are enriched in ~1.5 nm diameter cores, compared to a dominance of 1.7 nm cores when alkanethiols are used during synthesis. The Au_x(benzenethiolate)$_y$ clusters are more likely to form bulk crystals and degrade in polar solvents more rapidly than Au_x(alkylthiolate)$_y$ clusters. They were characterized by x-ray diffraction, carbon and proton NMR, FTIR, optical spectroscopy, mass spectrometry, elemental analysis, and thermogravimetric analysis.

The etching of clusters in the presence of hydrogen peroxide and excess benzenethiol to yield smaller 1.1 nm clusters is reported for the first time in this work. These 1.1 nm clusters have a rich optical spectrum with clear electronic transitions at room temperature and orient spontaneously when deposited from solution. This oxidative etching process was applied to alkanethiolate clusters, converting ~2.0 nm polydisperse clusters into smaller clusters. This offers the potential to produce smaller gold clusters with more available charge states and may increase the variety of thiols that can be bound to the surface of gold monolayer protected clusters (MPCs), known also as quantum dots.

The use of the bulky thiol, tert-butylmercaptan to produce 1.5 nm core gold clusters is also reported, indicating sterically hindered alkanethiols can play a role in limiting the size of Au_x(alkylthiolate)$_y$ clusters. These clusters were characterized by x-ray diffraction, proton NMR, FTIR, optical spectroscopy, and mass spectrometry. The clusters are potentially useful for thiolate exchange reactions to produce new types of Au_x(thiolate)$_y$ clusters.

CHAPTER 1

INTRODUCTION

The science behind the current publication frenzy describing nanometer scale materials can be traced to the preparation of II-VI semiconductor crystallites with dimensions below five nanometers in the late 1980's.[1,2] The cadmium selenide clusters obtained by these and subsequent methods contain fewer structural units than required to give rise to the conduction and valence bands present in bulk cadmium selenide. From the perspective of solid-state inorganic chemistry, the explanation of the novel optical and electronic properties of these materials follows.

Bulk semiconductors absorb light, moving an electron from a filled (valence) band to an empty (conduction) band. The energy difference between the valence and conduction band is typically called the bandgap. Lattice periodicity within the semiconductor allows an excited electron transferred into the conduction band to delocalize, leaving a positively charged vacancy (hole) in the valence band. The electron and hole are delocalized over several lattice sites and are mobile within the crystal lattice. If the photon energy used to generate this electron-hole pair, known as an exciton, is at or below the band gap of the material, these two charge carriers remain electrostatically bound. The exciton can be described by a wave function resembling a hydrogen atom, with a characteristic Bohr radius. The exciton diameter depends on the nature of the material and is approximately 10 nanometers in bulk CdSe. Exciton mobility is lowered somewhat on the scale of tens of nanometers mainly from localized surface defects, but when crystallite size is lower than the exciton diameter, the exciton total energy significantly increases. At this point, its hydrogen-like wave function is confined,

increasing exciton creation energy. This phenomenon is known as quantum confinement, as the energy shift is explicitly a function of the quantum mechanical nature of the exciton wave function. Experimental and theoretical results both indicate that this energy varies linearly with the inverse square of crystallite radius. In CdSe, these effects occur in crystals with diameters below 10 nm. Photoluminescence emission from a series of <10 nm CdSe crystallites are shown in Figure 1.1, showing the quantum confinement effect.

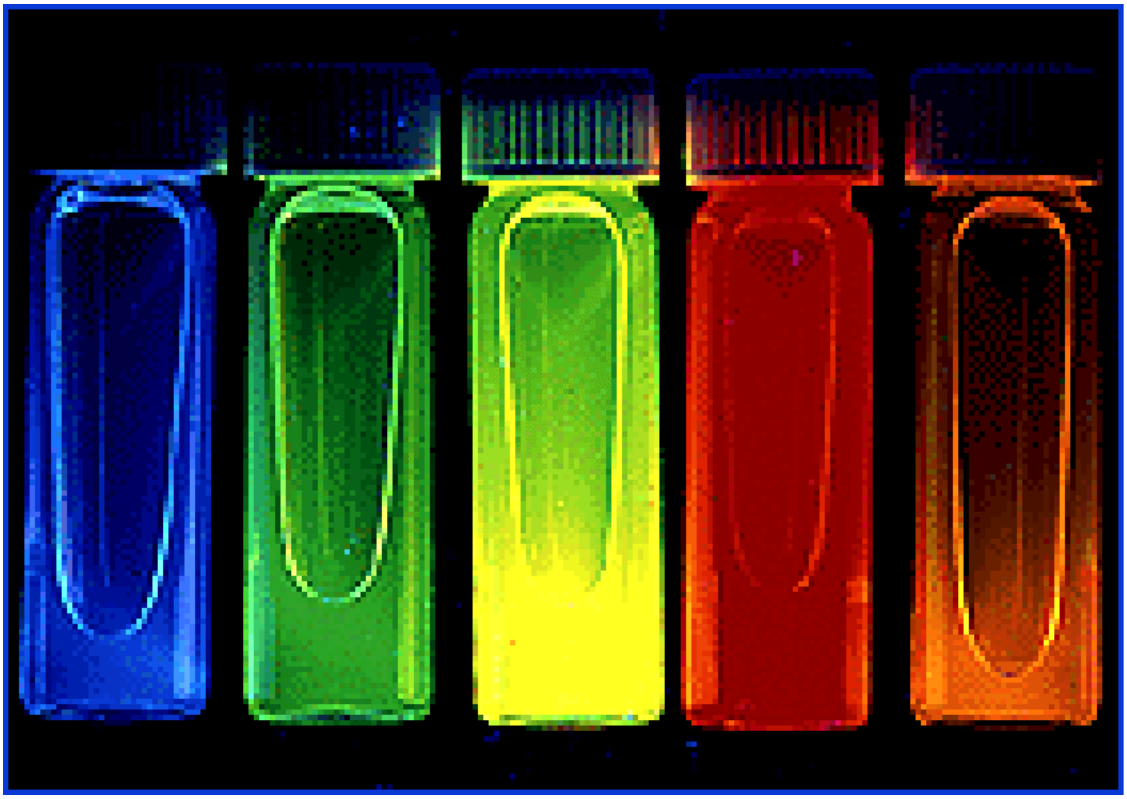


Figure 1.1 Cadmium selenide nanocrystal photoluminescence at diameters from ~1.5 nm (left) to ~6.0 nm (right).[3] The increased exciton energy gives rise to a blue shift (Anti-Stokes shift) in photoluminescence emission energy as crystallite diameter decreases.

Crystallites of this type can be synthesized by controlling their nucleation and growth. Each crystallite has interior structure and bonding similar to bulk CdSe. Crystal structures have even been determined for 1.2 nm core diameter $Cd_{32}S_{14}(SPh)_{36}$*DMF_4 nanocrystallites and 1.0 nm fullerenes (C_{60}), representing prototypical examples of discrete, well-defined nanophase materials with specific molecular compositions.[4,5]

Gold Clusters with Discrete Compositions

Gold Quantum Dots: A Historical Perspective

In 1857, Michael Faraday published the first scientific paper discussing nanoscale effects in colloidal gold.[6] Numerous methods exist for producing colloids of this type with average diameters ranging from 5 to 100 nm. The colloidal solutions are typically vibrant blue to violet color at millimolar concentrations and a light rose-red hue at lower concentrations. Colloidal gold was even used in the Middle Ages for coloring glass, but it was not until 1971 to 1980 that molecular scale, air-sensitive gold clusters were reported with the compositions $Au_{8\text{-}11}(P\text{-}Aryl_3)_xCl_y$.[7-9] Similar, larger clusters with the compositions $[Au_{13}(PPhMe_2)_{10}Cl_2](PF_6)_3$ and $Au_{55}(PPh_3)_{12}Cl_6$ were subsequently generated in 1981.[10,11] In 1993 molecule-scale $Au_x(alkylthiolate)_y$ monolayer protected clusters (MPCs) were chemically prepared and characterized as metastable solids.[12] The next year air-stable, organic solvent dispersible, alkanethiolate passivated gold MPCs with core diameters from one to three nanometers were reported, providing a prototypical synthetic method still employed by most researchers to date.[13] This two-phase liquid-liquid methodology was modified in 1996, narrowing the cluster core size distribution and allowing size separation of the products through fractional crystallization.[14] Mass spectrometric analysis of the separated products revealed discontinuous core masses, indicating the possibility of thermodynamically optimal cluster compositions, rather than random distributions of core sizes.

Subsequent optimization of this synthesis in 1997 produced a narrower crystallite core size distribution of one to three nanometers. This series of $Au_x(alkylthiolate)_y$ MPCs

were separated and isolated by fractional crystallization with each fraction possessing distinct mass spectroscopic, optical, and powder x-ray diffraction properties.[15 – 18] Specifically, below two nanometers diameter, the gold core masses occurred at 28 kDa, 22 kDa, 14 kDa, and 8 kDa, corresponding to core diameters of ca. 1.78 nm, 1.48 nm, 1.32 nm, and 1.09 nm, respectively. This work included the first mention of tuning cluster diameter by controlling the reaction temperature.[18] Figure 1.2 and Figure 1.3 compare the unique optical spectra and powder diffraction patterns these materials possess relative to bulk gold. The figures clearly show the divergence of nanocrystallite properties from the bulk with decreasing core diameter.

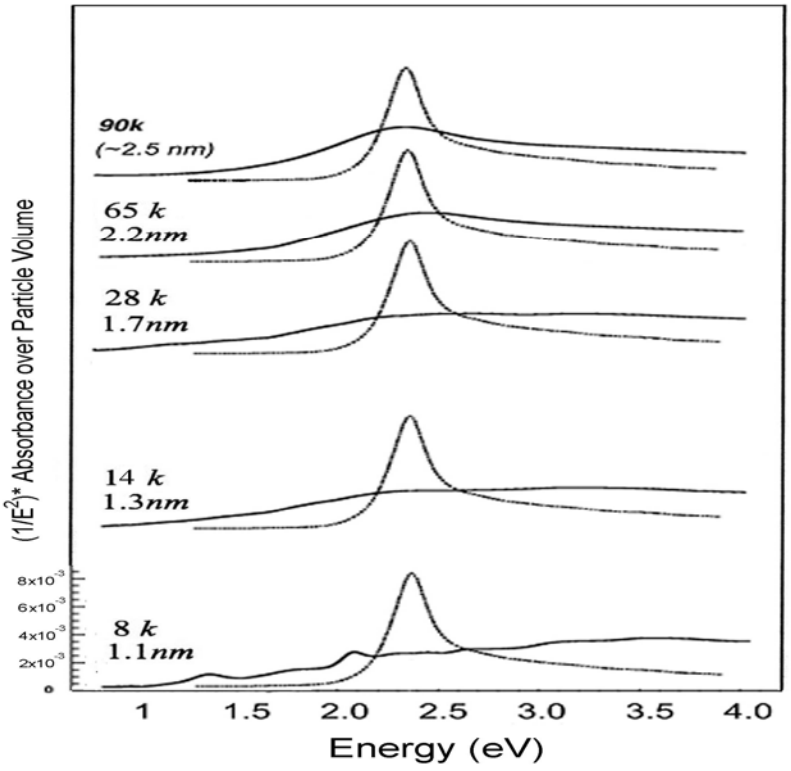


Figure 1.2 Optical spectra of various core diameter gold clusters. Each spectrum is referenced to 30 nm colloidal gold. Note the increasing number of inflection points at 1.7 nm diameter and below.

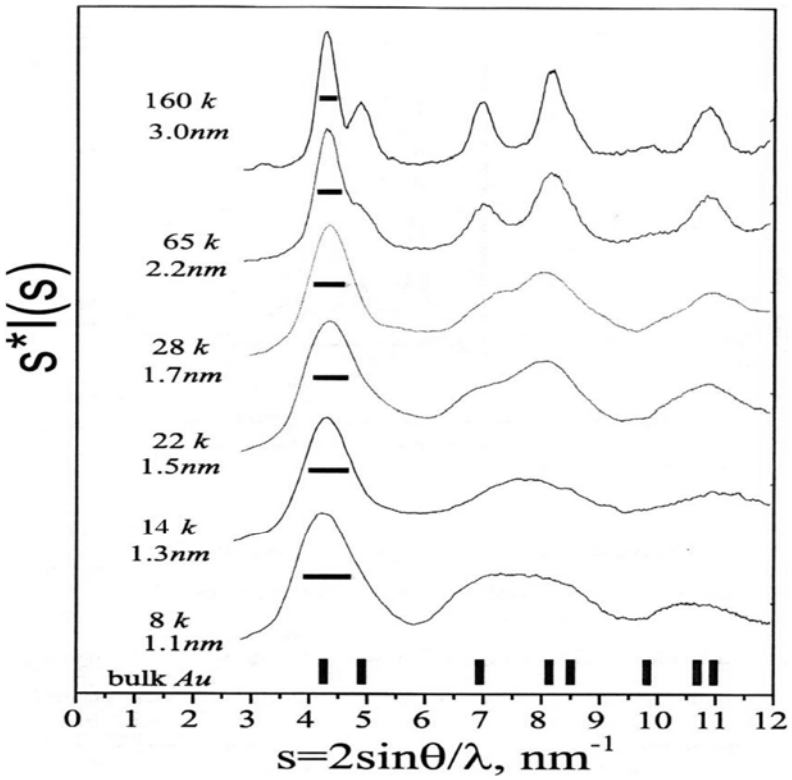


Figure 1.3 Large Angle XRD pattern of various core diameter gold clusters. The horizontal bars on each pattern indicate the peak width expected from the Debye formula for small crystalline spheres. Figure adapted from reference 17.

The optical spectra in Figure 1.2 are indicative of quantum size effects on the electronic structure of the gold core. This was verified in 1997 for 1.9 nm diameter clusters by subpicosecond transient absorption spectroscopy, revealing electronic energy level spacings of 60 meV.[19] These energy gaps are nearly *three* times the 26 meV thermal energy present at room temperature. This same year, *six* discrete, reversible electronic charging states known as a "Coulomb staircase" for a purified 1.68 nm core ~Au_{140}(hexanethiolate)$_{56}$ cluster at 83 K were detected by scanning tunneling microscopy (STM). [20] Cyclic (CV) and differential pulsed voltammetries (DPV) of this cluster revealed *ten* distinct, reversible charge states. Figure 1.4 shows this phenomenon.

In 1998, differential pulsed voltammetry of the three smallest core diameter $Au_x(S\text{-}alkyl)_y$ MPCs (8 kDa, 14 kDa, and 22 kDa) indicated an increased HOMO-LUMO gap with decreasing core sizes, further validating size quantized properties in small gold MPCs.[21] Figure 1.5 shows the DPV of the aforementioned molecules. During this same period, highly ordered superlatttice arrays of size-fractionated $Au_x(S\text{-}alkyl)_y$ MPCs with the gold cores organized as body centered cubic or face centered cubic arrays were evaluated.[22] Interdigitation of alkanethiolate hydrocarbon chains under suitable drying conditions gave rise to this self-organization. A concurrent study of $Au_x(dodecanethiolate)_y$ MPC formation across a range of temperatures and thiol concentration during cluster formation placed size-tuning via temperature control on a firmer experimental basis for future research.[23] Lastly, small5.5 kDa (0.9 nm core) $Au_x(\text{-glutathionate})_y$ MPCs with the formulation $Au_{28}(\text{-glutathionate})_{16}$, isolated by polyacrylamide gel electrophoresis chromatography (PAGE) were reported in 1998. Notably, this MPC had a slightly more structured optical spectrum and higher energy bandgap than 8 kDa $Au_x(alkylthiolate)_y$ MPCs, further revealing a trend of increased bandgap with decreasing core size for gold clusters.[24]

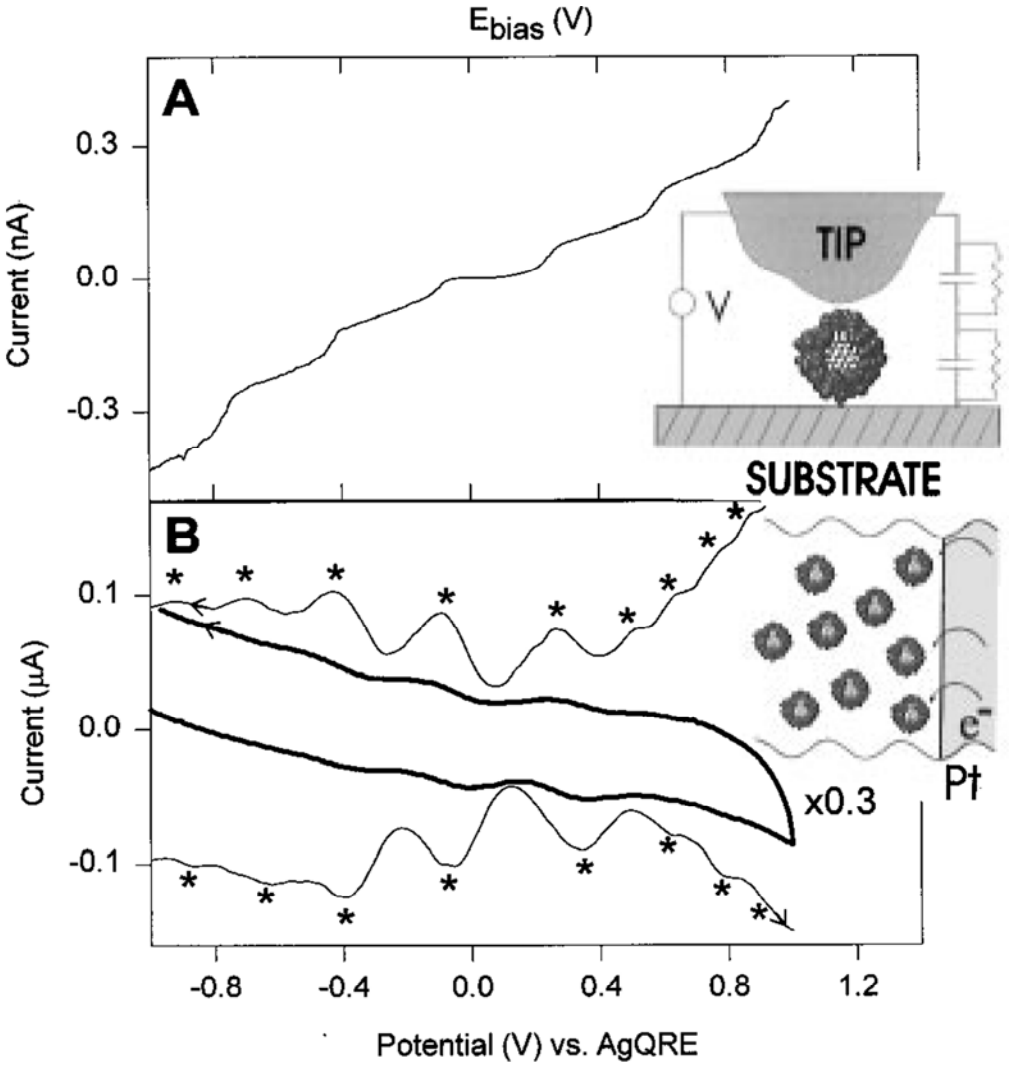


Figure 1.4 Panel A: Au STM tip addressing a single cluster adsorbed on an Au-on-mica substrate (inset) and Coulomb staircase I-V curve at 83 K; potential is tip-substrate bias; equivalent circuit of the double tunnel junction gives capacitance C_{upper} = 0.59 aF and C_{lower} = 0.48 aF. Panel B: Voltammety (CV —, 100 mW/s; DPV ■■ , * are current peaks, 20 mV/s, 25 mV pulse, top and bottom are negative and positive scans, respectively) of a 0.1 mM 28 kDa cluster solution in 2:1 toluene:acetonitrile/ 0.05 M Hx_4NClO_4 at a 7.9 x 10^{-3} cm^2 Pt electrode, 298 K, Ag wire pseudoreference electrode. (Reproduced from Reference 20)

Further insights into discrete charging behavior and compositions of gold MPCs were reported in 1999 and 2000. Study of the electrochemical charging properties for purified 1.68 nm ~Au_{140}(hexanethiolate)$_{56}$ MPCs showed electrochemical charge preservation after solvent removal. Subsequent re-dispersion allowed oxidation of ethyl ferrocene by positively charged MPCs and reduction of tetracyanoquinodimethane by

negatively charged MPCs.[25] This offered the possibility of gold MPCs as flexible electron transfer reagents, arising from their wide number of available charge states.[20] Subsequent work with this 1.68 nm MPC as a thin solid film characterized the bulk conductivity and electron self-exchange rate constants between multivalent clusters with charges differing by one electron.[26] Electron exchange rates were on the order of 10^8 – 10^{10} $(M*s)^{-1}$, increasing as the ratio of oxidized to reduced clusters increased in the film.

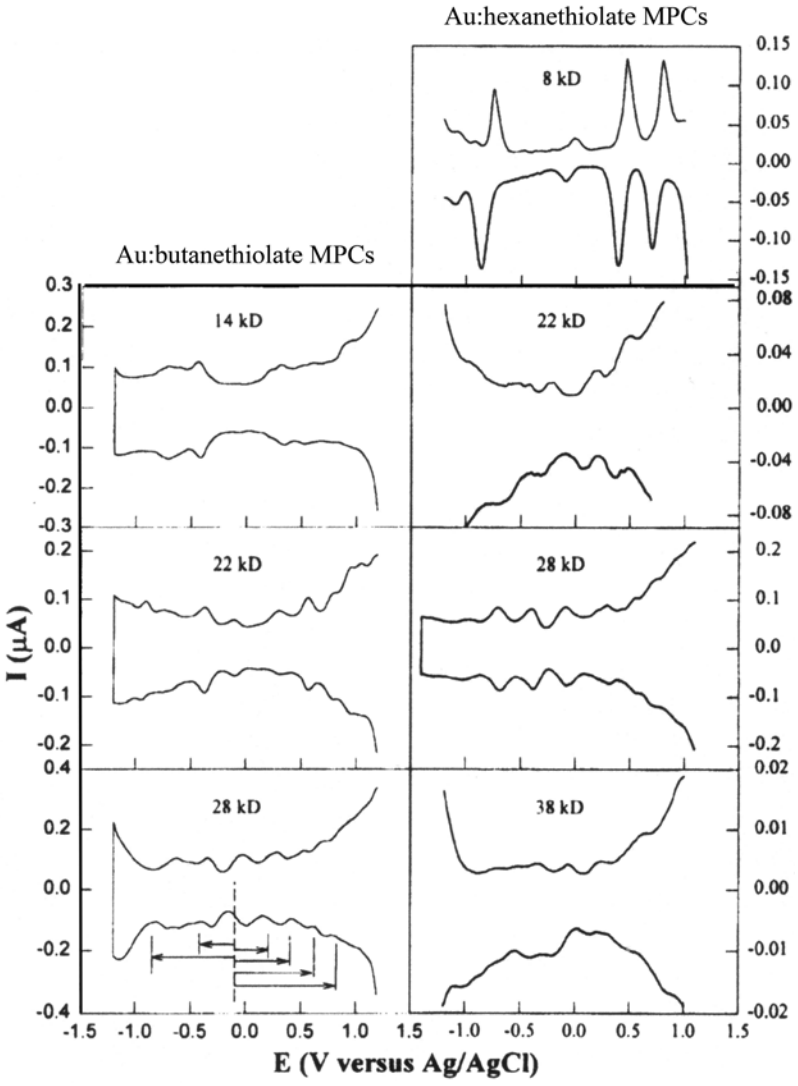


Figure 1.5 DPV for small gold clusters. The number of detectable charge states decreases with decreasing diameter, while the charge state spacing increases, becoming highly pronounced at 14 kDa and 8 kDa. Image adapted from reference 18.

The conductivities ranged 49 $M\Omega^{-1}cm^{-1}$ to 2.2 $k\Omega^{-1}cm^{-1}$, values 3 to 140x greater than silicon (15.6 $M\Omega^{-1}cm^{-1}$) and $200x10^6$ to $9x10^9$ times below bulk gold (.452 $\mu\Omega^{-1}cm^{-1}$). This could be interpreted as an initial demonstration for device applications, but MPC patterning and electronic addressing are still lacking.

This same period, electronic states for a ~Au_{140}(hexanethiolate)$_{56}$ cluster were evaluated at cryogenic temperatures by STM. Charging events from $\pm$3 electrons were studied at 300 K, 77 K, and 8 K. Electronic state quantization was observed as a Coulomb staircase with electronic fine structure evident between discrete charge states[27], revealing energy level spacings below the charging energy of the accessible charge states and pointing further towards smaller sizes yielding higher energy available charge states. A 1.3 nm MPC of composition $Au_{75}[P(\text{-Ph-}CONHCH_3)_3]_{16}Cl_x$ was concurrently reported to possess a highly structured optical spectrum, shown in Figure 1.6.[28] This structured optical spectrum indicated larger energy gaps between electronic states than found in 1.7 nm clusters. Larger energy gaps at smaller gold MPC sizes were also found in a series of Au_x(L-glutathionate)$_y$ MPCs with 4.3, 5.6, and 8.2 kDa cores (20 – 40 atoms) having optical bandgaps (absorbance onsets) at 1.7, 1.3, and 1.0 eV, respectively.[29] Discrete optical transitions of the 5.6 kDa Au_{28}(L-glutathionate)$_{16}$ MPCs are shown in Figure 1.7. The Au_x(glutathionate)$_y$ MPCs also displayed optical chirality (Cotton effect) attributed to the inherently chiral L,L-glutathionate passivant modifying the metallic core symmetry. This unique observation of optical activity in large metal clusters, possibly arising from chirality in the metallic core has remained largely unexplored.

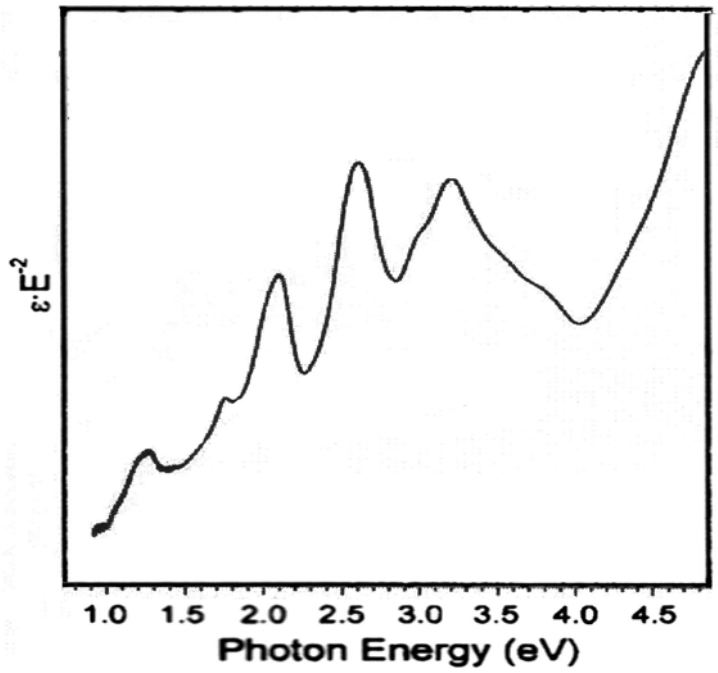


Figure 1.6 Highly structured optical spectrum of $Au_{75}[P(\text{-}Ph\text{-}CONHCH_3)_3]_{16}Cl_x$. Spectrum adapted from reference 28.

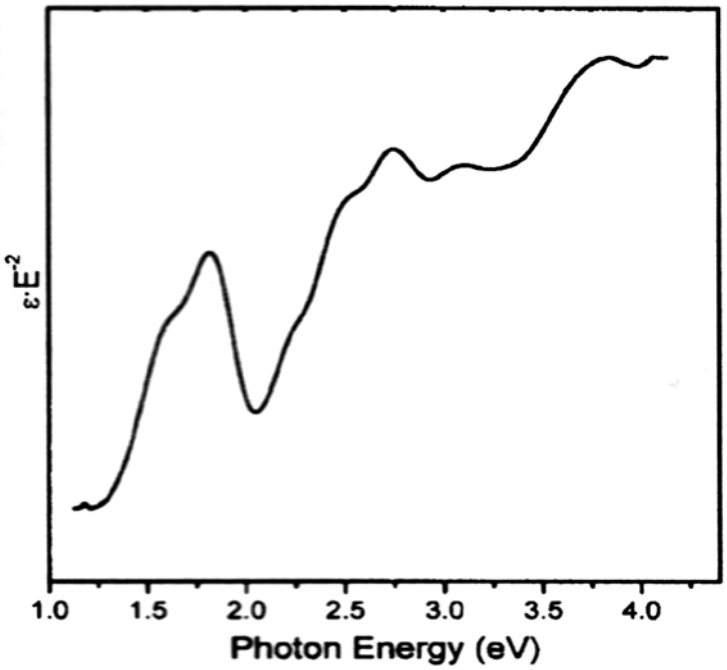


Figure 1.7 Optical spectrum of 5.6 kDa $Au_{28}(glutathionate)_{16.}$ Fewer states with larger energy gaps are evident when compared to Figure 1.6. Spectrum adapted from reference 29.

Another benchmark optical phenomenon reported that year was near-infrared luminescence of solvated 8 kDa (1.1 nm) and 28 kDa (1.7 nm) Au_x(dodecanethiolate)$_y$ MPCs upon irradiation with a 1.165 eV laser.[30] Both clusters emit broadly in the near IR from at least 0.7 eV to 1.165 eV (the lower and upper detection limits of the experiment). The smaller 8 kDa clusters display less emission at lower energies, providing additional evidence of a larger electronic bandgap with decreasing cluster size. Figure 1.8 shows a schematic representation of the discrete electronic states of small clusters and presents an energy level diagram for intraband excitation and emission of discrete gold clusters.

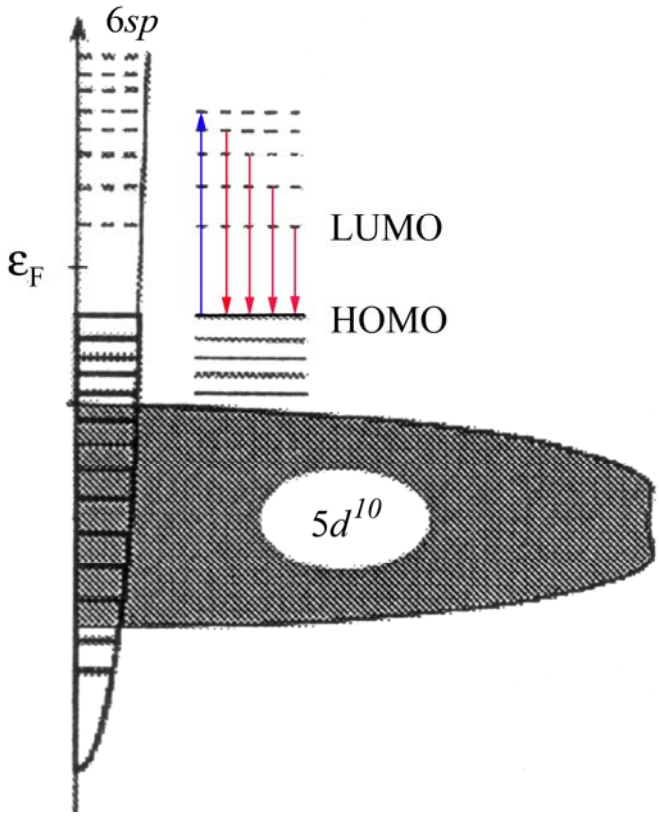


Figure 1.8 Schematic energy level diagram for 8 kDa (~Au_{38}) gold MPCs. Valence (6sp) electrons occupying the HOMO are slightly below the Fermi energy (ε_F), while the LUMO energy exceeds ε_F. The number and degeneracy of states available are dependent on the number of atoms *and* their geometry.[27] Intraband excitation is indicated in blue and emission in red. Figure adapted from reference 30.

Also in 2000, a simple synthetic method for a 20 kDa (1.5 nm) Au:triphenylphospine MPC with the approximate composition $Au_{101}(PPh_3)_{21}Cl_5$ was reported.[31] This method offered a potential thiol alternative for gold MPC production and a direct route to a specific size of cluster without the need for extensive purification. Unfortunately, this Au:triphenylphosphine MPC has not been characterized by electrochemical (CV and DPV), STM, and/or mass spectrometry.

In 2001, luminescence from aqueous 1.8 $\pm$ 1.0 nm (~Au_{201}) polydisperse gold MPCs passivated with 3-mercaptosuccinic acid (MSA) , tiopronin (TP) , and 3-mercapto-1-propanesulfuric acid(MPSA) was studied. Interestingly the materials displayed differing emission maxima.[32] The maxima for MSA, TP, and MPSDA were 2.36 eV, 2.61 eV, and 1.68 eV, respectively. This demonstrated the possibility of varying surface passivant composition on gold MPCs to tune emission wavelength. The possibility of ligand to metal charge transfer (LMCT) playing a role in the emission of gold MPCs was also suggested.

Additional work with passivant effects this same year revealed dialkyldisulfides could produce the same small (1.4 – 2.8 nm) core diameter gold MPCs under the same reaction conditions that normally utilize alkanethiols.[33] While no new insight was gained into the precise nature of the gold-thiolate interaction in MPCs, this work revealed 12-mercapto-1-dodecanol [$HS(CH_2)_{12}OH$] to be thermodynamically favored (by 90 %) over the dodecanethiol in exchange reactions between equimolar solutions of the two compounds and Au_x(dodecanethiolate)$_y$ MPCs. Cluster formation from the [Au(I):dodecanethiolate]$_x$ polymeric complex in the presence of [$HS(CH_2)_{12}OH$] also resulted in clusters predominantly (97 %) passivated this ω-hydroxyalkanethiolate . This

indicated complete degradation of the intermediate [Au:alkanethiolate]$_x$ polymer reactant during cluster generation and suggested thermodynamics govern cluster formation with thiol solubility in the reaction solvent lending a partial role. A kinetic product resulted with nearly a 1:1 molar ratio of ω-hydroxyalkanethiolate to alkanethiolate on the MPC surface when the asymmetric disulfide, $CH_3(CH_2)_{11}SS(CH_2)_{12}OH$ was present during gold MPCs formation. This product, rather than the thermodynamically favored ratio of 97:3 in the monolayer demonstrated yet another available technique for tailoring the surface chemistry of gold MPCs.

The strong influence of highly charged surface species on the electronic structure of the metallic core of gold MPCs was characterized this same year.[34] The prototypical gold MPC,[11] $Au_{55}(PPh_3)_{12}Cl_6$ was verified by x-ray photon spectroscopy (XPS) and ultraviolet photon spectroscopy (UPS) to undergo an insulator to metallic transition upon removal of the chloride anions by UV radiation. This effect was attributed to the high electronegativity of chlorine relative to gold and should be diminished or absent for thiolates on gold.

In 2002 significant insights were reported on ligand exchange reactions, luminescence properties, and the available electrochemical charge states of gold MPCs. Enchanced ligand exchange rates and exchange extent of 6-mercapto-1-hexanol [$HO(CH_2)_6SH$] onto1.7 nm ~Au_{140}(hexanethiolate)$_{56}$ clusters with increasing positive electrochemical charging of the cores were identified for the first time.[35] Only 19 % of the hexanethiolates on gold MPCs with charge –1 were exchangeable, while 45 % could be exchanged on MPCs at charge state +2. A maximum of ~25 ligands were exchangeable on the MPCs, a value near the 20 facial or 30 edge sites the MPCs are

believed to possess, suggesting higher ligand lability at one of these sites. The exchange reaction rate was dependent on incoming ligand concentration, indicative of an associative reaction mechanism, similar to that observed for larger, colloidal $Au_x(alkylthiolate)_y$ MPCs.[36] Generation of potassium thiolates via inclusion of the strong base potassium hydroxide enhanced the exchange rate by over twenty-fold, while acetic acid slowed the reaction. This revealed thiolates to be more reactive than thiols in exchange reactions. Inclusion of oxygen in the exchange reactions enhanced the exchange rate for negatively charged MPCs. This was reasonably attributed to reduction of oxygen by anionic clusters, with incoming thiols acting as proton donors, forming peroxide and thiolate at the cluster surface. The thiolate generated in proximity to the surface then binds to the gold MPC core, displacing some of the original protective monolayer. This insight provided an enhanced understanding of surface modification reactions for $Au_x(thiolate)_y$ MPCs.

Also in 2002, dodecanethiolate ligand exchange onto the sub-nanometer cluster $Au_{11}(PPh_3)_8Cl_3$ (undecagold)^8 established a lower size limit for Au:thiolate MPCs.[37] Study of this 0.8 nm diameter cluster should reveal a simple density of states and provide a more complete understanding of the emergent electronic structure between the atomic and molecular scale for gold. This substitution reaction also overcame the known stability issues of $Au_x(phosphine)_yCl_z$ MPCs.

The luminescence properties of the $Au_{28}(glutathionate)_{16}$ MPC reported in 2002 showed two distinct luminescence emission maxima with unprecedented quantum efficiencies on the order of 10^{-3} upon excitation at 2.48 eV (500 nm).[38] Two emission features were evident. There was a high energy emission at 1.5 eV attributed to interband

d-sp transitions with quantum efficiency of .0015±.0005, and a low energy emission at 1.15 eV with quantum efficiency .0020±.0006 assigned to intraband sp-sp transitions. Both of these processes are shown in Figure 1.9. The possibility of ligand to metal charge transfer (LMCT) giving rise to the low energy emission was also postulated for consideration, but has not been conclusively verified or disproved to date.

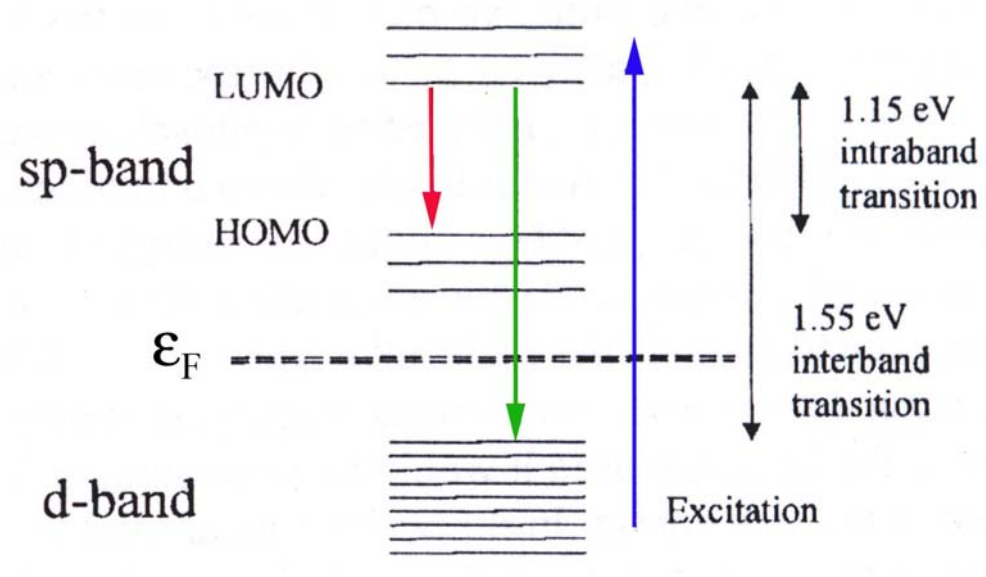


Figure 1.9 Schematic energy level diagram for 5.6 kDa Au_{28}(glutathionate)$_{16}$ MPC. Excitation is indicated in blue, the high-energy luminescence in green and the low energy emission in red. The Fermi energy (ε_F) lies *below* the HOMO-LUMO gap, unlike the larger 8 kDa cluster shown in Figure 1.8. Figure adapted from reference 38.

Electrochemical measurements this same year by cyclic and differential pulsed voltammetries (CV and DPV) of highly purified 1.7 nm Au_{140}(hexanethiolate)$_{56}$ MPCs found an unprecedented 13 discrete, available charge states ranging from –6 to +7 on the cluster cores at –17 ^{0}C.[39] The charge states of three and higher from the as-synthesized charge state of the clusters required considerably higher voltages to obtain, once more strongly suggesting non-classical, quantized charging consistent with a molecular bandgap. The 26 meV charging voltage observed for the highest charge state agrees

closely with the reported 30 meV bandgap reported for this cluster, further indicating the 1.7 nm core diameter gold MPC as the largest cluster of the gold quantum dot family.

While 2003 was slow relative to other years concerning new information about gold MPCs, a report of two additional accessible charge states on 1.7 nm Au_{140}(hexanethiolate)$_{56}$ clusters did emerge, bringing the total known charge states to 15 and further showcasing their electrochemical utility.[40] A simple, one-phase, aqueous synthesis for $Au_{10\text{-}13}$(dimercaptosuccinate)$_{6\text{-}8}$ clusters by merely combining $HAuCl_4$ and meso-2,3-dimercaptosuccinc acid [$HCO_2CH(SH)CH(SH)CO_2H$] in water was also reported, providing a convenient method to generate the smallest gold MPCs possessing rich, structured optical spectra.[41] A theoretical study this year indicated low symmetry chiral gold clusters with 28 to 75 atoms may possess energies only .13 to .39 eV/cluster greater than higher symmetry core structures, such as I_h, O_h, and T symmetries.[42] This provided theoretical insight regarding previously observed chiral gold clusters.[29]

Novel procedures for generating and isolating gold MPCs below two nanometers in diameter and insights into their properties were reported in 2004. A modification of previous methods generated $Au_x(PPh_3)_yCl_z$ clusters ranging from 0.8 to 3.0 nm in diameter with $Au_{20}(PPh_3)_8^{2+}$ detected by mass spectroscopy, ostensibly from the parent complex $Au_{20}(PPh_3)_8Cl_2$.[43] This presumably tetrahedral cluster was previously only generated in the gas phase, is composed *entirely* of surface atoms, and is exceptional in its high optical bandgap of ~ 1.7 eV.[44] The $[Au_{20}(PPh_3)_8]^{2+}$ dication is an 18 electron species, representing a major shell closing (S,P,D shells) in the electron shell model for metal clusters.[45] An additional advance in $Au_x(PPh_3)_yCl_z$ MPC chemistry was ^{31}P-NMR detection of a rapid loss and exchange of a single PPh_3 in solution from the

$Au_{101}(PPh_3)_{21}Cl_5$ cluster[31], providing new insight into the chemistry of this cluster.[46] The site opened during this exchange could possess catalytic or chemical activity.

This was also the year that deeper insights into the compositions and optical properties of $Au_x(glutathionate)_y$ MPCs[29] were resolved by electrospray ionization massspectrometry (ESI).[47] Cluster compositions of $Au_{18}(glutathionate)_{12}$, $Au_{21}(glutathionate)_{12}$, $Au_{25\pm1}(glutathionate)_{14\pm1}$, $Au_{28}(glutathionate)_{16}$, $Au_{32}(glutathionate)_{18}$, and $Au_{39}(glutathionate)_{23}$ were isolated, each possessing unique, structured optical absorbance and photoluminescence with quantum yields on the order of 10^{-4} to 10^{-3}, shown in Figure 1.10. This work further emphasized the size dependent nature of gold MPC optical properties.

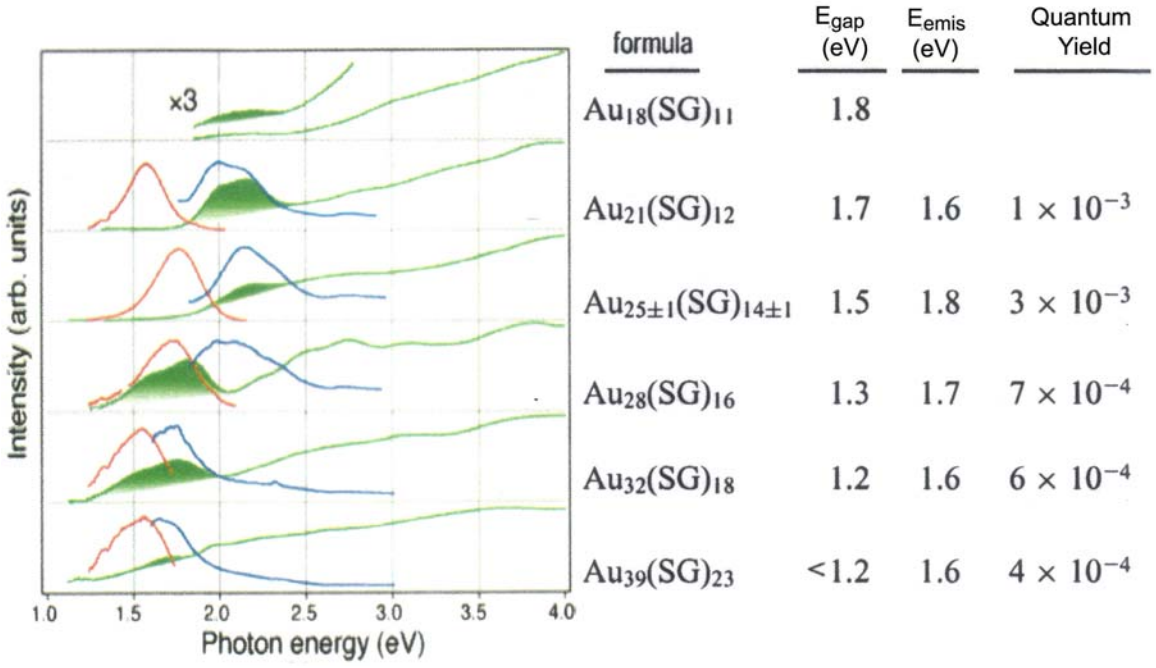


Figure 1.10 Optical absorbance (green), photoemission (red) and photoexcitation (blue) for gold:glutathionate MPCs. Molecular compositions and optical data are tabulated to the right. Figure adapted from reference 47.

One to two nanometer gold clusters generated via reduction of aqueous $HAuCl_4$ in the presence of poly-amidoamine (PAMAM) dendrimers, as templating agents, were also

reported in 2004.[48] Interestingly, controlling the molar ratio of gold to dendrimer during cluster formation appeared to govern whether Au_{55}, ~Au_{100}, or Au_{140} clusters were formed within the dendrimer, evidenced by optical and transmission electron microscopy (TEM). The quantities of material produced are currently on the microgram scale, and milligram quantities are desirable for XRD and MS characterization. A further extension of this work demonstrated the extraction of the gold clusters from the dendrimers by simply adding toluene solvated alkanethiols to yield organic soluble $Au_x(alkylthiolate)_y$ MPCs, with the dendrimer template subsequently purified and regenerated for re-use.[49]

Further refinement of the Brust-type synthesis[13] for $Au_x(thiolate)_y$ MPCs employing low temperatures and/or massive excesses of thiols produced considerable (~250 mg) yields of 1.1 nm core diameter $Au_x(hexanethiolate)_y$ and $Au_x(SC_2H_2Ph)_y$ MPCs with compositions of ~$Au_{38}(thiolate)_{24}$.[50,51] Both materials had structured optical spectra, a 1.33 eV electronic bandgap, and electrochemical charging properties similar to previously isolated 8 kDa $Au_x(hexanethiolate)_y$ MPCs.[21] Additionally, the optical absorbance intensity depletion as a function of oxidation for these MPCs was collected for the +1 and +2 oxidation states, showing the removal of electrons from their HOMO.[52] The surface ligand exchange kinetics of larger 1.7 nm ~$Au_{145}(SC_2H_4Ph)_{53}$ MPCs produced in situ with the 1.1 nm clusters of this type showed at most 53 % exchange by para-substituted benzenethiols in solution. This finding once more suggested enhanced lability at specific sites on the cluster core.[53] The exchange rates for electron donating para moieties (such as NO_2 and CN) were three to four times faster than electron withdrawing species (such as OCH_3 and OH). This further enhanced the understanding of

gold MPC surface chemistry, and may prove vital for forming nanoparticle arrays or sensors.

In 2005, many new insights into passivant monolayer effects on $Au_x(thiolate)_y$ MPC properties were described. A luminescence study of Au_{201}, Au_{145}, Au_{38}, and Au_{11} MPCs showed similar broad emission for all of these materials from ~ 0.9 to 1.8 eV with emission intensity dependent upon the nature of thiolates or charged species bound to the metal core.[54] The similarity of the spectral widths was proposed to arise from localized surface states that are independent of the core size. Validation of this hypothesis was shown by consistently increased or induced photoluminescence upon substitution of charged moieties, such as trimethyl-(mercaptoundecyl)ammonium, tiopronin, mercaptopolyethyleneglycol, and even chloride into the aliphatic monolayer of the clusters. Despite possessing ~ 20 gold atoms, clusters of composition $\sim Ag_{125}Au_{20}(tiopronin)_{33}(t\text{-butylbenzylthiolate})_{20}$ displayed photoluminescence similar to known Au_{140} MPCs. The clusters were generated by exchange reactions of Au(I)[*para*-t-butylbenzylthiolate] with $Ag_{145}(tiopronin)_{53}$ and they provided strong evidence for discrete surface state emission from metallic MPCs.[55] Similar surface-state phenomena are well known for semiconductor quantum dots.[56]

Exchange rate studies of para substituted benzenethiols onto $\sim Au_{145}(SC_2H_4Ph)_{53}$ and $\sim Au_{38}(SC_2H_4Ph)_{24}$ MPCs found faster exchange rates for electron withdrawing moieties and little core size dependence on exchange rate.[57] The exchange rates for the two clusters with the same benzenethiolate were on the same order of magnitude and within 35 % of one another. The largest rate difference occurred for 4-bromobenzenethiol with a rate of .0034 $M^{-1}s^{-1}$ for the $\sim Au_{38}$ cluster and .0022 $M^{-1}s^{-1}$ for the $\sim Au_{145}$ cluster.

The relative exchange rates followed the order NO_2 > Br > CH_3 for both clusters and were reversible, but the reverse rates were about four times slower. This lower rate implied enhanced stability of Au_x(arylthiolate)$_y$ MPCs by an estimated 35 meV per cluster.

These exchange reactions allowed the production and electrochemical characterization of ~Au_{38}(SPh-X)$_{24}$ MPCs with X = NO_2, Br, H, CH_3, and OCH_3.[58] Interestingly, the energy spacing between charge states and HOMO-LUMO gap of the MPCs were insensitive to differing benzenethiolates. The absolute potentials of the charge states were varied relative to benzenethiolate, with shifts to more positive potentials for electron withdrawing substituents (NO_2 and Br) and to more negative potentials for electron donating species (CH_3 and OCH_3). Each ~$Au_{38}(SC_2H_4Ph)_{24-y}$(S-aryl)$_y$ MPC possessed a distinct optical spectrum relative to ~$Au_{38}(SC_2H_4Ph)_{24}$ MPCs. The optical spectra of these MPCs are shown in Figure 1.11. Such seemingly simple systems reveal a great deal of complexity in their optical and electronic properties, demonstrating how the electronic properties of MPCs can be altered and potentially tailored by the protecting ligands.

The complex interactions of the core charge and ligand electronic environment for ~Au_{145}(hexanethiolate)$_{53}$ and ~$Au_{38}(SC_2H_4Ph)_{24}$ MPCs were investigated by monitoring ligand ^{13}C-NMR spectra at increasing oxidation states up to positive three.[59] Both clusters exhibited coalescence of distinct chemical shifts at +1 charge and complete merging to one broad spectral feature at +2 charge state. The ~Au_{145}(hexanethiolate)$_{53}$ MPCs initially possessed a series of closely spaced chemical shifts indicating numerous aliphatic carbons, while the $Au_{38}(SC_2H_4Ph)_{24}$ MPCs clearly showed two distinct chemical environments for the 2-phenylethanethiolate before oxidation. Rapid inter or intra cluster

exchange between magnetically nonequivalent sites was unlikely for both clusters, as the necessary rate would be ~10^5 faster than known ligand exchange rates[33,35,57] to yield the observed resonances on the timescale of NMR signal collection. The source of the chemical shift coalescence effect remains unknown, but clearly shows the influence that core charging can have on the electronic and magnetic properties of a ligand monolayer.

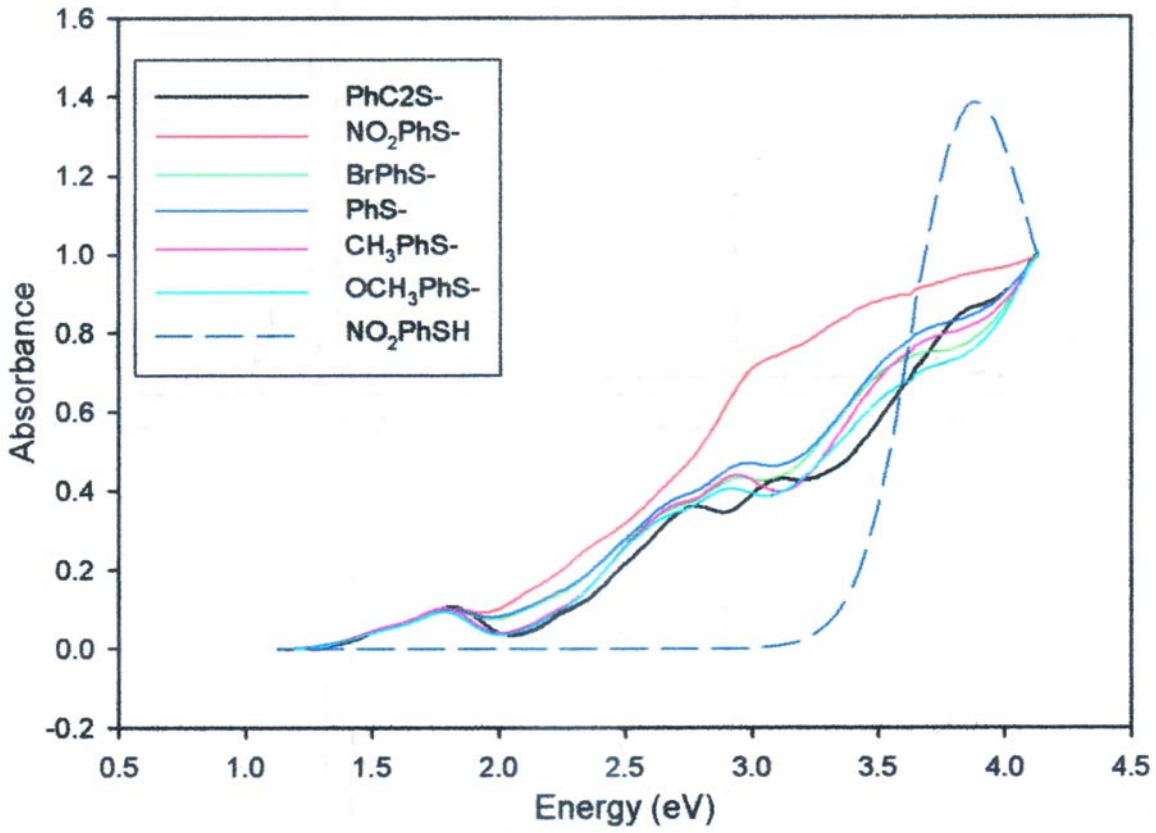


Figure 1.11 Optical spectra of ~Au_{38} clusters with various arylthiolate passivants compared to 2-phenylethanethiolate passivated MPCs. Pure *p*-nitrobenzenethiol is also shown for comparison due to the unique spectrum observed for clusters passivated its thiolate. Core-passivant interactions are hypothesized to yield this unusual spectrum relative to the other MPCs. Figure reproduced from reference 58.

The reaction of $Au_{38}(SC_2H_4Ph)_{24}$ MPCs with excess triphenylphosphine (PPh_3) to yield smaller clusters with an optical spectrum similar to $Au_{11}(PPh_3)_8Cl_3$ (undecagold)[9] and a $Au(SC_2H_4Ph)$ byproduct was also reported.[60] The exchange of PPh_3 occurred at a rate of .0023 $M^{-1}s^{-1}$ to .01 $M^{-1}s^{-1}$, which is approximately ten times greater than for

arylthiolates exchanged onto this cluster.[58] The exchange rates for PPh_3 slowed when oxygen was present, unlike thiol-thiolate exchange reactions on gold MPCs. This methodology validated the conversion of larger core clusters to smaller ones and suggested significant differences between core atoms and surface atoms in gold MPCs, owing to the "peeling" of the outer Au:thiolate complexes to leave a smaller core passivated by PPh_3.

More insight into the nature of thiolate-gold bonding in MPCs was discovered in 2005 by X-ray absorption near edge structure (XANES) and extended x-ray absorption fine structure (EXAFS).[61] The XANES measurements found $Au_x(alkylthiolate)_y$ MPCs of diameter ~1.4 nm to have less d-electron density than bulk gold, arising from metal to ligand charge transfer (MLCT). EXAFS revealed strong structural distortion from the expected *fcc* ordering found in bulk gold. These $Au_x(alkylthiolate)_y$ MPCs possessed gold-gold bond lengths ~5.0 % longer than in bulk gold, due to charge transfer to thiol, overcoming the expected lattice contraction with decreasing core size. EXAFS data for larger, ~1.8 nm Au:mercaptomaltose MPCs showed lattice contraction of only 2.0 % relative to bulk gold, with gold to sulfur charge transfer postulated as responsible for keeping the gold-gold distances near those of bulk gold. Lattice contractions and expansions were absent in even larger, colloidal $Au_x(NR_4Br)_y$ systems of up to 5 nm diameter. This new information provided evidence of structural properties induced by surface chemistry within molecular-scale gold MPCs and further studies should provide new insights into the role surface species play in determining gold MPC optical, electronic, and structural properties.

The large role of surface passivants on core optical properties was further demonstrated in a subsequent report of chiroptically active Au MPCs passivated with D and L penicillamine [$HSC(CH_3)_2CH(NH_2)CO_2H$] with core diameters of .57 nm, 1.18 nm, and 1.75 nm.[62] The $Au_x[SC(CH_3)_2CH(NH_2)CO_2H]_y$ MPCs displayed the same chirality as the specific penicillamine used to passivate the cluster surface, and no chiroptical effects were observed on clusters with racemic protective monolayers. The chiroptical activity (Cotton Effect) was found to increase with decreasing core diameter, strongly suggesting surface effects as responsible for this phenomenon. The anisotropy factor as a function of wavelength for each of these clusters is shown in Figure 1.12. This work provided further evidence of the dominant role the protective monolayer could have on gold MPC optical properties, validated an earlier report of chiroptically active $Au_x(glutathionate)_y$ MPCs[29], and hinted at the possibility of chirally active fluorescence probes.

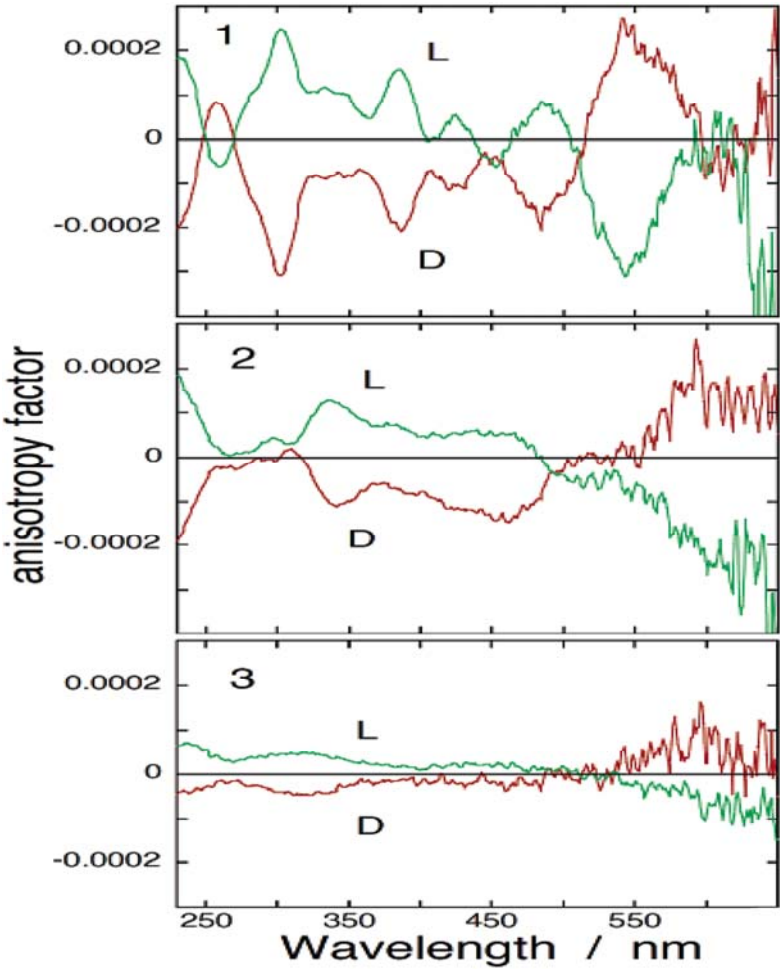


Figure 1.12 Anisotropy factor (*g*-factor) for L and D penicillamine passivated gold clusters. Diameters from top to bottom are: (1) .57 nm (2) 1.18 nm and (3) 1.75 nm. Note the mirror image nature of the two enantiomeric forms and the lowered anisotropy factor with increasing diameter. Figure adapted from Reference 62.

In closing, an overview of the known properties of gold quantum dots was provided to allow a better understanding of the work contained within this dissertation and place it within the proper context. The salient points describing gold quantum dots follow. Gold quantum dots possess core diameters below 1.8 nm and have fewer than 200 gold atoms in their core. To date, no bulk crystals of these materials have been produced, preventing total structural determination. Compositions are typically estimated by correlating mass spectrometry, x-ray diffraction, elemental analysis, and thermogravimetric analysis. The clusters exhibit size dependent quantum confinement of

electrons, molecule-like optical transitions, and discrete charge states. The precise number of gold atoms in the core is typically known within 10 % and a fairly accurate, if overlooked model predicting possible core compositions utilizes electronic shell closings, as shown in Figure 1.13. The core compositions of many of the clusters described in this chapter appear in Figure 1.13. If the protective monolayer is absent or removed, aggregation to colloids or bulk gold results.

A large variety of alkanethiolates and arenethiolates have been used as gold MPC surface passivants at the bulk, colloidal, and sub-colloidal level. The self-assembled monolayer (SAM) composition on the MPC surface can be modified by ligand exchange reactions, altering the optical and electronic properties of gold quantum dots. An experimental understanding of these core-passivant interactions is still being developed. Aromatic passivants still remain mostly unexplored in the $\leq$ 2.0 nm core diameter regime for gold MPC formation, despite 25 years of research and the utility of benzenethiol for CdSe nanocrystallite synthesis.[4] A lack of information about aromatic passivated gold MPCs provided the impetus for the work described herein.

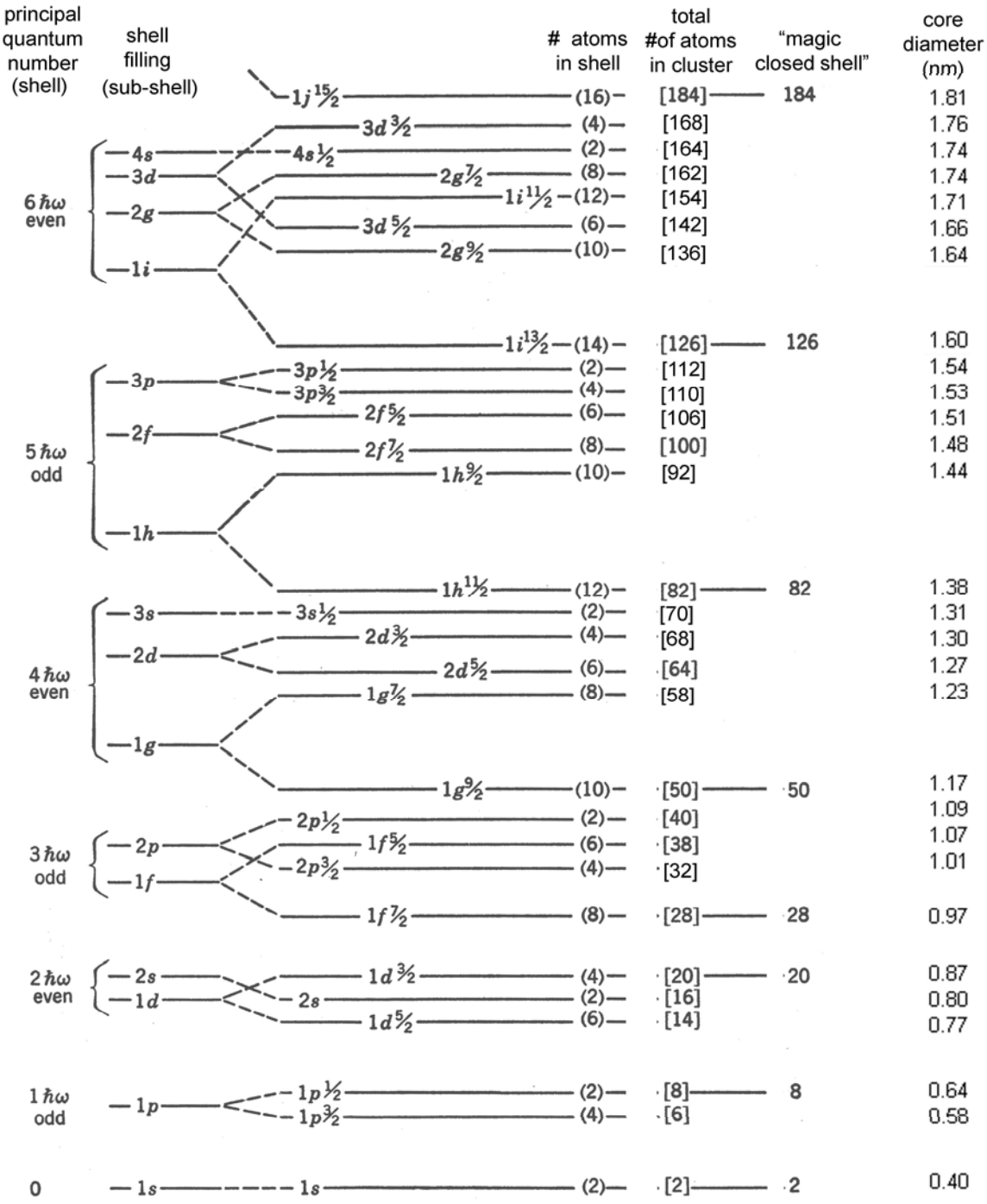


Figure 1.13 Schematic diagram of nuclear level shell theory applied to gold clusters. The model is interpolated between the square well and the harmonic oscillator model limit with spin orbit coupling included. Figure adapted from reference 63**. C**ore diameters estimated from the number of gold atoms (N) and bulk density (59 atoms/nm^3) with the relation:

$$D = \left(\frac{N}{31}\right)^{\frac{1}{3}}$$

Chapter 1 References

(1) Brus, L. E. *J. Phys. Chem.* **1986**, *90*, 255

(2) Steigerwald, M. L.; Alivisatos, A. P.; Gibson, J. M.; Harris, T. D.; Kortan, R.; Muller, A. J.; Thayer, A. M.; Duncan, T. M.; Douglass, D. C.; Brus, L. E. *J. Am. Chem. Soc.* **1988**, *110(10)*, 3046

(3) Frenkel, F. *www.mit.edu/afs/athena.mit.edu/org/m/museum/exhibits/frankel4.html*, accessed 11/15/2005

(4) Herron, N.; Calabrese, J. C.; Farneth, W. E.; Wang, Y. *Science*, **1993**, *259*, 1426

(5) Hawkins, J.; Lewis, T.; Loren, S.; Meyer, A.; Heath, J.; Saykally, R.; Hollander, F. *J. Chem. Soc., Chem. Comm.* **1991**, *11*, 775

(6) Faraday, M. *Phil. Trans. Roy. Soc. London* **1857**, *147*, 145

(7) Cariati, F.; Naldini, L. *Inorg. Chim. Acta.* **1971**, *5*, 172

(8) Cariati, F.; Naldini, L. *J. Chem. Soc. Dalton Trans.* **1972**, 2286

(9) Vollenbroek, F.; Van den Berg, J.; Van der Velden, J.; Bour, J. *Inor. Chem.* **1980**, *19*, 2685

(10) Briant, C.; Theobald, B.; White, J.; Bell, L.; Mingos, M.; Welch, A. *J. Chem. Soc., Chem. Comm.* **1981**, 201

(11) Schmid, G.; Pfeil, R.; Boese, R. Bandermann, F.; Meyer, S.; Clais, G.; v.d. Velden, J. *Chem. Ber.*, **1981**, *114*, 3634

(12) Duff, D.; Baiker, A.; Edwards, P. *J. Chem. Soc., Chem. Comm.* **1993**, *1*, 96

(13) Brust, M.; Walker, M.; Bethell, D.; Schiffrin, D.; Whyman, R. *J. Chem. Soc., Chem. Comm.* **1994**, *7*, 801

(14) Whetten R.; Khoury, J ; Alvarez, M.;.Murthy, S.; Vezmar, I.; Wang, Z. L.; Stephens, P.; Cleveland, C.; Luedtke, W.; Landman, U.. *Adv. Mater.* **1996**, *8*, 428

(15) Alvarez, M.; Khoury, J.; Schaaff, T.; Shafigullin, M.; Vezmar, I.; Whetten, R. *Chem. Phys Lett.* **1997**, *266*, 91

(16) Alvarez, M.; Khoury, J.; Schaaff, T.; Shafigullin, M.; Vezmar, I.; Whetten, R. *J. Phys. Chem. B.* **1997**, *101(19)*, 3706

(17) Cleveland, C.; Landman, U.; Schaaff, T.; Shafigullin, M., Stephens, P.; Whetten R. *Phys. Rev. Lett.* **1997**, *79(10)*, 1873

(18) Schaaff, T.; Shafigullin, M.; Khoury, J.; Vezmar, I.; Whetten, R.; Cullen, W.; First, P.; Gutierrez-Wing, C.; Ascensio, J.; Jose-Yacaman, M. *J. Phys. Chem. B.* **1997**, *101*, 7885

(19) Logunov, S.; Ahmadi, T.; El-Sayed, M.; Khoury, J.; Whetten, R. *J. Phys. Chem. B.* **1997**, *101*, 3713

(20) Ingram, R.; Hostetler, M.; Murray, R.; Schaaff, T.; Khoury, J.; Whetten, R.; Bigioni, T.; Guthrie, D.; First, P. *J. Am. Chem. Soc.* **1997**, *119*, 9279

(21) Chen, S.; Ingram, R.; Hostetler, M.; Pietron, J.; Murray, R.; Schaaff, T.; Khoury, J.; Alvarez, M.; Whetten, R. *Science* **1998**, *280*, 2098

(22) Whetten, R.; Shafigullin, M; Khoury, J.; Schaaff, T.; Vezmar, I.; Alvarez, M.; Wilkinson, A. *Acc. Chem. Res.* **1999**, *32*, 397

(23) Hostetler, M.; Wingate, J.; Zhong, C.; Harris, J.; Vachet. R.; Clark, M.; Londono, D.; Green, S.; Stoke, J.; Wignall, G.; Glish, G.; Porter, M.; Evans, N.; Murray, R. *Langmuir*, **1998**, *14*, 17

(24) Schaaff, T.; Knight, G.; Shafigullin, M.; Borkman, R.; Whetten, R. *J. Phys. Chem. B.* **1998**, *102*, 10643

(25) Pietron, J.; Hicks, J.; Murray, R. *J. Am. Chem. Soc.* **1999**, *121*, 5565

(26) Wuelfling, P.; Green, S.; Pietron, J.; Cliffel, D.; Murray, R. *J. Am. Chem. Soc.* **2000**, *122*, 11465

(27) Bigioni, T.; Harrell, L.; Cullen, W.; Guthrie,D.; Whetten, R.; First, P. *Eur. Phys. J. D.*, **1999**, *6*, 355

(28) Gutierrez, E; Powell, R.; Furuya, F.; Hainfelf, J.; Schaaff, T.; Shafigullin, M.; Stephens, P.; Whetten, R. *Eur. Phys. J. D.*, **1999**, *9*, 647

(29) Schaaff, T.; Whetten, R. *j. Phys. Chem. B.* **2000**, *104*, 2630

(30) Bigioni, T.; Whetten, R.; Dag, O. *J. Phys. Chem. B.* **2000**, *104*, 6983

(31) Weare, W.; Reed, S.; Warner, M.; Hutchison, J. *J. Am. Chem. Soc.* **2000**, *122*, 12890

(32) Huang, T; Murray, R. *J. Phys. Chem. B.* **2001,** *105*, 12498

(33) Shon, Y.; Mazzitelli, C.; Murray, R. *Langmuir* **2001**, *17*, 7735

(34) Boyen, H.; Kastle, G.; Wegil, F.; Ziemann, P.; Schmid, G.; Garnier, M.; Oelhafen, P. *Phys. Rev. Lett.*, **2001**, *87(27)*, 6401

(35) Song, Y.; Murray, R. *J. Am. Chem. Soc.* **2002**, *124*, 7096

(36) Hostetler, M.; Templeton, A.; Murray, R. *Langmuir* **1999**, *15*, 3783

(37) Woerhle, G.; Warner, M.; Hutchison, J. *J. Phys. Chem. B.* **2002**, *106*, 9979

(38) Link, S.; Beeby, A.; Fitzgerald, S.; El-Sayed, M.; Schaaff, T.; Whetten, R. *J. Phys. Chem. B.* **2002**, *106*, 3410

(39) Hicks, J.; Miles, D.; Murray, R. *J. Am. Chem. Soc.* **2002**, *124*, 13322

(40) Quinn, B.; Liljeroth, P.; Ruiz, V.; Laaksonen, T.; Kontturi, K. *J. Am. Chem. Soc.* **2003**, *125*, 6644

(41) Negishi, Y.; Tsukuda, T. *J. Am. Chem. Soc.* **2003**, *125*, 4046

(42) Garzon, I.; Beltran, M.; Gonzalez, G.; I. Gutierrez-Gonzalez; K. Michaelian; Reyes-Nava, J.; Rodriguez-Hernandez, J. *Eur. Phys. J. D.* **2003**, *24*, 105

(43) Zhang, H.; Stender, M.; Zhang, R.; Wang, C.; Li, J; Wang, L. *J. Phys. Chem. B.* **2004**, *108*, 12259

(44) Li, J.; Li., X; Zhai, H.; Wang, L. *Science* **2003**, *299*, 864

(45) De Heer, W. *Rev. Mod. Phys.* **1993**, *65*, 611

(46) Petroski, J.; Chou, M.; Cruetz, C. *Inorg. Chem.* **2004**, *43*, 1597

(47) Negishi, Y.; Takasugi, Y.; Sato, S.; Yao, H.; Kimura, K.; Tsukuda, T. *J. Am. Chem. Soc.* **2004**, *126*, 6518

(48) Kim, Y.; Oh, S.; Crooks, R. *Chem. Mater.* **2004**, *16*, 167

(49) Garcia-Martinez, J.; Crooks, R. *J. Am. Chem. Soc.* **2004**, *126*, 16170

(50) Lee, D.; Donkers, R.; Wang, G.; Harper, A.; Murray, R. *J. Am. Chem. Soc.* **2004**, *126*, 6193

(51) Jimenez, V.; Georganopoulou, D.; White, R.; Harper, A.; Mills, A.; Lee, D.; Murray, R. *Langmuir*, **2004**, *20*, 6864

(52) Donkers, R.; Lee, D.; Murray, R. *Langmuir*, **2004**, *20*, 1945

(53) Donkers, R.; Song, Y.; Murray, R. *Langmuir*, **2004**, *20*, 4703

(54) Wang, G.; Huang, T.; Murray, R.; Menard, L.; Nuzzo, R. *J. Am. Chem. Soc.* **2005**, *127*, 812

(55) Huang, T.; Murray, R. *J. Phys. Chem. B.* **2003**, *107*, 7434

(56) Kuno, M.; Lee, J.; Dabbousi, B.; Milkulec, F.; Bawendi, M. *J. Chem. Phys.* **1997**, *106*, 9869

(57) Guo, R.; Song, Y.; Wang, G.; Murray, R. *J. Am. Chem. Soc.* **2005**, *127*, 2752

(58) Guo, R.; Murray, R. *J. Am. Chem. Soc.* **2005**, *127*, 12140

(59) Song, Y; Harper, A.; Murray, R. *Langmuir* **2005**, *21*, 5492

(60) Wang, W.; Murray, R. *Langmuir* **2005**, *21*, 7015

(61) Lopez-Cartes, C.; Rojas, T.; Litran, R.; Martinez, D.; de la Fuente, J.; Penades, S.; Fernandez, A. *J. Phys. Chem. B.* **2005**, *109*, 8761

(62) Yao, H.; Miki, K.; Nishida, N.; Sasaki, A.; Kimura, K. *J. Am. Chem. Soc.* **2005**, *127*, 15536

(63) Jenson, J. *Elementary Theory of Nuclear Shell Structure* ed. Goeppert-Mayer M. **1955** John Wiley & Sons, Inc.

CHAPTER 2

GOLD:ARYLTHIOLATE QUANTUM DOTS WITH 1.7 AND 1.5 NANOMETER CORES

2.1 Previous Syntheses of Gold:Arylthiolate Monolayer Protected Clusters

Reports of aromatic thiolates on gold clusters with core diameters below 2.0 nm remain limited.[1,2] Similar three nanometer and larger colloids have been generated with benzenethiolate and various para substituted benzenethiolates as passivation monolayers. All methods for generating these colloids are modifications of the reaction first reported by Brust, Walker, Bethell, Schiffrin, and Whyman in 1994.[3] The generally accepted basic reaction scheme occurs in a two phase solution often composed of water and toluene. There is much variance in stoichiometry between research groups utilizing the reaction, hence it is omitted in the typical reaction scheme that follows in Figure 2.1.

(1) $HAuCl_{4(aq)}$ + tetraoctylammonium $bromide_{(tol)} \rightarrow$ $TOA[AuCl_4]_{(tol)} + HBr_{(aq)}$

(2) $TOA[AuCl_4]_{(tol)} + HSR_{(tol)} \rightarrow (Au^{I}SR)_{x(tol)} + HCl_{(aq)} + RSSR + TOACl_{(tol)}$

(3) $(Au^{I}SR)_{x(tol)} + NaBH_{4(excess)} \rightarrow Au_x(SR)_{y(tol)}$

(4) Solvent removal and impurity extraction with ethanol, acetone, and/or acetonitrile.

(5) Product elution from a frit with a suitable solvent (typically hexane or toluene).

Figure 2.1 Multistep reaction scheme first employed by Brust et al. Tetraoctylammonium is abbreviated is TOA henceforth.

In this reaction scheme, TOABr acts as a phase transfer reagent to transfer $[AuCl_4]^-$ into the organic phase for subsequent reaction with hydrophobic thiols and stirring is continuous throughout. Steps (1) and (2) typically require at most an hour and the

reduction step in (3) is completed within 24 hours. Use of a 3:1 ratio of thiol to gold in step (2) of this reaction ensures the following stoichiometric reaction is driven to completion as shown.[4]

$$3n\mathrm{RS}^- + n\mathrm{Au}^{\mathrm{III}} \rightarrow (\mathrm{Au}^{\mathrm{I}}\mathrm{SR})_n + n\mathrm{RSSR}$$

{spectator halides and protons omitted for clarity}

This stoichiometry gives the smallest clusters at room temperature with any given thiol and using a lower thiol to gold ratio tends to give larger clusters. Thiol to gold ratios below three are often used to "thermodynamically" control the core size of colloidal gold thiolate MPCs.[5]

Our initial use of this method with 1:3: 3:10 molar ratios of Au:TOABr:HSPh:$NaBH_4$ produced poor yields of Au_x(benzenethiolate)$_y$ MPCs with diameters above 2.0 nm.[6] Chen and Murray applied this same stoichiometry at 0 ^oC , obtaining unstable $Au_x(SPh)_y$ MPCs with ~2.0 nm cores and $Au_x(SPh\text{-}CH_3)_y$ MPCs with ~3.0 nm cores. These clusters decomposed in sodium cyanide three to 16 times faster than similar Au_x(hexanethiolate)$_y$ MPCs.[7]

Several groups have obtained 2.9 to 6.0 nm core MPCs with the 4-X-C_6H_4S- passivants (where X= H, OH, COOH, NH_2, CH_3, Cl, Br, and CF_3) by using a one-phase method with methanol as the reaction solvent.[8a-e] In these cases, excess glacial acetic acid was typically substituted for TOABr with Au:SR ratios of 1:1 to 2.4:1. The rationale for glacial acetic acid use has never been published. This methodology was also effective for producing stable 4.0 – 5.6 nm Au_x(2-mercaptopyridine)$_y$ MPCs.[9] It is noteworthy that these research groups relied only on optical spectroscopy and TEM estimates of average core diameter. The optical spectra of any small clusters present in these samples would be masked by the large plasmon absorbance present in colloidal gold. Furthermore, the TEM estimates provided no details of how many particles were counted for the size estimates, or whether an automated counting algorithm was utilized. In two of the cases the overall

research goal was to produce a "nanophase" material that would be responsive to organic vapors for sensor applications, therefore a high level of characterization may have been deemed unnecessary.[8c,d]

2.2 A Route to 1.7 nm and 1.5 nm Gold:Benzenethiolate Quantum Dots

The previous inability of standard Brust-type conditions to produce $\leq$ 2.0 nm gold:arylthiolate MPCs and the observation of preferential elution by methylene chloride of larger $Au_x(SPh)_y$ MPCs formed by the method in Figure 2.1 prompted investigation of dichloromethane (DCM) as a reaction medium.[10] The reaction scheme initially employed for this admittedly non-rational synthesis shown in Figure 2.2.

(1) $n\ HAuCl_{4(aq)} + 1.2n\ TOABr_{(DCM)} + 3n\ HSPh_{(DCM)} \rightarrow (Au^{I}SPh)_{n(DCM)} + n(PhS)_2 + 4n\ HCl_{(aq)}$

(2) $1.2n\ TOABr_{(DCM)} + (Au^{I}SPh)_{n(DCM)} + 10\ NaBH_{4(aq)} \rightarrow TOA_z[Au_x(SR)_y]^{z-}{}_{(DCM)} +$
$1.2\text{-}z\ TOABr_{(DCM)} + z\ NaBr$ (TOA^+ evident in products by multiple analyses)

(3) Solvent removal and impurity extraction with ethanol or acetone.

(4) Product eluted from frit with DCM. (Later changed to toluene *followed* by DCM)

Figure 2.2 Reaction scheme for sub 2.0 nm core $Au_x(SPh)_y$ MPCs. The TOABr shown in step (2) is remnant material from step (1), not additional TOABr added to the reaction.

The use of a 1.2:1 molar ratio of TOABr to gold in step (1) does not alter cluster size and presents less organic impurity for removal during purification.[11,12] The Au:SPh polymer formed in step (1) was observed to form much slower than the half hour normally required by alkanethiols. Remnant yellow coloration, characteristic of aqueous $HAuCl_4$ initially persisted for over 24 h when benzenethiol was added *after* phase transfer of $AuCl_4^-$ in step (2). Placing benzenethiol in the organic phase *during* this phase transfer step reduced the polymer formation time to ~12 h, rather than > 24 h, evident by the

absence of yellow coloration and formation of white polymeric $[Au(I):SPh]_x$. During collaboration with Dr. Greg Schaaff over the course of a year, it was determined 16 h for complete polymer formation (step 1) with at least 16 hours of reduction (step 2) yielded materials with consistent optical and solubility properties. The optical spectra of the products resembled 1.7 nm core $Au_x(alkylthiolate)_y$ MPCs.

While applying typical purification methods to these novel clusters, valuable insights were gained regarding their chemical properties. These discoveries included:

(1) Use of acetone to extract excess TOABr and diphenyldisulfide from the clusters led to complete and rapid degradation to large colloidal particles and bulk gold, implying ambient electrochemical activity.
(2) Storage of the clusters in methylene chloride or chloroform allowed cluster degradation to bulk gold within one week, evident as a gold mirror on the container surface. This further implied an active electrochemistry.
(3) Prolonged extraction of impurities in a Soxhlet extractor with ethanol led to some sample degradation and no substantial improvement in purity of the MPCs. (No efforts to exclude oxygen were taken.)
(4) Tetraoctylammonium (TOA^+) was always present in the MPCs at a fairly constant molar ratio indicating its presence as a necessary counterion, rather than as TOABr contamination.
(5) The MPCs were stable for over a year when dried and could readily be redispersed in methylene chloride.

The apparent MPC instability in methylene chloride initially seemed problematic, therefore other solvents, including ethanol, isopropanol, and tetrahydrofuran were utilized during synthesis, but no particles were formed in these solvents. At this point, the solvents used to elute the purified MPCs were varied, with the goal of finding a solvent less reactive than halocarbons. Toluene was found to elute most (66 %) of the soluble material synthesized, while the remainder was eluted by methylene chloride. The toluene

soluble MPCs were chemically distinct from the methylene chloride soluble MPCs and stable for years in toluene. Both of these materials are detailed in Chapter 3, but at this point it is sufficient to note that the toluene fraction contains MPCs of 1.5 nm core diameter and the remainder are 1.7 nm core diameter. This demonstrates conditions that produce a material enriched in 1.5 nm cores analogous to a prior report of ubiquitous (thermodynamically favored) 1.7 nm core diameter $Au_x(alkylthiolate)_y$ clusters.[6] Multiple analytical techniques indicate the MPCs formed are anionic with TOA cations providing charge balance (detailed fully in Chapter 2.3.4-2.3.6). The specific synthetic route used to generate these clusters has been repeated in excess of twenty times and is described below.

Synthesis of 1.7 nm and 1.5 nm Gold:Benzenethiolate Quantum Dots

Hydrogen tetrachloraurate (516 mg, 1.5 mmol) is dissolved in deionized water (20 mL). This aqueous solution is then added to dichloromethane (75 mL) containing tetraoctylammonium bromide (1.002 g, 1.8 mmol) and benzenethiol (0.5 mL, 4.5 mmol). The mixture is stirred vigorously for 16 hours to ensure formation of the cloudy, white Au:SPh:TOA complex in the organic phase. Next, $NaBH_4$ (572 mg, 15 mmol) in deionized water (20 mL) is added all at once and stirred an additional 24 hours to ensure complete reduction. The solution is next dried by rotary evaporation to remove most of the dichloromethane, and precipitated thrice with ethanol (150 mL each) to remove diphenyldisulfide (DPDS) and TOABr/Cl. The clusters are then transferred to a 0.16 μm filter with acetonitrile and rinsed twice with acetonitrile (80 mL) to remove residual tetraoctylammonium bromide. Soxhlet extraction with ethanol for 96 h has been employed to remove residual tetraoctylammonium bromide after these purification steps,

but tetraoctylammonium is always evident by ^{1}H-NMR and infrared spectroscopy (to be discussed in Section 2.3.5). Molecular-level purity is obtained by the rinse/extraction methods described (as evidenced by mass spectrometry) and Soxhlet extraction has been found unnecessary.

A slight yellow coloration in the acetonitrile rinse resembles the optical spectrum of known 5.5 kDa (Au_{28}) core MPCs[13], but the material is present in sub-milligram quantities and no further characterization was possible. Toluene (100 mL) elutes 39.4 mg of 1.5 nm core MPCs from the cleaned material on the .16 μm filter, followed by addition of dichloromethane (100 mL) to elute 17.7 mg of 1.7 nm core MPCs. A significant amount of insoluble material consistent with composition $(Au^{I}SPh)_x$ remains after elution. The 1.5 nm MPCs are stable in toluene for years if kept away from light and oxygen. The materials decompose over days to weeks if stored in dichloromethane or tetrahydrofuran and should be stored dry when possible. The room temperature solubilities of the 1.5 and 1.7 nm core MPCs in toluene are 630 μM and 160 μM, respectively. In dichloromethane at room temperature, the 1.5 nm MPCs are soluble at 290 μM and the 1.7 nm clusters are soluble at 576 μM.

2.3 Physical Properties of 1.5 and 1.7 nm $Au_x(SPh)_y$ Quantum Dots

2.3.1 Optical Spectroscopy

As outlined in Chapter 1, size dependent properties arise in gold clusters below two nanometers in diameter. The optical appearance and spectrum of a cluster solution immediately reveals the absence or presence of the characteristic violet/red coloration of a strong plasmon absorbance centered near 2.4 eV. Any gold cluster below two nanometers in diameter lacks this feature. The optical absorbance spectrum of a MPC

sample is the first property characterized after generation and purification. The optical absorbance spectra for 1.7 and 1.5 nm $Au_x(SPh)_y$ are shown in Figure 2.3 with analogous Au_x(hexanethiolate)$_y$ clusters provided for comparison.[14] The plasmon absorbance present in the 2.2 nm MPCs spectrum is clearly absent in both the benzenethiolate and hexanethiolate passivated MPCs. The $Au_x(SPh)_y$ MPCs differ significantly from the Au_x(S-hexyl)$_y$ MPCs, lacking a broad absorbance feature with onset at 3.0 eV. This e depletion of this absorbance feature likely arises from withdrawal of conduction electrons from the metallic core by benzenethiolate (metal to ligand charge transfer), as benzenethiol has higher electronegativity than alkylthiols. The higher electronegativity of benzenethiol is evidenced by its pKa of 6.62, whereas benzenemethanethiol ($HSCH_2Ph$) has a pKa of only 9.43.[15] Metal to ligand charge transfer (MLCT) of gold d electron density to the π^* system of the aromatic ring through the sulfur atom may also play a role in electronic depletion of the metallic core. Hybridization of sulfur 3d-orbitals with the π bonding orbitals of benzenethiol has been known since 1965. [16] The benzenethiolate passivated MPCs also show minor spectral variation from 1.25 to 2.25 eV relative to the corresponding hexanethiolate passivated MPCs.

Plotting the derivatives of the spectra better compares the varying optical spectra, shown in Figure 2.4. The derivative spectra are analogous to a partial density of states plot for the metallic core, arising from the valence electronic bands capable of absorbing high energy photons ($\geq$ 1.1 eV). The differential plot is a direct representation of the energy-level quantization (quantum size effect) in the unoccupied portion of the

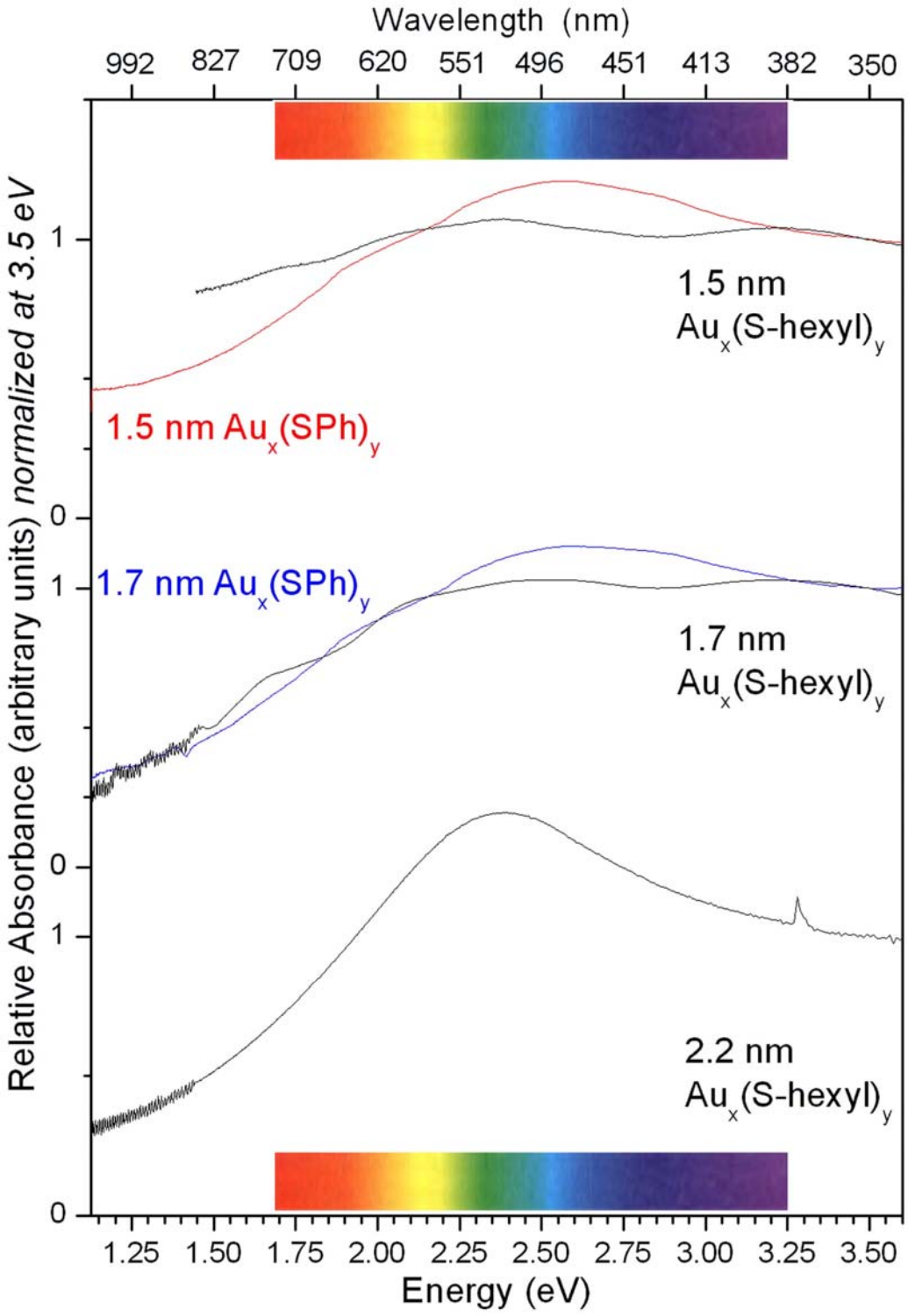


Figure 2.3 Optical spectra of $Au_x(SPh)_y$ clusters compared to previously reported Au_x(hexanethiolate)$_y$ MPCs.[14] Spectra are normalized at 4.1eV to account for concentration differences. The colors shown at the top and bottom visually show the 2.2 nm colloidal clusters to strongly absorb all but red and violet light, giving rise to a purple coloration. The small clusters absorb all but a small amount of red light, imparting dark black/brown coloration.

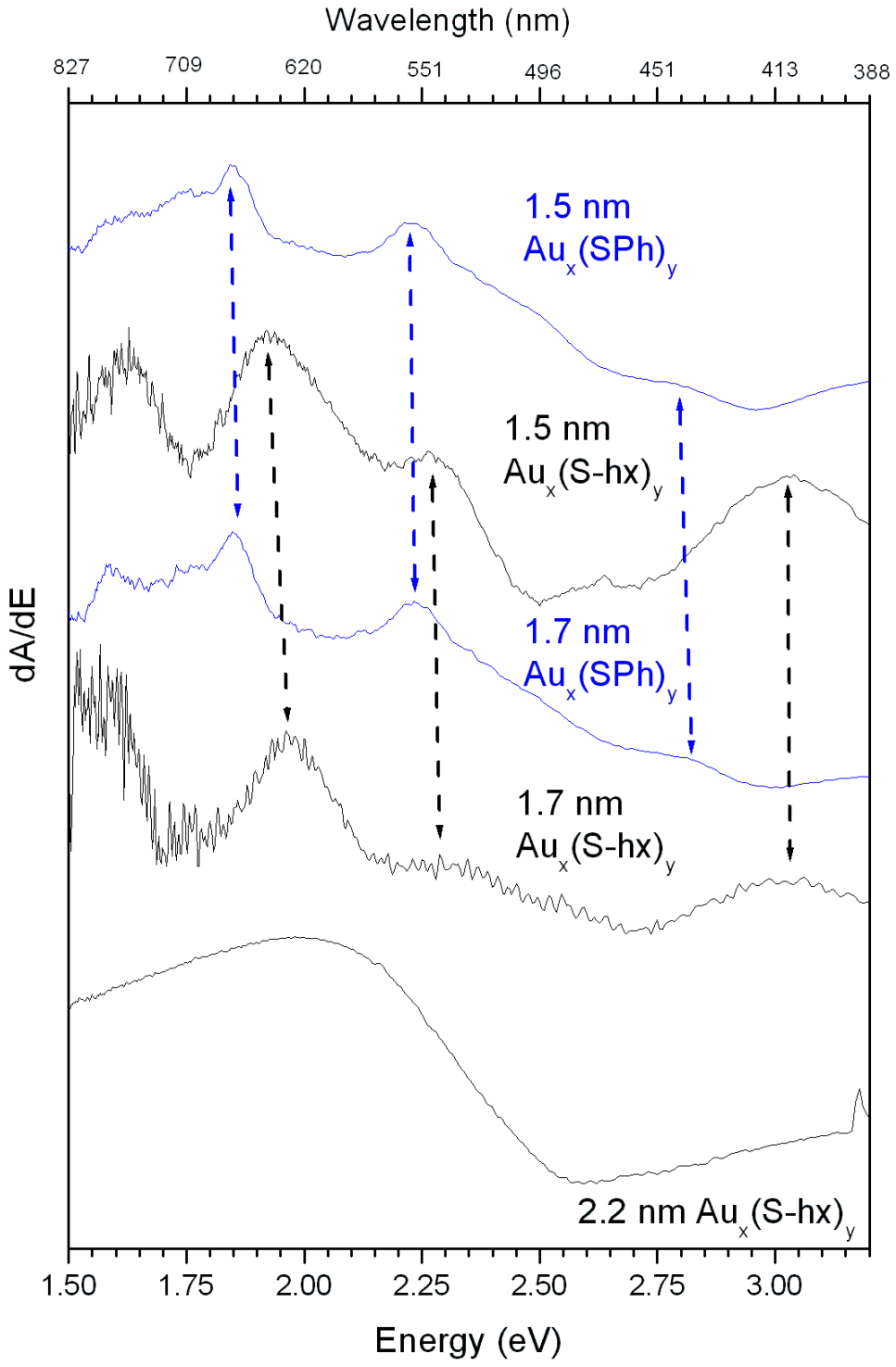


Figure 2.4 Differential optical spectra of benzenethiolate (blue) and hexanethiolate (black) passivated 1.7 and 1.5 nm clusters. Dashed lines indicate shared features between MPCs with the same passivation layer.

conduction band. The absorbance features above 1.6 eV arise from intraband electronic transitions from filled $6d^{10}$ HOMOs to 6sp LUMOs. Each absorbance band contains a series of closely spaced energy levels with spacings dependent upon the number of gold atoms present. A spherical-spheroid electronic shell structure estimates the quantized level structure of these bands to contain average energy level spacings (δ) of 8 eV/N_{Au}, where N_{Au} is the number of cluster gold atoms.[14] By this model, a 2.2 nm (320 atom) cluster would have mean energy level spacings of 25 meV, equivalent to k_BT at room temperature.[14] The observed lack of fine structure in the 2.2 nm colloidal gold optical spectrum confirms this prediction. Smaller 1.7 and 1.5 nm clusters are anticipated to have 57 and 73 meV mean energy level spacings, respectively, but are thermally broadened at room temperature, giving rise to the observed broad absorbance bands. The geometry of the gold atoms in the cluster will determine the total number of electronic states and if any degenerate states are present. Only a crystal structure will provide the true structure of the cluster cores. In spite of this, the observed electronic states are available for electrochemical oxidation and reduction while leaving the core intact, as outlined in chapter 1.

The molar absorptivity coefficients (ε) for the 1.5 and 1.7 $Au_x(SPh)_y$ MPCs were determined over the spectral range of 1.1 to 3.1 eV with serial micromolar scale dilutions. The clusters are strongly absorbing, with ε values on the scale of 12,000 at 1.1 eV for the 1.5 nm core clusters. This results in an absorbance of 1.27 at 1.13 eV (1100 nm) for a cluster concentration of only 83 μM! The ε plots are shown in Figure 2.5.

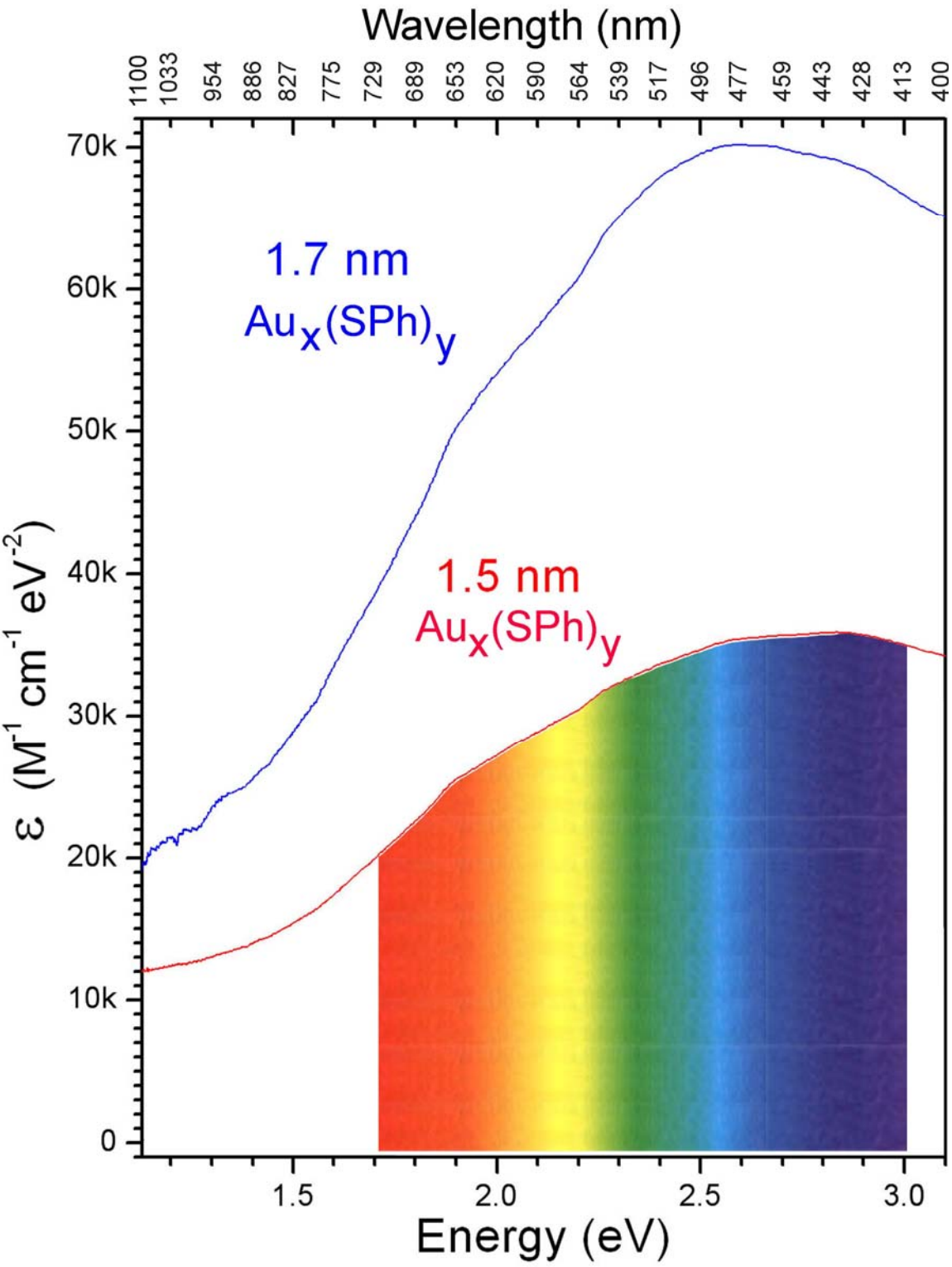


Figure 2.5 Molar absorptivity coefficients of $Au_x(SPh)_y$ clusters as a function of photon energy. The solvent was dichloromethane (absorbance edge 5.27 eV). Data were collected from four serial dilutions over two orders of magnitude in concentration (10^{-8} to 10^{-6} M).

2.3.2 Powder X-Ray Diffraction

2.3.2.1 Large Angle Diffraction (LAXRD)

After optically interesting gold clusters are identified, it is vital to verify the presence of a crystalline core, rather than an amorphous polymeric material or a binary molecular material. Large angle x-ray diffraction ($2\theta = 10 - 140^0$; $s = 1.1 - 12.2\ nm^{-1}$) allows comparison with bulk gold and previously isolated $Au_x(S\text{-alkyl})_y$ MPCs for core size estimation.[6,14] The similarities between the $Au_x(SPh)_y$ MPCs and their $Au_x(S\text{-hexyl})_y$ analogs are shown in Figure 2.6. In lieu of the diffraction similarities shared by the aryl and alkyl passivated clusters, it is highly likely they share similar core structures.

Average core diameter estimates are obtained as the reciprocal of the full peak width at half maximum (FWHM) for each peak present. To minimize any bias or human error, the diffraction patterns were fit with Gaussian functions using Microcal Origin software to obtain diffraction peak locations and their FWHM. An example of this process and its accuracy in evaluating the diffraction peaks is given in Figure 2.7. The experimental peak widths (FWHM) for gold clusters at this scale are typically narrower than expected when accounting for the number of gold atoms present and the bulk density of gold ($59 atoms/nm^3$). While this remains unexplained, reports of hexagonally ordered $(Ag^I(SR))_x$ non-metallic phases that can also form on Ag^0 surfaces[17a-c] offers the previously unconsidered possibility of a solid Au^0 core encased by a $(Au^I(SR))_x$ shell of unknown organization. The observed large angle diffraction could arise solely from the Au^0 core. Surface studies have found benzenethiol adsorbed onto bulk gold (111) surfaces can alter the gold surface atom ordering, with sulfur penetrating into the

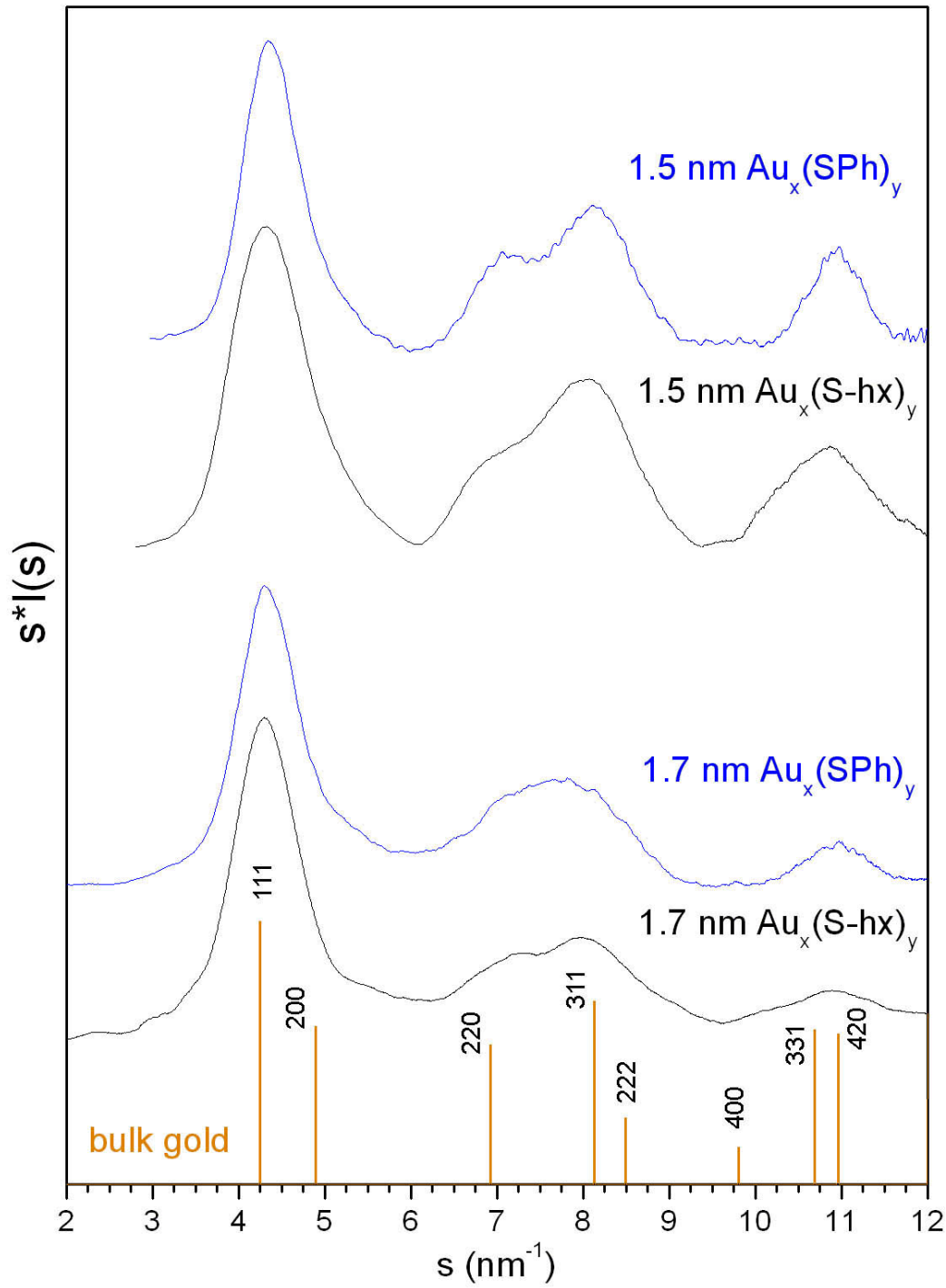


Figure 2.6 Large angle powder diffraction of benzenethiolate (blue) and hexanethiolate (black) passivated 1.7 and 1.5 nm clusters. The cores are obviously very similar. The diffraction pattern and expected peak intensities for bulk gold with the Miller indices labeled is shown at the bottom for comparison. Significantly fewer diffraction peaks relative to bulk are typical in <2.0 nm materials due to the presence of a finite number of diffraction planes and high symmetry geometries (such as tetrahedral, octahedral, decahedral or icosahedral) within these systems.

111 layer and displacing some of the gold atoms above the 111 plane[18]. This effect could definitely alter the x-ray diffraction properties of a small cluster. Additionally, recent theoretical work for $Au_{38}(SCH_3)_{24}$ clusters suggests the possibility of a neutral Au_{14} core bound to six $(AuSCH_3)_4$ units with a calculated binding energy of 1.1 eV between Au_{14} and $(AuSCH_3)_4$.[19] These finding indicate much work remains in fully understanding the structure of these materials.

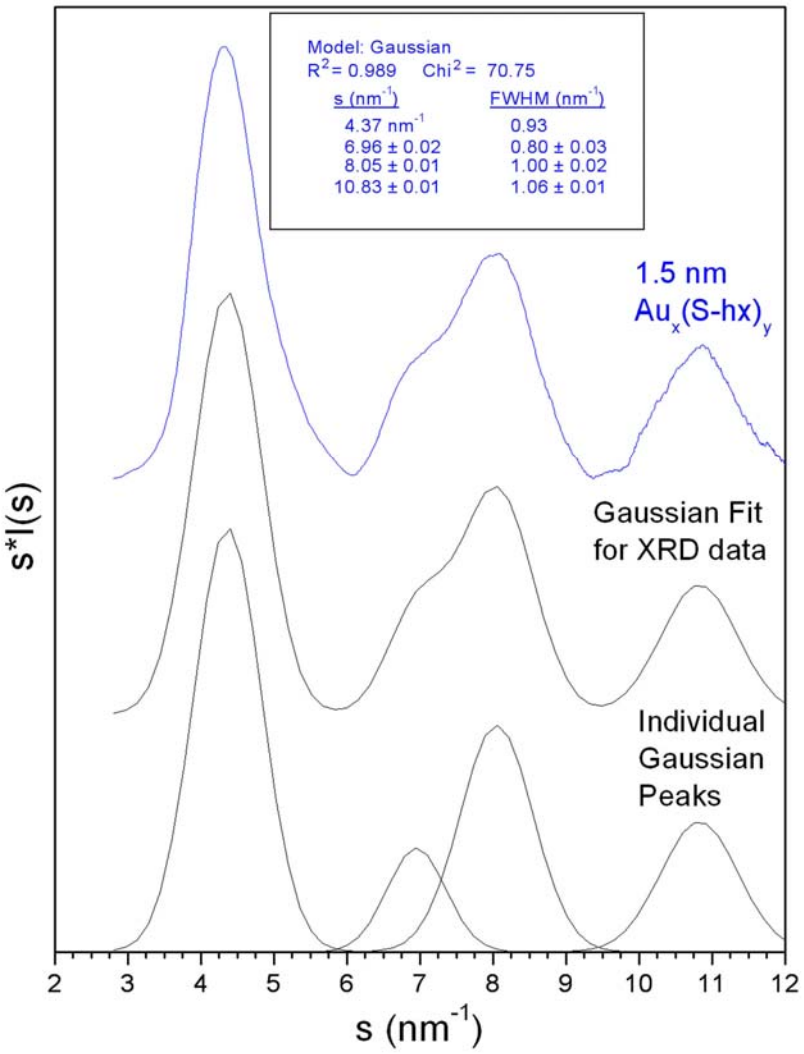


Figure 2.7 Gaussian data fits for experimental LAXRD pattern. The top (blue) plot is experimental data, the middle a Gaussian function fit, and the bottom shows the peaks comprising the Gaussian function. The top panel shows the location and FWHM of each peak, as well as the correlation coefficient (R^2) of the fits. Diffraction pattern coordinates taken from reference 13.

Although crystal structures of $Au_x(SR)_y$ MPCs remain elusive, computed powder diffraction patterns for a variety of cluster geometries between 1.0 and 2.4 nm core diameter are available.[20,21] Calculated diffraction patterns for decahedral structural models closely match the experimentally observed powder XRD data for 1.7 and 1.5 nm $Au_x(S\text{-hexyl})_y$ clusters. The structural models considered and experimental diffraction data for these $Au_x(S\text{-hexyl})_y$ MPCs are shown in Figure 2.8.

For the 1.5 nm cluster, both Ino-decahedral and Marks-decahedral structures match fairly well with the experimental diffraction pattern, preventing either from being ruled out as structural candidates. The 1.7 nm cluster model has been previously compared to a transmission electron microscope (TEM) image, clearly showing a five-fold symmetry consistent with decahedral structure (see Figure 2.9). This offers experimental validity to the theoretical structural models although it is vital to note TEM is difficult at best for clusters in this size regime.[22]

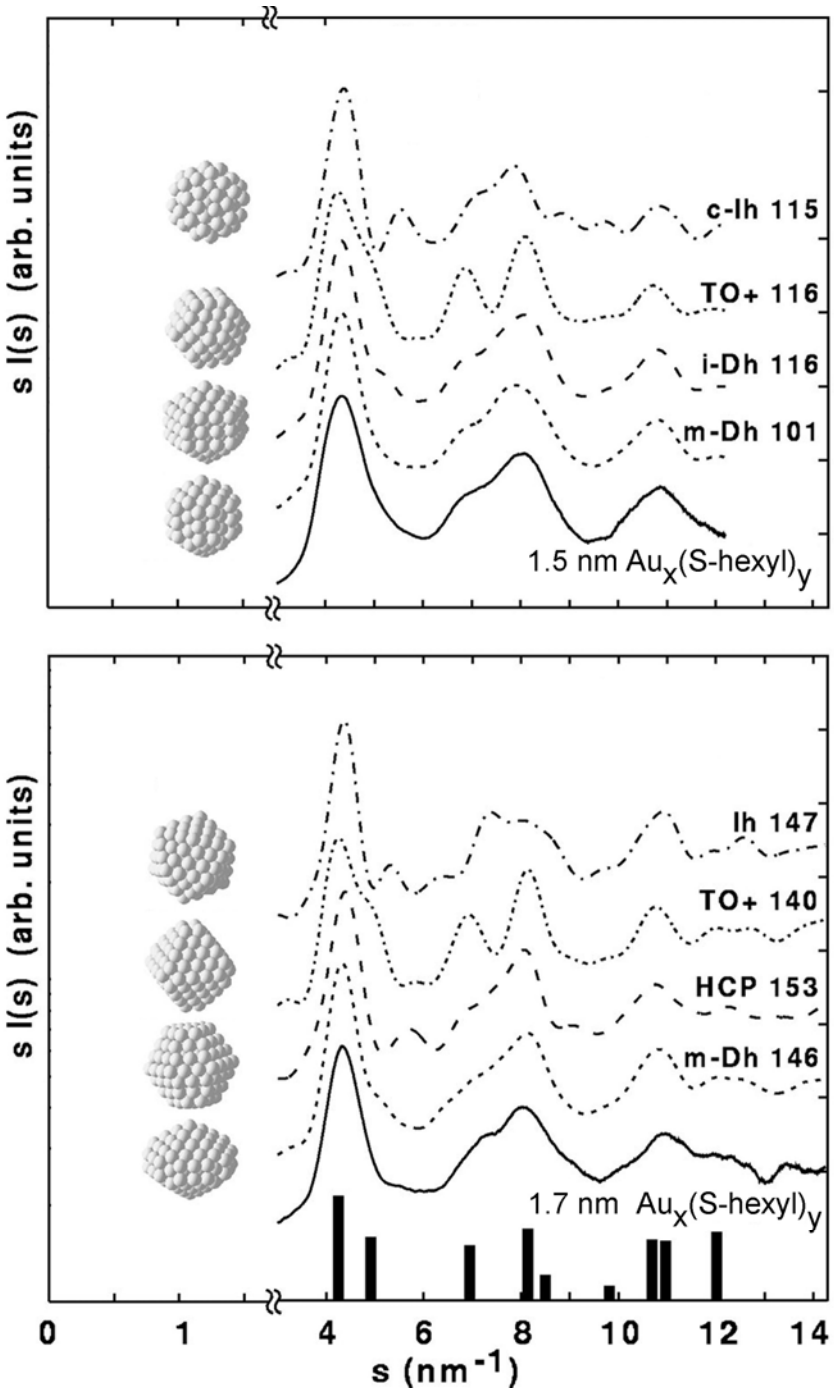


Figure 2.8 Calculated diffraction patterns of structural models compared to experimental results for 1.5 nm (top) and 1.7 nm (bottom) $Au_x(S\text{-hexyl})_y$ MPCs . Figure adapted from reference 21.

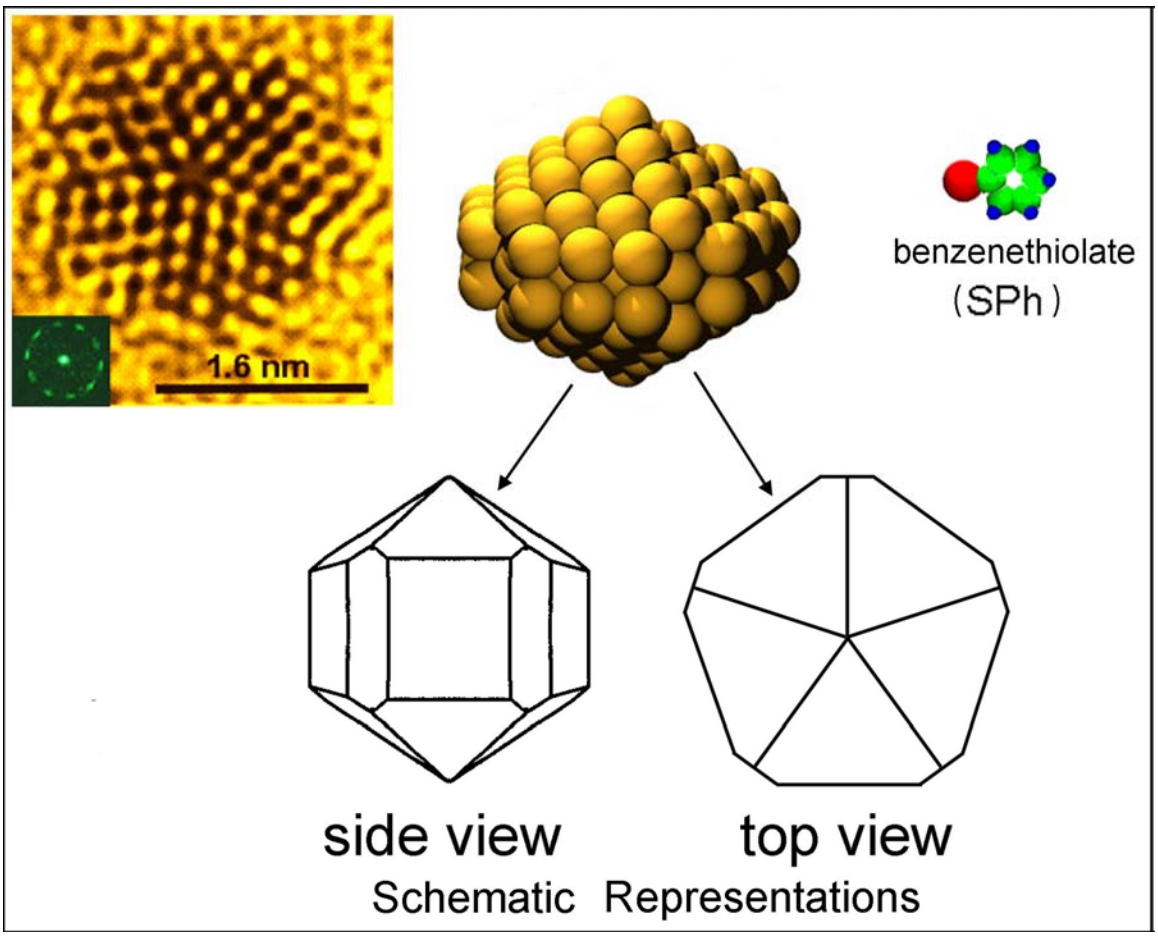


Figure 2.9 TEM image of a ~Au_{140}(S-hexyl)$_{56}$ quantum dot (left), Marks decahedral structural model (center), and benzenethiolate shown to scale (right). Note the numerous possible binding sites for the benzenethiolate ligand on the cluster surface. Figure adapted from reference 22.

2.3.2.2 Small Angle Diffraction (SAXRD)

Small angle x-ray diffraction (2θ=0-10^0; s=0-1.13 nm^{-1}) is used to determine if long range ordering is present between nanocrystalline cores. This type of ordering has previously been observed for 1.7, 2.0 and 2.5 nm $Au_x(S\text{-}(CH_2)_NCH_3)_y$ MPCs with N = 3 to 18 as a .82 to 1.68 nanometer edge to edge distance between adjacent nanoparticles within the superlattice. When adequately purified, the cluster cores can spontaneously form *bcc* or *fcc* arrays when slowly dried from solution, with edge-edge distances and

lattice type depending on the core diameter and alkanethiolate chain length.[22] Figure 2.10 shows SAXRD patterns for *bcc* arrays of 1.7 nm ~Au_{140}(S-alkyl)$_{56}$ MPCs with 1.0 and 1.6 nm edge-edge distances. An edge to edge distance of 0.8 nm is observed when butanethiolate is used as the passivation monolayer for the 1.7 nm cluster, but a smaller interparticle distance is observed for analogous $Au_x(SPh)_y$ clusters.

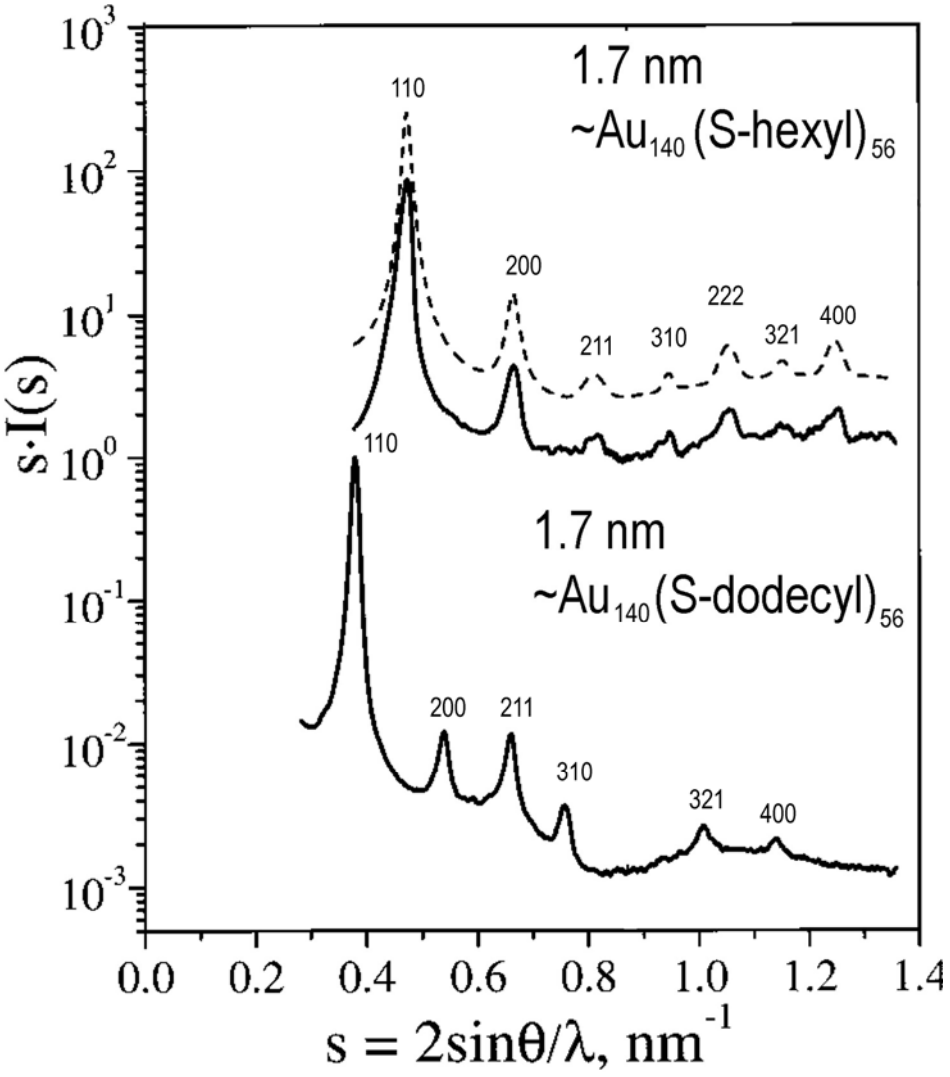


Figure 2.10 Logarithmic plot of scattering intensities for two nanocrystalline superlattices. Miller indices (hkl) are shown above each diffraction peak. Diffraction peaks appear at s values according to Braggs Law, $s = a^{-1}(h^2 + k^2 + l^2)^{1/2}$, where h,k,l are Miller indices and a is the lattice constant in *nm*. The lattice constants are 2.67 nm and 3.29 nm for hexanethiolate and dodecanethiolate passivated clusters, respectively.

The 1.5 and 1.7 nm Au_x(SPh)y MPCs have shown rudimentary ordering as a single, broad peak, similar to previous observations for polydisperse 2.7±1.0 nm Au_x(dodecanethiolate)$_y$ MPCs.[23] The small angle diffraction patterns of the two $TOA_NAu_x(SPh)_y$ MPCs are shown in Figure 2.11. The approximate edge-edge distance between 1.7 nm cores was .22 nm, while the 1.5 nm cores possess a .63 nm edge-edge distance. X-ray photon spectroscopy (XPS) has previously indicated benzenethiolate monolayers to be 0.1 to .15 nm thick on Au(111), which would yield at most ~ .30 nm edge-edge distance.[24,25] The greater than 3X interparticle distance in the 1.5 nm MPCs relative to the 1.7 nm MPCs arises from their possession of ~*six* bulky, disordered TOA counterions,

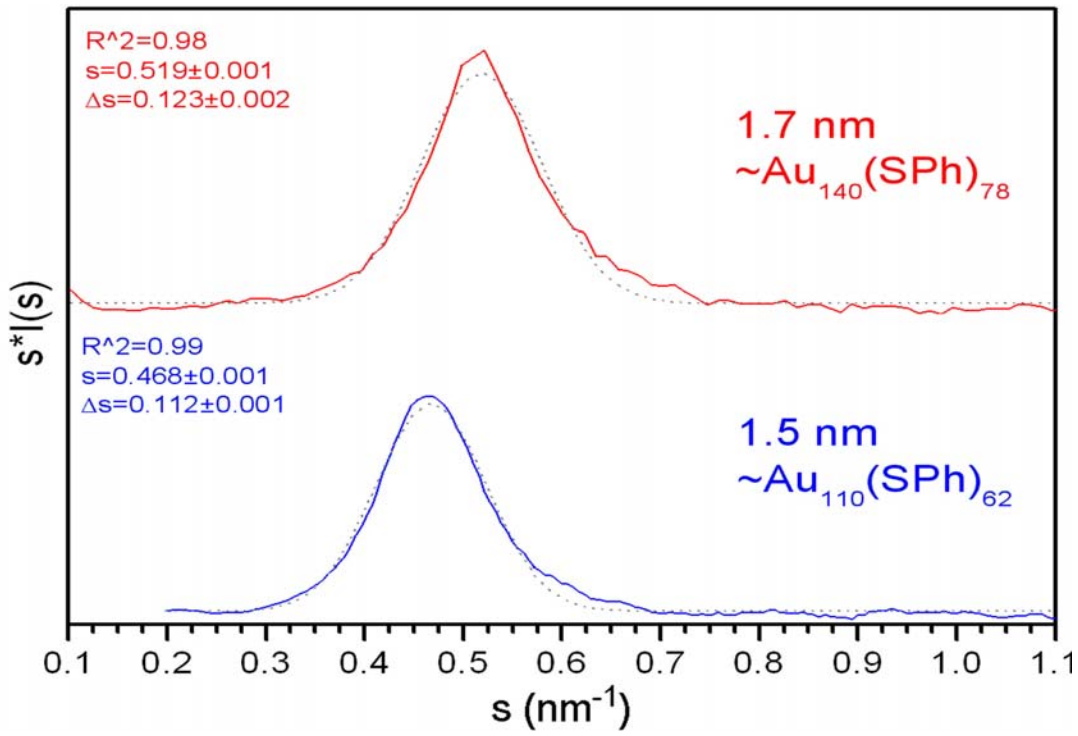


Figure 2.11 Small angle XRD for 1.5 and 1.7 nm Au_x(SPh)y MPCs. Dashed lines indicate Gaussian peak fits of the data. The values to the top left for each plot show its Gaussian fit correlation coefficient, peak location in nm^{-1} and peak FWHM in nm^{-1}. The reciprocal of the peak location provides the inter-particle core-core distance, while subtracting the large-angle diameter provides the edge-edge distance between clusters.

whereas the 1.7 nm MPCs only possess around three. The detection and quantification of TOA^+ within the cluster are detailed shortly in sections 2.3.4 to 2.3.6. The TOA^+ counterions also prevent the formation of highly ordered arrays or macroscopic crystals. The reciprocal of the small angle peak widths at half maximum indicate an average grain size of 8.1 nm for the 1.7 nm MPCs and 8.9 nm for the 1.5 nm MPCs, therefore the extended crystalline domains are ~ 4 nanocrystals in each dimension or about 64 nanocrystalline units in total volume.

STM size estimation from cross sectional profile scans of the 1.5 nm diameter core clusters of 1.7 nm indicate a compact, ~.10 nm thick benzenethiolate monolayer. [26] This would be consistent with .20 nm edge-edge distances without any intercalation interactions occurring between adjacent cluster monolayers, thus it is likely the TOA^+ serves to increase inter-particle distances as well as decrease bulk crystallinity. Figure 2.12 shows an STM image of the 1.5 nm clusters cross sectional height profile scans. Limited attempts to improve the crystallinity of these and other MPCs have been ineffective. All data presented in this chapter were collected with a Scintag Inc. X-GEN 4000 powder diffractometer. Each sample was prepared by dissolving ~10 mg of powdered sample in 100 μL of toluene. This solution was deposited on Si_{111} (miscut 5^o) in 10 μL aliquots with air-drying between each aliquot to form a thin film.

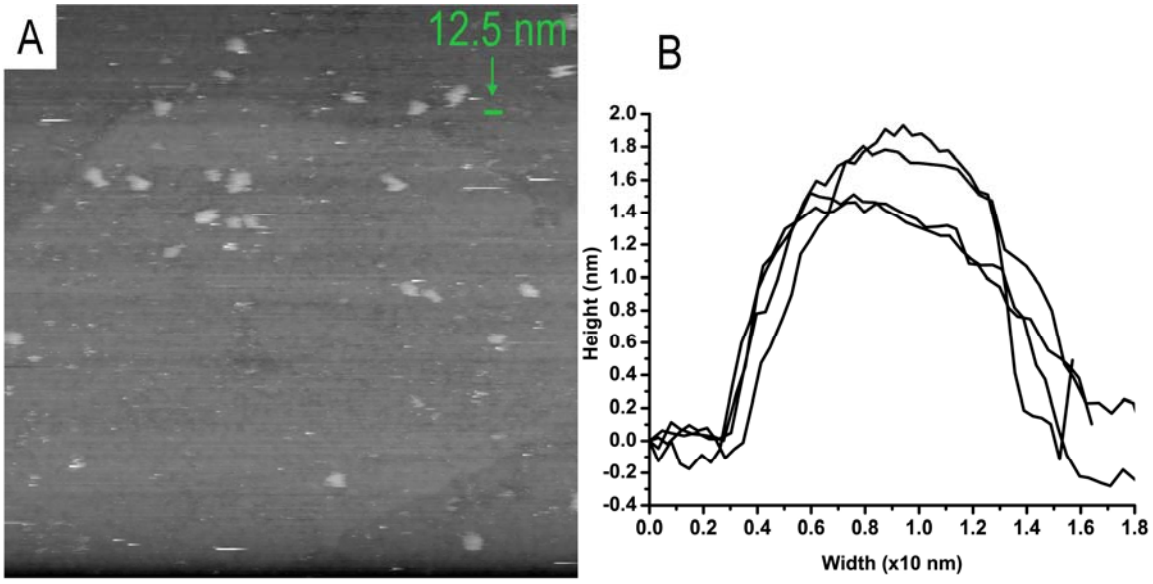


Figure 2.12 (A) 200 x 200 nm area STM scan at room temperature for 1.5 nm core ~$(TOA)_6Au_{110}(SPh)_{62}$ MPCs. Horizontal features are routinely exaggerated by a factor of ~10x due to particle-tip interactions. [100 pA set point current, -1 V tip bias] (B) Cross-sectional profile scans of four MPCs yielding a 1.7 nm average height (total diameter). Images provided by Dr. Jianfei Shao.

2.3.3 Matrix Assisted Laser Desorption Ionization Mass Spectrometry (MALDI-MS)

Mass spectrometry has proven an invaluable tool for the characterization of purified gold MPCs, allowing identification of polydisperse colloidal up to 160 kDa (~800 Au) and size fractionated gold:alkylthiolate MPC samples with core masses as low as 8 kDa (~40 Au).[6,13,27,28] The MPCs are inherently hydrophobic, hence insoluble in electrospray ionization solvents such as water, acetone, or acetonitrile. Matrix-assisted laser desorption ionization (MALDI) has proven effective for transferring gold:thiolate MPCs into the gas phase and accelerating the ions into a mass spectrometer. The inherently high molecular weights (~1 kDa per 5 Au) of the MPC cores are best detected by linear time of flight (TOF) mass spectrometry, which is often employed for biomolecules in this mass range and beyond. MALDI-TOF-MS spectra can determine the

approximate number of gold atoms from the center of a mass spectral peak and the number of sulfur atoms bound to the core estimated from the full width at half max (FWHM) of the mass spectral peak.[29]

Before the precise diameter of the toluene soluble $Au_x(SPh)_y$ MPCs were known, a series of size/solubility separated samples were prepared by dissolving 25.7 mg of the clusters at 1 mg/mL in 25 mL of toluene. A beaker of this constantly stirred solution was sealed in a desiccator over acetone, allowing passive vapor transport to slowly precipitate the largest clusters. The solution was checked daily over the course of a month for insoluble, precipitated clusters, that were collected by filtration through a .16 μm syringless filter, re-eluted with toluene, dried, then massed to allow purity estimates. A total of 11 materials were collected and analyzed at Oak Ridge National Laboratory in collaboration with Dr. Greg Schaaff. Briefly, ~ 0.1 mg of each MPC sample was diluted in ~100 mg of a sinapinic acid (3,5 dimethoxy-4 hydroxy cinnamic acid) matrix in ~10 μL of dichloromethane and dried before analysis. The mass spectra were collected by MALDI-TOF on an Applied Biosystems Perspective linear TOF mass spectrometer operating in negative ion detection mode and equipped with a VSL-337 ND pulsed N_2 laser with a 4 ns pulse width at 337 nm, typically delivering 2-3 MW/cm^2 to the target (analyte).

The varying materials isolated by slow precipitation fell into only three categories, and their mass spectra are shown in Figure 2.13. The dominant peak in the spectra, representing 87.2 % of the mass isolated, comprised a mass spectral peak at 21.6 with peak FWHM of 2.0 kDa, values indicative of an ion of composition ~$Au_{110}S_{62}^-$.

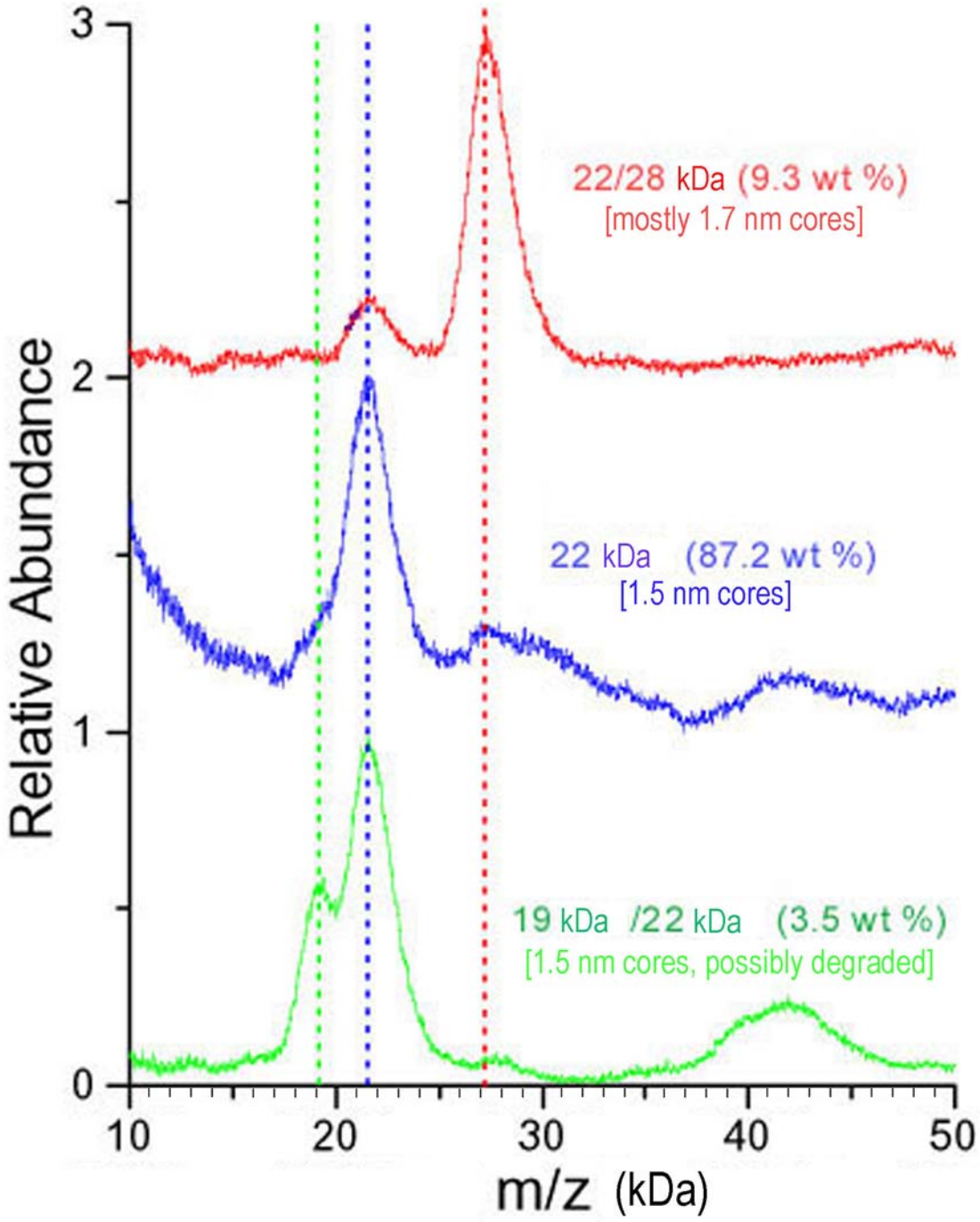


Figure 2.13 MALDI-TOF-MS of size fractionated 1.5 nm $Au_x(SPh)_y$ MPCs. The average core mass is shown for each set of materials isolated and their percent abundance by mass in the isolated product is shown. The higher mass peaks above 40 kDa in the two lower spectra are dimeric anions of the clusters.

The 21.6 kDa fractions collected precipitated on days 7 through 19 and had indistinguishable mass spectra. Below 9.3 % of the material produced an ion with a mass spectral peak at 27.2 kDa with peak FWHM of 2.5 kDa, indicating an ion of composition ~$Au_{140}S_{78}^-$. This same mass spectrum was observed for the dichloromethane soluble material described in section **2.2,** verifying its identity as a 1.7 nm core MPC. The gold to sulfur ratios, and hence the gold to benzenethiolate ratios, are 1.77 for the 1.5 nm core MPCs and 1.79 for the 1.7 nm core MPCs. These ratios are consistent with elemental and thermogravimetric analysis data described shortly.

The final mass fraction isolated during precipitation represented only 3.5 % of the total mass and showed some indication of a ~19 kDa material. It should be noted the MPCs were in contact with the toluene/acetone solution for thirty days at this point and it was subsequently discovered the MPCs become unstable upon prolonged exposure to acetone. There is no precedent for gold MPCs with this core mass and it has not been observed in fresh, non-size separated samples. Sample degradation by electrochemical degradation and oxidation by acetone is the most likely explanation.

2.3.4 Elemental and Thermogravimetric Analysis

2.3.4.1 Elemental Analysis

Atomic absorption elemental analysis was performed by Galbraith Laboratories for two different samples of $Au_x(SPh)_y$ MPCs prior to implementation of rigorous tetraoctylammonium bromide (TOABr) extraction procedures. The first sample analyzed was composed of a mixture of both clusters sizes, thus was of limited use. The presence of excess TOABr within both samples yielded excessively high ratios of carbon and hydrogen relative to the aromatic moieties present with each sulfur atom. Detectable levels of nitrogen 0.7 % or less by weight, a value too close to the 0.5 % detection limit of the Kjeldahl nitrogen method to be of quantitative use.

The second sample evaluated by Galbraith consisted of relatively pure 1.5 nm $Au_x(SPh)_y$ MPCs that were eluted by toluene. The weight percentage for each element evaluated were: 45.06 % Au, 36.47% C, 5.10 % H, 4.10% S, .74 % N, and 1.28 % Br. Applying the molar ratios determined from these weight ratios yields $TOA_{31\text{-}33}[Au_{110}(SPh)_{62}]Br_8$ as a molecular formula. This formula has a 1.77:1 Au to S ratio, matching the 1.77:1 ratio estimated from mass spectral data. This shows little difference between the two methods for the 1.5 nm $Au_x(SPh)_y$ MPCs.

2.3.4.2 Thermogravimetric Analysis

Further analysis of the 1.5 and 1.7 nm core $Au_x(SPh)_y$ clusters was performed with a TA Instruments TGA 2950 located in the Georgia Institute of Technology Materials Science Department. Samples analyzed in this fashion were rigorously purified by acetonitrile extraction to remove excess TOABr. Each sample was heated from room

temperature to at least 450 ^{o}C at a rate of 10 ^{o}C/minute under a continuous nitrogen purge and held at 450 ^{0}C or higher for ten minutes to ensure complete removal of all volatile material, leaving only elemental gold. The 1.5 nm core MPCs contained 28.0 % volatile material, while the 1.7 nm MPCs contained 25.0 % volatile material. These values are not consistent with MPCs composed solely of gold and benzenethiolate which would have mass losses of 23.8 % and 23.5 % for 1.5 and 1.7 nm cores, respectively. Assigning the additional mass loss as TOA^{+} yields compostions of $(TOA)_4[Au_{110}(SPh)_{62}]$ and $(TOA)_2[Au_{140}(SPh)_{78}]$, which should contain volatile material within 1.8 % of the experimentally measured values. The levels of TOA^{+} present are 33 % lower than previously estimated by ^{1}H-NMR, discussed in **2.3.5**. The TGA data for the MPCs, as well as the insoluble reaction by-product are shown in Figure 2.14.

Thermogravimetric analysis of the grayish, insoluble by-product from MPC synthesis (detailed in **2.2)** indicated 29.2 % volatile material. It appeared more thermally stable than the $Au_x(SPh)_y$ MPCs, evidenced by continued mass loss beyond 300 ^{o}C. This insoluble material was thoroughly rinsed with water, acetone, methanol, ethanol, toluene, dichloromethane, and hexanes to ensure removal of all soluble and volatile material before TGA analysis. It was insoluble in concentrated hydrochloric, nitric, and sulfuric acids, and was only partially dissolved by aqua regia on a time scale of 24 hours, implying resistance to oxidation and the likely presence of gold in its highest oxidized state of +3. The reactants contained 4 chloride anions and 1.2 bromide anions for each gold atom present, making a $[Au(SPh)(halide)_2]_x$ complex or compound formation not unreasonable. Such a complex is consistent with aqua regia insolubility. Feasible

compositions are given in Figure 2.14 for this material with computed mass loss percentages.

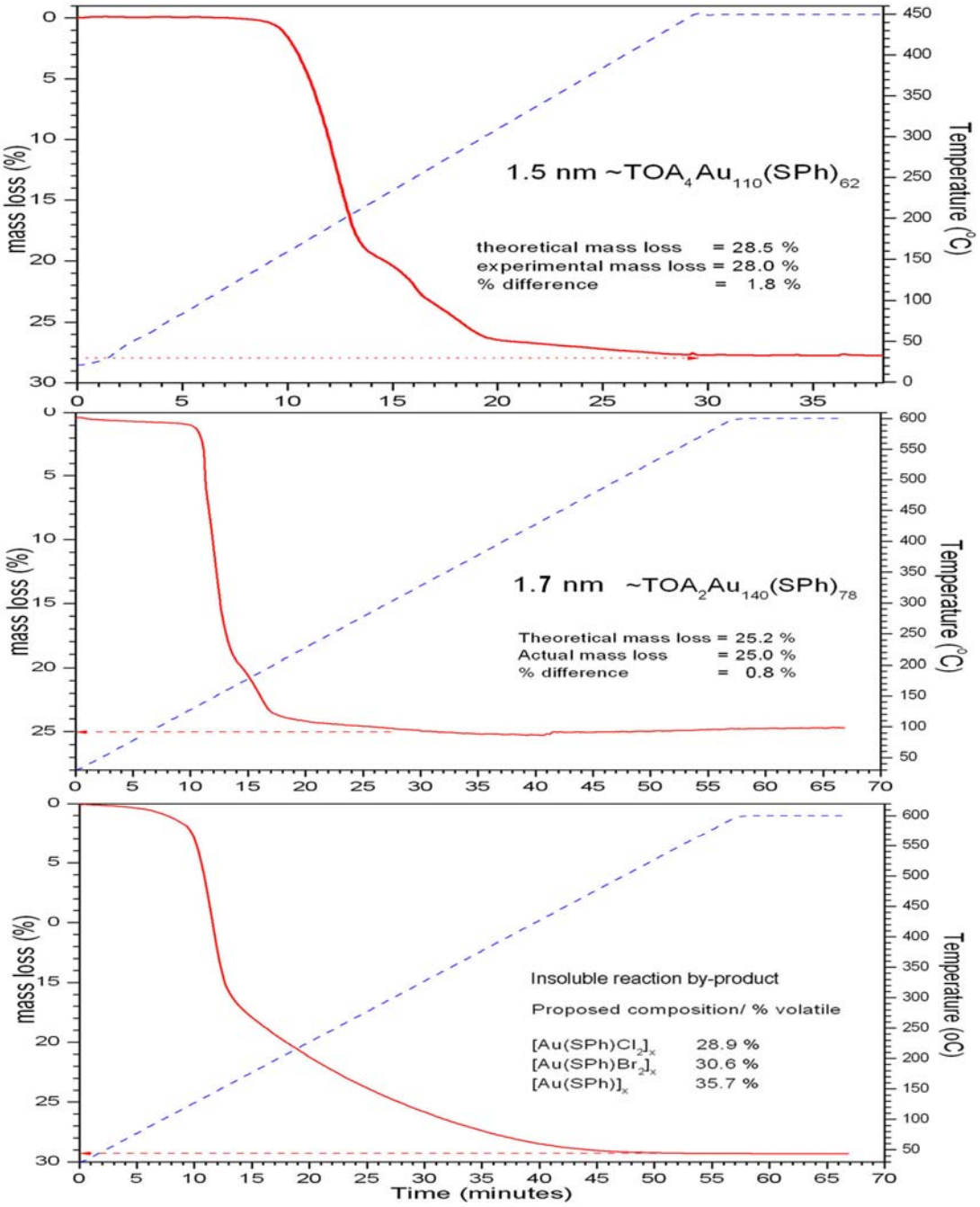


Figure 2.14 Thermogravimetric plots for 1.5 nm (top), 1.7 nm (middle), and reaction by-product (bottom) from $TOA_zAu_x(SPh)_y$ MPCs. Red plots are mass loss %, with a the red dashed line guiding the eye to the y-axis. The blue dashed line indicates the temperature, read from the right axis.

2.3.5 Proton Nuclear Magnetic Resonance (^{1}H-NMR)

Proton and carbon nuclear magnetic resonance (^{1}H and ^{13}C-NMR) have been applied qualitatively to $Au_x(alkylthiolate)_y$ MPCs with core dimensions from 1.7 to 5.2 nm and three to eleven methylene units in the alkane backbone.[6,30] The tripeptides glutathione and tiopronin have also been investigated on gold MPCs with 0.8 (28 atoms) to 2.0 nm (~200 atoms) cores.[31,32] The ^{1}H and ^{13}C NMR signals for the α and β atoms proximal to the sulfur atoms are consistently broadened and display diminished intensity, although use of a high field spectrometer ($\geq$ 400 MHz) allows integration of the ^{1}H-NMR signals to yield intensities expected for the appropriate alkanethiols.[6] The Murray group at UNC Chapel Hill have extensively investigated the line-broadening and loss of sharp spectral features for dodecanethiolate on Au cores ranging from 1.7 to 5.2 nm, finding more pronounced, sharper features for $\leq$ 2.0 nm clusters.[31] They have additionally reported tiopronin on ~1.7 nm Au cores is significantly more broadened and diminished than on ~1.0 nm cores.[32] Plausible explanations for this behavior put forth by Murray et al. are:

(1) Spin-spin relaxation (T_2) from rotation of the clusters would give smaller, faster rotating clusters less broadening.

(2) A Knight's shift of the chemical shifts downfield (higher ppm) due to more metallic conductivity in larger clusters would give broader peaks for larger clusters.

This information implies the ^{1}H-NMR spectra of 1.5 and 1.7 nm core diameter $Au_x(SPh)_y$ MPCs should yield broad, diffuse spectra with some retention of sharp spectral features and sharper spectral features for the 1.5 nm core.

The ^{1}H-NMR spectra of the MPC aromatic region shown in Figure 2.15 indicate the expected trend of increased broadening at larger diameter, but the aromatic chemical shifts appear both upfield and downfield from similar hydrogen atoms in both benzenethiol and diphenylsidulfide. This could arise from some polydispersity (of $\leq$ 10 Au atoms) within the samples and/or differing binding sites on the cluster surface. The clusters are as monodisperse as possible based on the mass spectrometric results in chapter 2.3.3, leaving multiple binding modes as a more likely explanation for the many peaks present in the ^{1}H-NMR spectra. There are definitely three doublets and up to three more possible doublets present in the spectrum of the 1.5 nm MPCs, with each doublet corresponding to one or two ortho protons of an aromatic ring. This suggests three to six binding sites, with no guarantee that the two orthogonal hydrogens are in similar chemical environments, as one could be tilted much closer to the gold surface than the other, making the two magnetically non-equivalent. Attempts to resolve this matter using 2-D COSY NMR did not produce data that sufficiently indicated the ^{1}H -^{1}H couplings within each type of aromatic ring present. Numerical comparison of the chemical shifts for the dominant peaks in the spectra of Figure 2.15 and reference benzenethiolates is given in Table 2.1. From table 2.1 it is interesting to note that the J-J coupling values for the ortho and meta hydrogen listed of the clusters resemble those of diphenyldisulfide, rather than benzenethiol, but the nature of the gold-thiolate interaction can not be

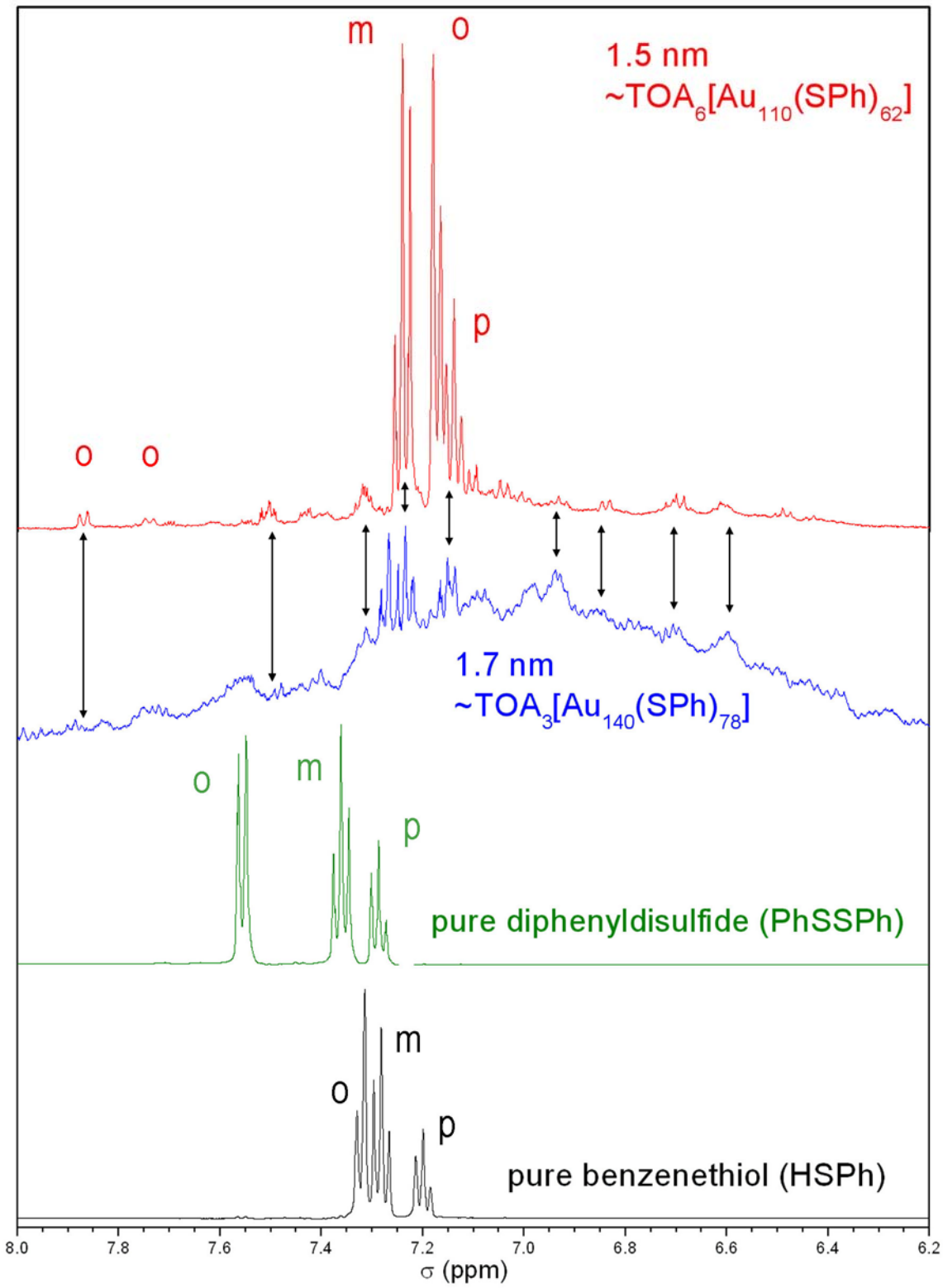


Figure 2.15 ^{1}H-NMR spectra of 1.5 and 17 nm $TOA_N[Au_x(SPh)_y]$. (O)rtho, (m)eta and (p)ara hydrogen atoms are clearly labeled where apparent. Spectra were collected as saturated solutions in CD_2Cl_2 (Cambrige Isotopes) on a Bruker DRX-500 spectrometer.

Table 2.1 Chemical shifts, peak appearances, and J-J coupling constants for dominant ^{1}H resonances in diphenyldisulfide (PhSSPh), benzenethiol (HSPh), and $Au_x(SPh)_y$ MPCs.

Chemical shift,appearance, J_{H-H}

	Ph-S-SPh	H-S-Ph	~$Au_{110}(SPh)_{62}$	~$Au_{140}(SPh)_{78}$
ortho	7.56,doublet,3.8 Hz	7.32,doublet, 8.0 Hz	7.17, doublet, 3.5 Hz	7.23, doublet, 3.0 Hz
meta	7.36, triplet, 7.5 Hz	7.28, triplet, 4.0 Hz	7.24, triplet, 7.5 Hz	7.27, triplet, 8.0 Hz
para	7.29, triplet, 7.5 Hz	7.20, triplet, 8.0 Hz	7.14, tiplet, 7.5 Hz	7.15, triplet, 8.0 Hz

reconciled from this information. Attempts to further resolve this matter with ^{13}C-NMR spectroscopy were unsuccessful.

The full ^{1}H-NMR spectra of the clusters from 0 to 9 ppm consistently revealed the presence of alkane hydrogens, matching well with tetraoctylammonium, but absent the α methylene hydrogen signals present in TOABr at ~3.2 ppm. The full ^{1}H-NMR spectra for the 1.5 and 1.7 nm $TOA_NAu_x(SPh)_y$ MPCs are shown in Figure 2.16. The presence of silicone grease contamination from the laboratory rotovap, evident at 1.2 ppm in the spectra, consistently prevented reliable use of the full alkane region of the spectra for determining TOA to benzenethiolate ratios. Fortunately, the methyl protons at ~0.9 ppm and the β-methylene protons at ~ 1.6 ppm had a consistent 1:1 ratio between different syntheses, allowing an estimated aromatic to alkane ratio of 1.9 to 3.3. Scaling this ratio for the ~62 benzenethiolates per 1.5 nm cluster gives 6 $\pm$ 2 TOA per cluster. These estimates were determined from the four spectra in Figure 2.17.

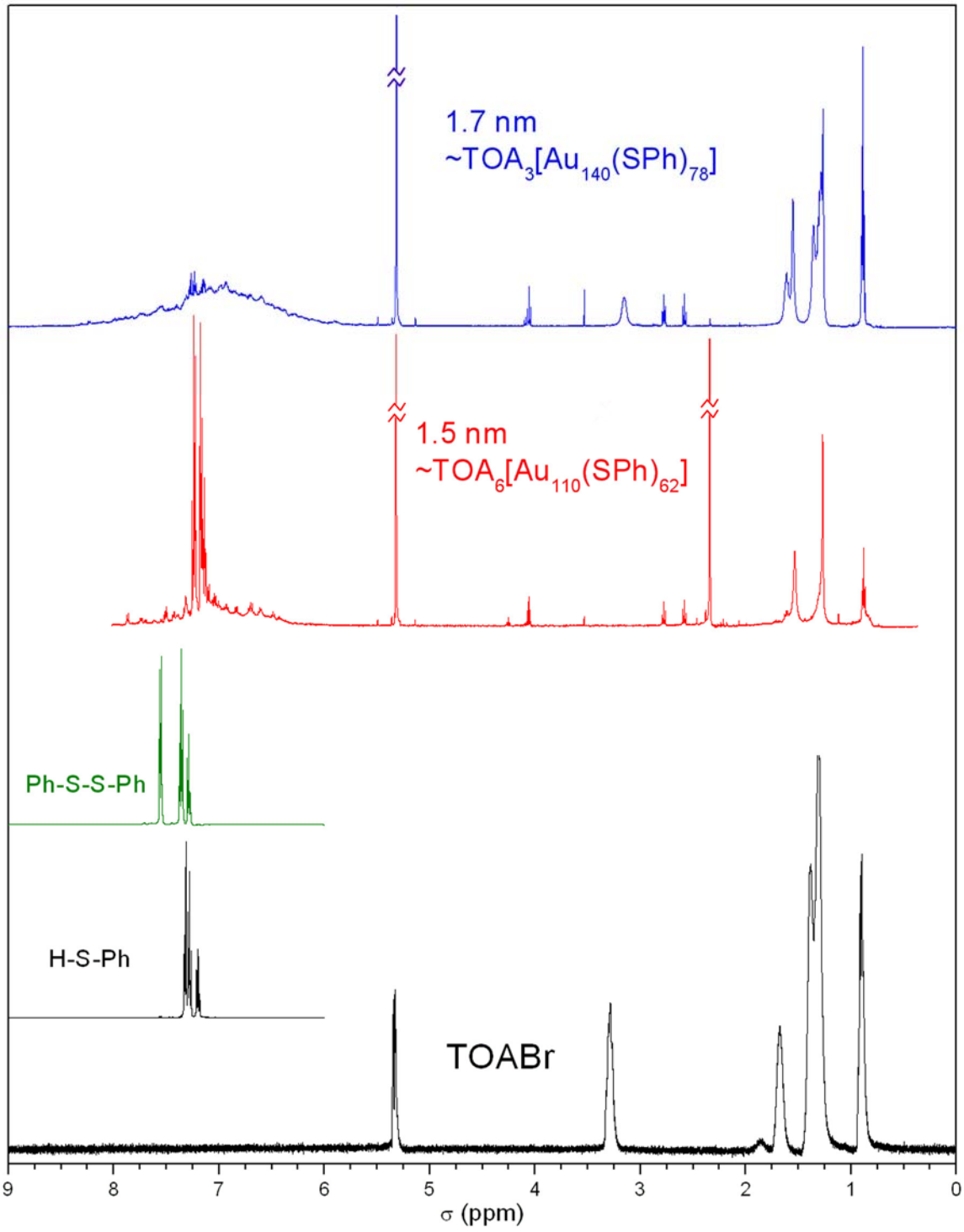


Figure 2.16 Full ^{1}H-NMR spectra of 1.7and 1.5 nm $Au_x(SPh)_y$ MPCs with standards, including TOABr. The absence of a strong a methylene peak from TOABr at 3.1 ppm argues against TOABr as a contaminant in the MPCs, while the consistent appearance of methyl and β-methylene protons indicate TOA^+ with the α-methylene possibly suppressed by the presence of the anionic gold core.

For the 1.7 nm $Au_{140}(SPh)_{78}$ clusters, using the ratio of the integrated aromatic proton resonances to the 0.9 ppm methyl proton resonances yields a 11.8:1.00 ratio, consistent with three TOA cations per $Au_{140}(SPh)_{78}$. Figure 2.18 shows an integrated spectrum for the1.7 nm MPCs. It is important to note that any suppression (diminishment) of the aromatic signal from ligand proximity to the gold core would give erroneously high ratios of TOA^+ to benzenethiolate, thereby reconciling the ^{1}H-NMR estimates with the lower values determined subsequently by TGA.

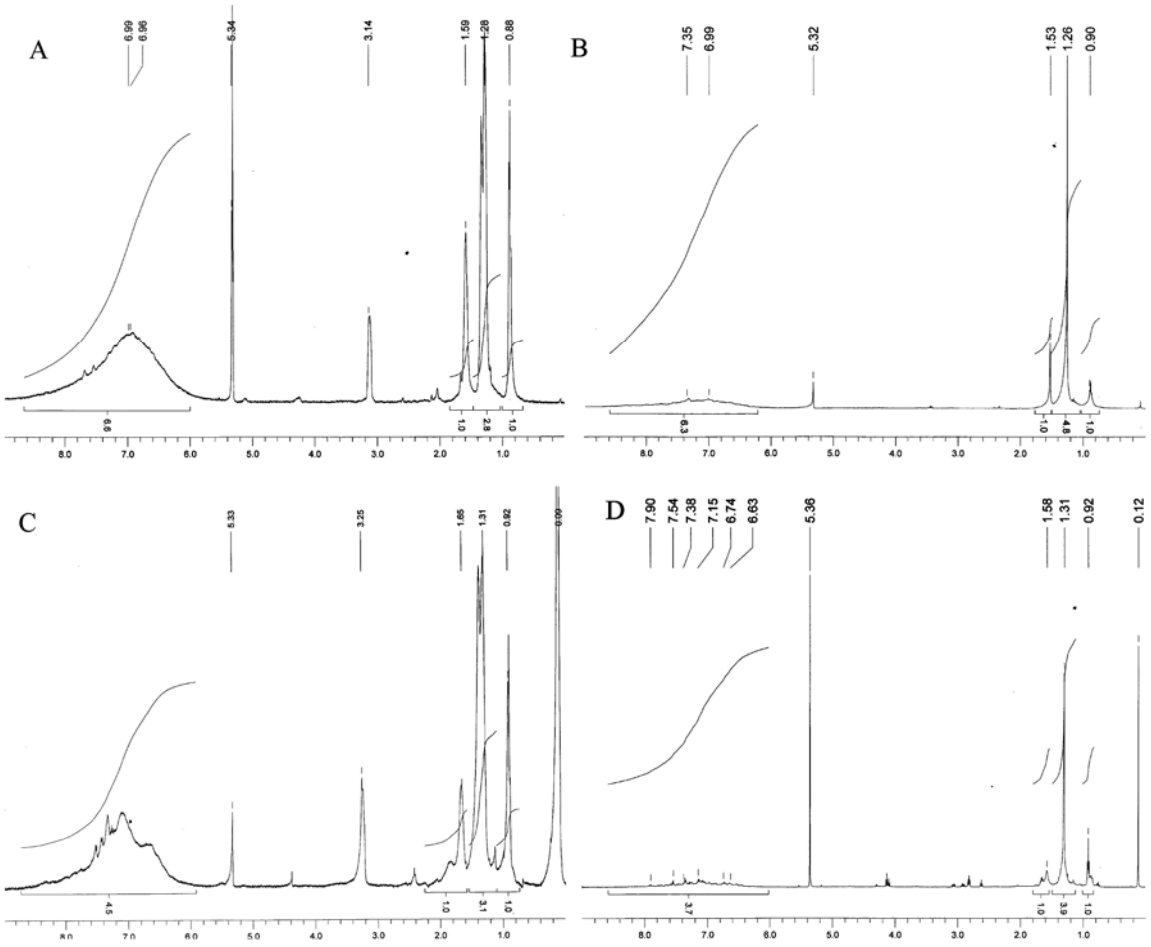


Figure 2.17 ^{1}H-NMR spectra of four ~TOA$_N$[Au$_{110}$(SPh)$_{62}$]MPC samples. Estimates of the aromatic to methyl/methylene integration intensities for the spectra and their ratio when scaled for 62 aromatic moieties (determined from EA and MS) are:

	aromatic:alkyl	S-Ph:TOA
A	3.3	62:5
B	3.2	62:5
C	2.3	62:7
D	1.9	62:8

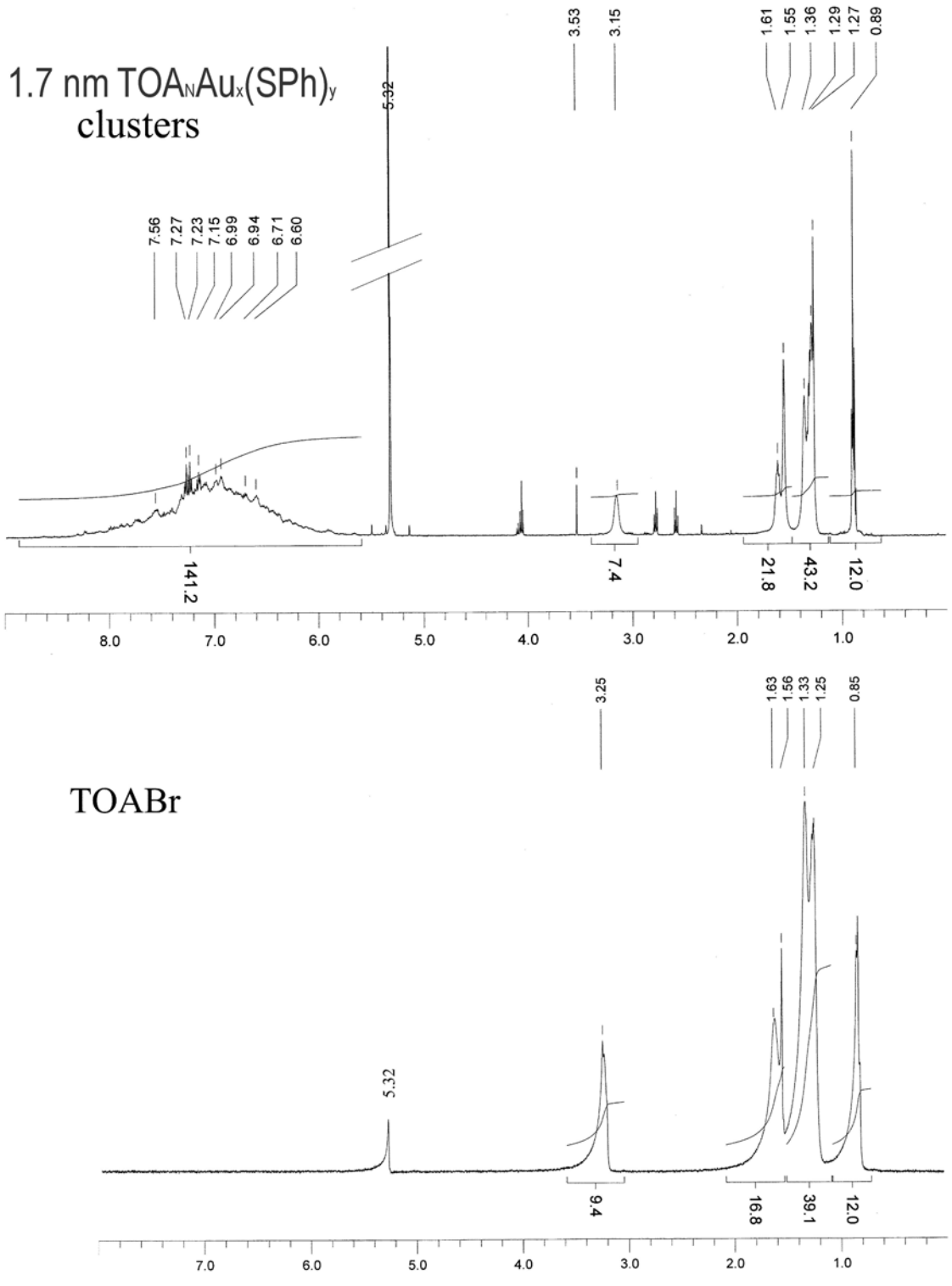


Figure 2.18 ^{1}H-NMR spectrum of 1.7 nm ~TOA$_N$[Au$_{140}$(SPh)$_{78}$] clusters. Only the methyl resonance was used for estimating aromatic to alkyl content. If the total alkyl signal integration is counted as TOA, an estimated ratio of 78 benzenethiolate to 3.4 TOA+ ratio results.

2.3.6 Infrared and Raman Spectroscopy

2.3.6.1 Infrared Spectroscopy

Infrared spectroscopy has been applied only sparingly for characterizing gold MPCs. It is exceptionally useful as a fast method for verifying the absence of excess thiol remaining from cluster synthesis, as the S-H stretch at 2560 cm^{-1} is prominent in free thiol, but absent in the IR spectra of gold MPCS. Murray et al. at UNC Chapel Hill exhaustively studied the infrared spectra of polydisperse 2.6±0.2 nm core colloids with alkanethiols ranging in chain length from three to 24 carbons.[33] The salient findings were that chains longer than 6 carbon atoms have more gauche (non-trans) defects than shorter chains and the MPC spectra resemble earlier reports of 2-D self-assembled monolayers on flat gold surfaces.[34] The alkanethiol monolayers on gold display enhanced ordering relative to free alkanethiol, indicated by methylene symmetric and anti-symmetric frequency increases of 6-8 cm^{-1} relative to unbound liquid alkanethiol. Murray also reported the dominant aryl infrared absorption bands for benzenethiol on the surface of 1.9 to 6.5 nm gold colloids as aryl C-H →3052 cm^{-1}, aryl C=C →1573 cm^{-1}, 1470 cm^{-1}, and 1435 cm^{-1}, values which are consistent with the results on 1.5 and 1.7 nm $Au_x(SPh)_y$ MPCs.[35] The infrared spectra of 1.5 and 1.7 nm Aux(SPh)y MPC are shown in Figure 2.19 and contain twice as many clearly defined absorption bands as a previous report with surface-enhanced infrared absorption spectroscopy(SEIRAS) utilized to analyze benzenethiol adsorbed on Au(111).[36] The MPC absorbance bands in relation to pure benzenethiol are given in table 2.2.

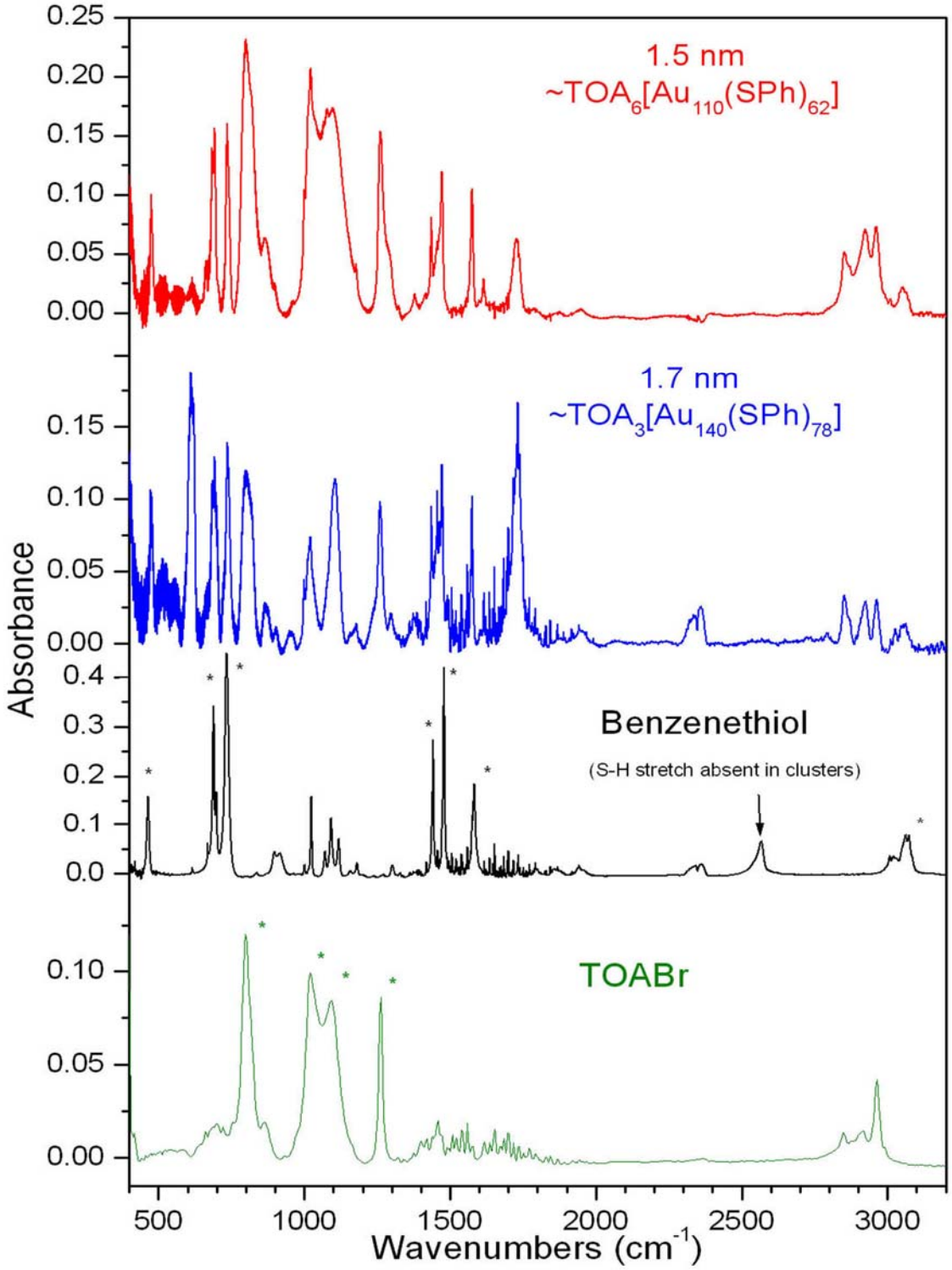


Figure 2.19 Infrared spectra of $TOA_N[Au_x(SPh)_y]$ MPCs with benzenethiol and tetraoctylammonium bromide. Asterisks (*) denote prominent features of benzenethiol and TOA present in the clusters. While qualitative, the presence of more TOA in the 1.5 nm MPCs is apparent from the enhanced absorbance features between 900 and 1200 cm^{-1}. All MPCs lack the 2567 cm-1 S-H absorbance feature.

Infrared spectra were collected with a Nicolet 520 FT-IR Spectrometer. The samples were prepared by dissolving the clusters in toluene at a concentration of ~10 mg/mL and depositing a thin film containing ~3 mg of clusters onto a KBr disk, followed by drying at room temperature. The lack of the S-H stretch at 2567 cm^{-1} indicates that benzenethiol is covalently bound to the gold. The shift of the aryl C=C absorbance bands between 1583 cm^{-1} and 1442 cm^{-1} to frequencies that are 6 to 10 cm^{-1} lower indicate softening of the ring modes. This phenomenon has also been observed in Raman spectra of benzenethiol chemisorbed on bulk gold and has been attributed to tilting of the aromatic ring towards the surface in bulk gold ($<90^{o}$ to surface normal).[37] The dominant infrared absorbance bands observed for tetraoctylammonium (TOA^{+}) are virtually unchanged when associated with gold MPCs and their constant presence in the MPC IR spectra even after rigorous purification was the first indication that TOA^{+} was a cation, rather than a TOABr contaminant. Subsequent analysis by Raman spectroscopy produced significantly more information about the bind of benzenethiolate in $TOA_{N}[Au_{x}(SPh)y]$.

Table 2.2 Tabulated dominant IR bands for 1.5 and 1.7 nm $TOA_N[Au_x(SPh)_y]$ clusters. Strong absorbance bands ($\geq$50 % relative intensity) are listed in red, weak to moderate (<50 % relative intensity) are in green. Benzenethiol adsorbed on bulk Au(111) has been reported in reference 16 to give the following IR absorbance bands: 3060 cm^{-1}(weak),1574 cm^{-1}(weak), 1472 cm^{-1}(strong), 1068 cm^{-1} (weak), 1026 cm^{-1}(moderate), 1000 cm^{-1} (weak). Mode assignments from reference 36.

pure benzenethiol	1.5 nm Au clusters	1.7 nm Au clusters	notes/description	mode
3060	3066	3053	aromatic C-H stretch	a_1
3010			aromatic C-H stretch	
2560	-	-	S-H stretch	
1940	1950	1941	overtone	
1855	1876		overtone	
1795	1799	1726	overtone	
1583	1573	1575	aromatic C=C stretch	b_2
1479	1468	1471		a_1
1442		1436	aromatic C=C stretch	b_2
1118	1132			a_1
1093		1099		a_1
1070	1069	1077	aryl-C-S stretch	b_2
1025	1020	1021	aryl-C-S stretch	a_1
1000				a_1
920	-	-	S-H bend	
895			overtone	
734	735	736	C-H bend	b_1
699			overtone	
689	689	691	C-S stretch (in plane)	a_1
465	475	475	C-S bend (out of plane)	a_2

2.3.6.2 Raman Spectroscopy

Raman scattering by thiolate monolayers on noble metal bulk and colloidal surfaces has been intensively studied for the information it provides on the structure and bonding of the adsorbate groups.[38a-c] Applying this method to the 1.7- and 1.5-nm $Au_x(SPh)_y$ MPCs indicates they have many features in common with polymeric $[Au^{(I)}SPh]_x$, similar to earlier reports of benzenethiolate (-SPh) and diphenyldisulfide (DPDS) on roughened gold electrodes.[39a-c] While this provides an enhanced understanding of benzenethiolate binding on small gold MPCs, a complete understanding of the gold thiolate interaction remains elusive.

The nature of the bonding in gold-thiolate monolayers on extended crystalline surfaces is not fully understood, but disulfide species are generally not detected, with the exception of 4-pyridinethiolate on Au(111).[40] Surface spectroscopic measurements of benzenethiolate self-assembled monolayers (SAMs) have determined a 76^0 tilt angle from surface normal for the aromatic ring.[39c] This is consistent with the compact monolayers evident from the small edge-edge MPC distances detected by SAXRD (section 2.3.2.1). Benzenethiolate on Au (111) has been reported to form no ordered phases[41], however, more recent work by Osawa et al. found a nearly $(\sqrt{13} \times \sqrt{13})R13.9°$ monolayer symmetry with a ~30^0 ring tilt angle from the surface normal in aqueous solution.[36] It seems likely that solvent and thiol concentration during benzenethiol chemisorption at *crystalline* surfaces may determine the characteristics of the monolayer formed, and could differ greatly from benzenethiolates on small clusters formed via the complete reductive degradation of a $[Au^{(I)}$:thiolate$]_x$ polymer method utilized in this research. In contrast to the earlier assumptions (implicit or explicit) that the structure of the outermost

metal layer is unmodified by SAM formation, several recent experimental and theoretical reports assert a substantial reconstruction of noble-metal surfaces by bound thiolates.[42a-h]

Raman spectra for the MPCs, the $[Au^{(I)}SPh]_x$ polymer, NaSPh, and diphenyldisulfide are shown in Figure 2.20. The MPCs and $[Au^{(I)}SPh]_x$ polymer have similar relative intensity enhancement of vibrations at 1582 cm^{-1} (a_1), 1070 cm^{-1} (b_2), and 416 cm^{-1} (a_1), relative to the 999 cm^{-1} a_1 mode. There are several noteworthy spectral features, the most prominent being the appearance of a *cis oriented* diphenyldisulfide S-S stretch in the 1.5 nm $Au_N(SPh)_M$ cluster spectrum at 507 cm^{-1}. Splitting and shifting of the diphenyldisulfide S-S stretch at 542 cm^{-1} to 515 cm^{-1} (trans) and 505 cm^{-1} (cis)are known for DPDS in the solid state on Ag(0).[43] The next feature of interest is the softening of the ~1570 a_1 mode to 1559 cm^{-1}, possibly arising from a tilt of the aromatic ring towards the gold surface, as reported for benzenethiolate on iron and platinum.[43] Another noteworthy feature unique to the $Au_x(SPh)_y$ MPCs is a significant relative intensity enhancement of the 1272 cm^{-1} b_2 mode by 3X – 4X.This mode represents (Figure 2.21) an in-plane bend of the ring with the carbons twisting in unison as the hydrogen and sulfur atoms all twist in unison in the opposite direction, thereby breaking the C_{2v} symmetry of the molecule. This is consistent with a tilt of the benzenethiolates toward the gold surface, rather than being perpendicular to the gold surface. If this is the case, the two orthoganol hydrogen atoms may not be equivalent to one another, although the expected high curvature of nanocrystal surfaces prevents estimation of surface geometry. Lastly, no evidence of Au-Cl vibrations at 324 or 347 cm^{-1} or Au-Br vibrations at 202 or 212 cm^{-1} are observed in the $Au_N(SPh)_M$ MPCs, indicating no gold-halide bonds to induce a metal to insulator transition, such as those observed in $Au_{55}(PPh_3)_{12}Cl_6$.[44]

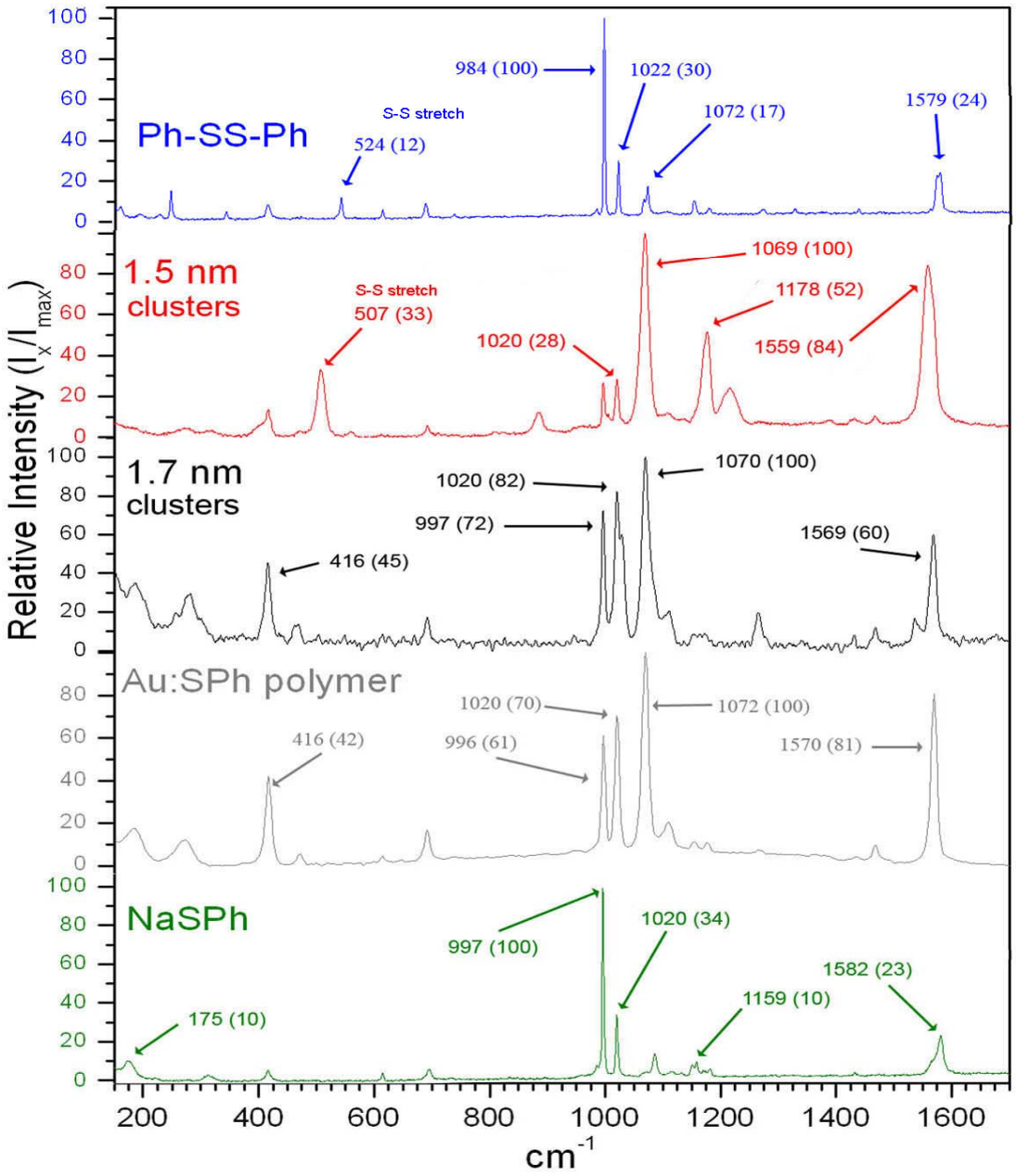


Figure 2.20 Raman spectra of $Au_x(SPh)_y$ MPCs with reference samples. Each spectrum is internally normalized with the most intense band in each set to 100 % intensity. The MPC spectra tended to have a small positive slope with increasing frequency, arising from broad luminescence with onset at ~1700 cm^{-1} extending beyond 3500 cm^{-1}.

Table 2.3 Tabulated Raman shifts for $Au_x(SPh)_y$ MPCs with benzenethiol (HSPh), sodium benzenethiolate (NaSPh), and diphenyldisulfide(PhSSPh) standards for comparison. Relative intensities are shown in brackets next to each frequency shift (in cm^{-1}). The most prominent features of each spectrum are in red text. Mode assignments are from references 36 and 45.

HSPh[36]	NaSPh	Ph-S-S-Ph	1.5 nm clusters	1.7 nm clusters	$(Au:SPh)_x$	mode
185	175 {10}	192 {4}	185 {33}	185 {18}	185 {18}	b_1
278	-	248 {14}	280 {5}	280 {29}	274 {12}	b_2
412	416 {5}	-	416 {14}	416 {45}	416 {42}	a_1
464	-	-	471 {3}	472 {5}	-	a_2
-	-	524	507 {33}	-	-	ν S-S
617	615 {4}	614 {6}	-	-	615 {4}	b_2
698	695 {6}	688 {9}	695 {6}	692 {17}	692{17}	a_1
999	997 {100}	984 {100}	996 {27}	997 {72}	996 {61}	a_1
1023	1020 {34}	1022 {30}	1020 {28}	1020 {82}	1020 {70}	a_1
1072	1072 {4}	1072 {17}	1069 {100}	1070 {100}	1072 {100}	b_2
1093	1086 {14}	-	1095 {11}	-	-	a_1
1108	1118 {5}	1106 {5}	1108 {12}	1111 {20}	1108 {21}	a_1
1159	1159 {10}	1153 {10}	-	-	1155 {11}	b_2
1182	1182 {6}	1187 {7}	1178 {52}	1173 {8}	1178 {11}	a_1
1272	-	1272 {6}	1216 {24}	1265 {20}	1267 {7}	b_2
1445	1432 {4}	1438 {6}	1432 {8}	1435 {4}	1438 {6}	b_2
1480	-	1467 {11}	1468 {13}	1468 {10}	-	a_1
1582	1582 {23}	1579 {24}	1559 {84}	1569 {60}	1570 {81}	b_2

These results do not quantify surfaced enhancement Raman effects, but it is significant that the 1070 cm^{-1} b_2 mode is 8 to 34x more intense than the 997 cm^{-1} a_1 mode within the MPCs *and* polymer relative to NaSPh, implying a metallic surface may not be needed for "selective" enhancement of certain vibrational modes. Raman shifts and relative intensities for the MPCs and standards are shown in Table 2.3, providing relative band intensity ratios for each substance, but absolute comparisons between spectra were not possible. The fundamental vibrational modes for benzenethiol are depicted graphically in Figure 2.21.

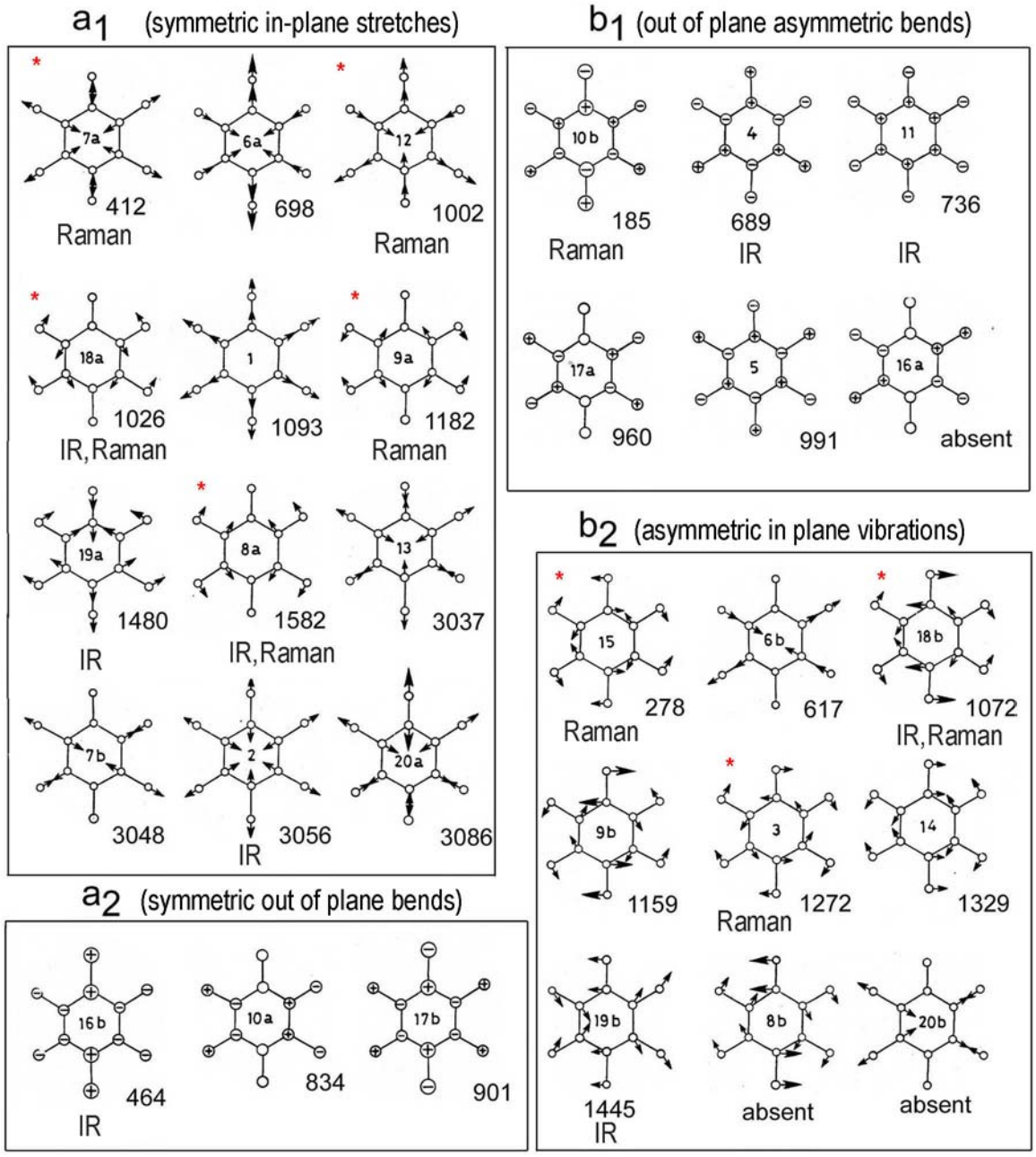


Figure 2.21 Graphical representations of benzenethiol vibrational modes adapted from reference 45. Infrared and/or Raman activity are indicated under each mode; unobserved modes are left unlabelled. The a_1 and a_2 vibrational modes preserve the C_{2v} symmetry axis of benzenethiol, while the b_1 and b_2 modes do not and are consequently less likely to be observed. The red asterisks (*) denote Raman modes with a relative intensity of $\geq$20 in the 1.5 or 1.7 nm $Au_x(SPh)_y$ MPC Raman spectra.

The preparation of standards and MPC samples for Raman spectroscopy is now detailed for completeness. The preparation of the $(Au:SPh)_x$ polymer[4] is as follows: A 3:1 molar ratio of benzenethiol (Aldrich) was combined with $HAuCl_4$ in methanol and stirred until a white precipitate results, in accordance with the stoichiometric reaction:

$$3\ PhSH + HAuCl_4 \rightarrow (Au^{I}SPh) + PhSSPh + 4HCl.$$

This solution was dried by rotary evaporation and rinsed with copious amounts of acetone to remove excess diphenyldisulfide, followed by drying to yield $[(Au:SPh)]_x$ as an insoluble white powder. Sodium benzenethiolate (NaSPh) and diphenyldisulfide (DPDS) were purchased from Aldrich and used without further purification.

The samples were prepared for Raman analysis by placing two to three milligrams of each dry, free-flowing material within a stainless steel target/sample holder and manual pressing into a pellet with a steel rod. Each sample was placed in a Bruker FRA 106/S FT Raman Module attached to a Bruker Equinox 55 FTIR spectrometer. The instrument has a fixed path length and focal length. The excitation for Raman scattering is at 1064 nm (9399 cm^{-1}, 1.165 eV) with a typical fluence of 75 mW. The laser focus area is ~ .80 mm^2. Spectra were typically collected at ~94 W/m^2 for 16 or 32 scans at 2 cm^{-1} resolution through the spectral range –600 – 3200 cm^{-1} in a duration of about two minutes. The notch filter inhibiting Rayleigh radiation detection occluded $\pm$ 150 cm^{-1}, precluding detection of Au-Au modes.

The spectra were reproducible over time and for different synthetic batches of the same material. Independent evaluation of the 1.7 nm clusters with a Thermo Nicolet NXR FT-Raman spectrometer at an excitation wavelength of 1064 nm with a null filter (0.3 mW, 640 scans) produced the same spectrum with a superior signal to noise ratio the

spectra presented herein.[46] Larger numbers of scans and higher fluences tended to degrade the samples into bulk gold, providing spectra devoid of benzenethiolate features. Anti-Stokes shifts were utilized to estimate sample temperatures and compared with thermogravimetric data for the materials, verifying sample stability during data collection.

The MPCs were irradiated at 1.165 eV (1064 nm), rather than the 1.65 – 2.41 eV (514 to 750 nm) previously utilized and the power per unit area of ~90±20 W/m^2 was near or below previously reported levels for aromatic thiols on bulk gold[38a-c], but sample degradation from thermal decomposition was initially a concern. Our inability to continuously rotate to refresh the samples during spectrum acquisition and minimize excess heating prompted the estimation of the sample temperatures from the ratios of the relative intensities of the Anti-Stokes and Stokes shifts. The relation

$$\frac{I_{AS}}{I_S} \cong e^{\frac{-h\Delta\nu}{kT}}$$

allows estimation of sample temperature, where I_{AS} and I_S are the relative intensities of the Anti-Stokes and Stokes peaks sharing the same shift, *h* is Planck's constant, $\Delta\nu$ is the frequency shift (in s^{-1}) of the Anti-Stokes/Stokes peak pair, *k* is the Boltzmann constant, and T is temperature. The estimated temperatures for the clusters are 394 K and 315 K for the 1.7 nm cores and 1.5nm cores, respectively. The thermal decomposition onset is at 421 K, indicating sample stability during spectrum collection. The Stokes/Anti-Stokes peaks and thermogravimetric data for the 1.7 nm cluster are shown in Figure 2.22. The MPCs absorb strongly in the near-infrared, possessing molar absorption coefficients (ε) at the 1.165 eV Rayleigh line on the order of 10^5 M^{-1} cm^{-1} (ε given in Figure 2.5**)**. This

suggests the Raman spectra collected may be in resonance. These Raman spectra are the first ever collected and reported on well-defined non-colloidal gold MPCs, as prior attempts with similar alkanethiols passivated MPCs were unsuccessful.[47]

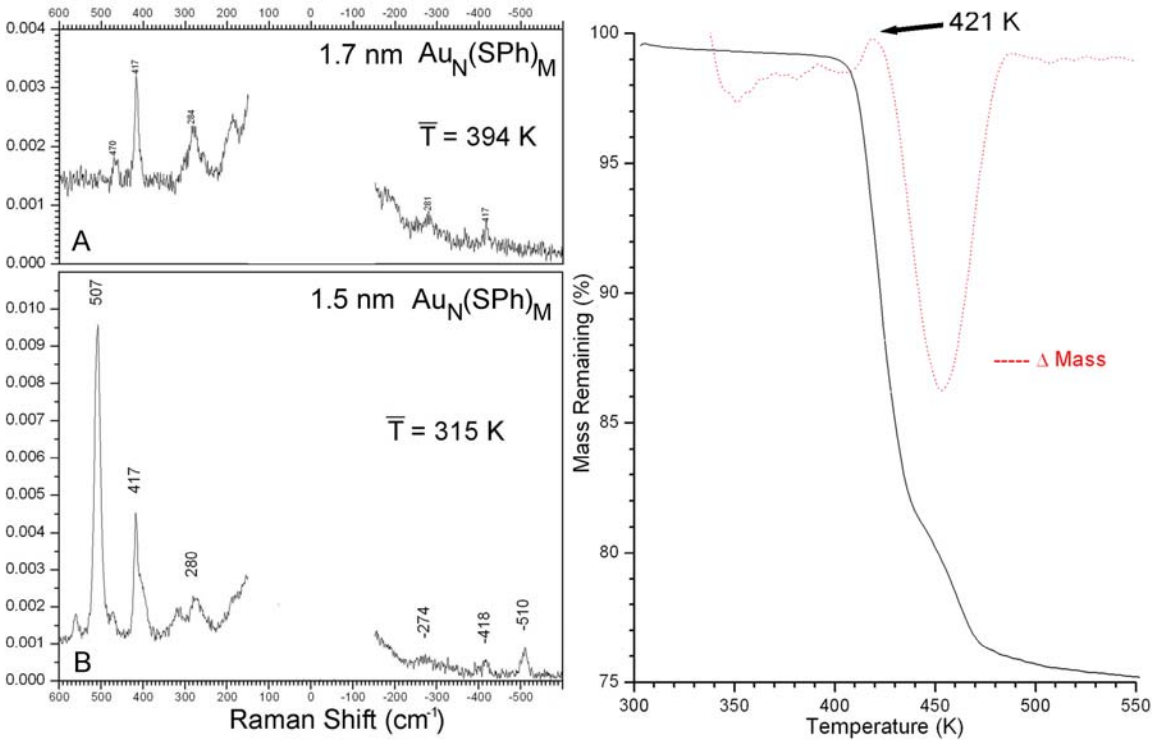


Figure 2.22 (A) Anti-stokes and stokes region of Raman spectrum for 1.7 nm $Au_x(SPh)_y$ (B) Anti-stokes and stokes region of Raman spectrum for 1.5 nm $Au_x(SPh)_y$ (C) Mass loss vs. temperature (black) and its derivative (red) to show the onset of significant mass loss for the 1.7 nm core $Au_x(SPh)_y$ MPCs. Thermogravimetric analysis was performed from 303 K to 873 K at a heating rate of 10 K/minute.

2.4 Summary

The thorough characterization detailed in this chapter for 1.5 and 1.7 nm $TOA_N[(Aux(SPh)y]^{N-}$ MPCs is necessary, as most research entailing "gold nanoparticles" is focused on colloidal materials possessing size polydispersity of hundreds to thousands of atoms. As such, the materials typically are not (or can not) be evaluated by mass spectroscopy, x-ray diffraction, ^{1}H-NMR, thermogravimetric analysis, elemental analysis, or even Raman spectroscopy. It is anticipated that this work provides examples of molecular materials with size dependent properties and specifically with optical properties that are a *direct* measure of the electronic states within a material. While the molecular formulas estimates of $TOA_{4-6}[Au_{110}(SPh)_{62}]$ and $TOA_{2-3}[Au_{140}(SPh)_{78}]$ do inherently contain a small degree of uncertainty, they are the best estimates possible with the correlated XRD, MS, ^{1}H-NMR, TGA, and EA data available. Application of these methods allowed the discovery that TOA^+ is present as a cation within the clusters. This new knowledge that the small gold MPCs can be anionic in nature, similar to known $[Pt_{44}(CO)_{47}]^{4-}$ and $[Pt_{38}(CO)_{44}]^{2-}$ clusters that are crystallographically characterized[48] has led to several subsequent discoveries, outlined in the next four chapters. Unfortunately, efforts to produce bulk crystals in our laboratory have been unsuccessful to date.

Chapter 2 References

(1) Guo, R.; Song, Y.; Wang, G.; Murray, R. *J. Am. Chem. Soc.* **2005**, *127*, 2752

(2) Guo, R.; Murray, R. *J. Am. Chem. Soc.* **2005**, *127*, 12140

(3) Brust, M.; Walker, M.; Bethell, D.; Schiffrin, D.; Whyman, R. *J. Chem. Soc., Chem. Comm.* **1994**, *7*, 801

(4) Puddephatt, R.; *The Chemistry of Gold*; Elsevier Scientific Publishing: Oxford, **1978**, 61

(5) Leff, D.; Ohara, P.; Heath, J.; Gelbart,W *J. Phys.Chem.* **1995**, *99*, 7036

(6) Schaaff, G.; Shafigullin, M.; Khoury, J.; Vezmar, I.; Whetten, R. *J. Phys. Chem. B.* **2001** *105*, 8785

(7) Chen, S.; Murray, R. *Langmui*r **1999**, *15*, 682

(8) (a) Johnson, S.; Evans, S.; Brydson, R. *Langmuir*, **1998**, *14*, 6639 (b) Chen, S. *Langmuir* **1999**, *15* 7551 (c) Evans, S.; Johnson, S.; Cheng, Y.; Shen, T. *J. Mater. Chem.* **2000**, *10*, 183 (d) Grate, J.; Nelson, D.; Skaggs, R. *Anal. Chem.* **2003**, *75*, 1868

(9) Zhang, H.; Evans, S.; Henderson, J.; Miles, R.; Shen, T. *J. Phys. Chem. B* **2003**, *107*, 6087

(10) Schaaff, G.; Price, R. *private communication* **2002**

(11) Donkers, R.; Lee, D.; Murray, R. *Langmuir*, **2004**, *20*, 1945

(12) Donkers, R.; Song, Y.; Murray, R. *Langmuir*, **2004**, *20*, 4703

(13) Schaaff, G.; Whetten, R. *J. Phys. Chem B* **2000**, *104*, 2630

(14) Schaaff, G.; Shafigullin, M; Khoury, J.; Vezmar, I.; Whetten, R.; Cullen, W.; First, P. *J. Phys. Chem. B* **1997**, *101*, 7885

(15) *CRC Handbook of Chemistry and Physics*; CRC Press, **2004**, 8-52

(16) Goodman, L.; Taft, R. *J. Am. Chem. Soc.* **1965**, *87*, 4385

(17) (a) Dance, I.; Fisher, K.; Banda, R.; Scudder, M *Inorg. Chem.* **1991**, *30*, 183
(b) Bensebaa, F.; Ellis, T.; Kruss, E.; Voicu,R.; Zhou,Y. *Langmuir* **1998**, *14*, 6579
(c) Woodruff, D.; Yu,M.; Bovet, N.; Satterly, C.; Lovelock, K.; Jones, R. *J. Phys. Chem. B.* **2006**, *110*, 2164

(18) Whelan, C.; Smyth, M.; Barnes, C. *Langmuir* **1999**, *15*, 116

(19) Hakkinen, H.; Walter, M.; Gronbeck, H. *J. Phys. Chem. B.* **2006**, *110*, 9927

(20) Cleveland, C.; Landman, U.; Shafigullin, M.;Stephens, P.; Whetten, R. *Z. Phys. D.* **1997**, *40*, 503

(21) Cleveland, C.; Landman, U.; Schaaff, T.; Shafigullin, M.;Stephens, P.; Whetten, R. *Phys. Rev. Lett.* **1997**, *79*, 1873

(22) Whetten, R.; Shafigullin, M.; Khoury, J.; Schaaff, T.; Vezmar, I.; Alvarez, M.; Wilkinson, A. *Acc. Chem. Res.* **1999**, *32*, 397

(23) Shafigullin, M *Ph.D. Thesis Dissertation* **1999**, Georgia Institute of Technology

(24) Sabatani, E.; Cohen-Boulakia, J.; Bruening, M.; Rubinstein, I. *Langmuir* **1993**,*9*, 2974

(25) Tao,Y.; Wu, C.; Eu, J.; Lin, W. *Langmuir* **1997**, *13*, 4018

(26) Shao, Jianfei *Ph. D. Thesis Dissertation* **2006**, Georgia Institute of Technology

(27) Schaaff, T.; Shafigullin, M.; Khoury, J.; Vezmar, I.; Whetten, R.; Cullen, W.; First, P.; Gutierrez-Wing, C.; Ascensio, J.; Jose-Yacaman, M. *J. Phys. Chem. B.* **1997**, *101*, 7885

(28) Gutierrez, E; Powell, R.; Furuya, F.; Hainfelf, J.; Schaaff, T.; Shafigullin, M.; Stephens, P.; Whetten, R. *Eur. Phys. J. D.*, **1999**, *9*, 647

(29) Schaaff, T. *Analytical Chemistry*, **2004**, *76*, 6187

(30) Hosteetler, M; Wingate, J.; Zhong, C.; Harris, J.; Vachet, R.; Clark, M.; Londono, D.; Green, S.; Stokes, J.; Wignall, G.; Glish, G.; Porter, M.; Evans, N.; Murray, R. *Langmuir* **1998**, *14*, 17

(31) Schaaff, T.; Knight, G.; Shafigullin, M.; Borkman, R.; Whetten, R. *J. Phys. Chem. B.* **1998**, *102*, 10643

(32) Kohlmann, O.; Steinmetz, W.;Mao, X.; Wuelfing, P; Templeton, A.; Murray, R.; Johnson, C. *J. Phys. Chem. B.* **2001**, *105*, 8801

(33) Hostetler, M.; Stokes, J.; Murray,R. *Langmuir* **1999**, *12*, 3604

(34) Nuzzo, R.; Fusco, F.; Allara, D. *J. Am. Chem. Soc.* **1987**, *109*, 2358

(35) Chen, S.; Murray, R. *Langmuir* **1999**, *15*, 682

(36) Wan, L.; Terashima, M.; Noda, H.; Osawa, M. *J. Phys. Chem. B.* **2000**, *104*, 3563

(37) Szafranski, C.; Tanner, W.; Laibinis, P.; Garrell, R. *Langmuir* **1998**, *14*, 3570

(38) (a) Ulman, A. *Chem. Rev.* **1996**, 96, 1533 (b) Link,S.; El-Sayed, M. *Int. Rev. in Phys. Chem.* **2000**, *19(3)*, 409 (c) Kudelski, A. *Vib. Spectros.* **2005**, *39(2)*, 200

(39) (a) Carron, K.; Hurley, G. *J. Phys. Chem.* **1991**, *95*, 9979 (b) Garrell, R.; Chadwick, J.; Severance, D.; McDonald, N.; Myles, D. *J. Am. Chem. Soc.* **1995**, *117*, 11563 (c) Szafranski, C.; Tanner, W.; Laibinis, P.; Garrell, R. *Langmuir* **1998**, *14*, 3570

(40) Sawaguchi, T.; Mizutani, F.; Yoshimoto, S.; Taniguchi, I. *Electochim. Acta* **2000**, *45*, 2861

(41) (a) Dhirani, A.; Zehner, R.; Hsung, R.; Guyot-Sionnest, P.; Sita, L. *J. Am. Chem. Soc.* **1996**, *118*, 3319 (b) Tao, Y.; Wu, C.; Eu, J.; Lin, W. *Langmuir*, **1997**, *13*, 4018

(42) (a) Whelan, C.; Smyth, M.; Barnes, C. *Langmuir* **1999**, *15*, 116 (b) Molina, L. M.; Hammer, B. *Chem. Phys. Lett.* **2002**, 360(3,4), 264 (c) Danisman, Mehmet F.; Casalis, Loredana; Bracco, Gianangelo; Scoles, G. *J. Phys.Chem. B* **2002**, *106(45*), 11771 (d) Nara, Jun; Higai, Shin'ichi; Morikawa, Yoshitada; Ohno, Takahisa. *J. Chem. Phys.* **2004**, *120(14)*, 6705 (e) Roper, M. G.; Skegg, M. P.; Fisher, C. J.; Lee, J. J.; Dhanak, V. R.; Woodruff, D. P.; Jones, Robert G. *Chem. Phys. Lett.* **2004**, *389(1-3)*, 87 (f) Yu, Miao; Driver, S. M.; Woodruff, D. P. *Langmuir* **2005**, *21(16)*, 7285 (g) Woodruff, D.; Yu, M.; Bovet, N.; Satterley, C.; Lovelock, K.; Jones, R.; Dhanak, V. *J. Phys. Chem. B* **2006**, *110*, 2164

(43) (a) Gui, J.; Stern, D.; Lu, F.; Zapien, D.; Hubbard, A. *Langmuir* **1991**, *7*, 955 (b) Uehara, J.; Aramaki, K. *J. Electrocem. Soc.* **1991**, *138*, 3245

(44) (a) Degen, I.; Rowlands, A. *Spectrochim. Acta* **1991**, *9/10*, 1263 (b) Boyen, H.; Kastle, G.; Wegil, F.; Ziemann, P.; Schmid, G.; Garnier, M.; Oelhafen, P. *Phys. Rev. Lett.*, **2001**, *87(27)*, 6401

(45) Varsanyi, G. *Assignments for Vibrational Spectra of Seven Hundred Benzene Derivatives*; John Wiley and Sons: New York, 1974

(46) M. Foote; T. Hanks, *private communication* **2005**

(47) Whetten R, Price, R. ~Au_{140}(S-hexyl)$_{56}$ clusters did not yield Raman spectra of the surface-bound thiolates in our hands nor have they been reported by anyone *unpublished results (no one ever reports failure in the literature)*

(48) Roth J., Lewis G., Safford L., Jiang X., Dahl L., Weaver M. *J. Am. Chem. Soc.* **1992,** *114*, 6159

CHAPTER 3

1.1 NANOMETER CORE $TOA_2[Au_{44}(SPh)_{28}]$ QUANTUM DOTS

3.1 Size Reduction of 1.5 and 1.7 nm $Au_x(SPh)_y$ MPCs to 1.1 nm Core Diameter.

During the initial year spent characterizing $Au_x(SPh)_y$ MPCs, the presence of tetraoctylammonium (TOA^+) was consistently evidenced by ^{1}H-NMR and FTIR spectroscopy (detailed in Chapter 2), regardless of any purification steps undertaken. As the previous paradigm was that "residual" TOA containing species within the MPC products could be removed, purification of the 1.5 nm ~$Au_{110}(SPh)_{62}$ MPCs was attempted by exposure to a 10 - 20 benzenethiol molar excess (relative to the bound benzenethiolates) in methylene chloride for 72 hours. This process is commonly known as annealing or etching.[1,2] Reports of efficient surface thiolate exchange reactions in methylene chloride by Murray et al.[3] provided the rationale for using this solvent and reaction duration. It was presumed a significant (10-20x) molar excess of free thiol relative to cluster-bound thiolates would prevent MPC degradation and displace any "excess" TOA. This treatment of the MPCs yielded unforeseen products initially evidenced by additional structure in the optical spectra of the purified products and a white, insoluble by-product strongly resembling $[Au:SPh]_x$ polymer. Reacting the MPCs with excess benzenethiol in dichloromethane did not consistently yield smaller clusters, hinting at an overlooked reactant and the possible need to change to a less reactive solvent.

A report by Murray and Song[4] indicated tetrahydrofuran (THF) could be effectively substituted in place of dichloromethane for gold MPC exchange reactions. They also found THF under anaerobic conditions retarded exchange reactions on $Au_x(hexanethiolate)_y$ MPCs with a 2:3 ratio of incoming to outgoing ligands. When the

exchange reaction was performed under air instead of N_2, nearly four times more 6-mercpatohexanethiolate ligands exchanged onto these “as-prepared” negatively charged 1.7 nm cores. This work also indicated clusters electrochemically oxidized from their “as formed” negative charge state could undergo a slightly higher number of ligand exchanges.

This information guided us to adapt pure THF as the solvent for etching the 1.5 nm $Au_x(SPh)_y$ MPCs at 10 μM in the presence of a 10 - 20x ratio of incoming benzenethiol to benzenethiolates on the MPCs. Aqueous hydrogen peroxide (30 %v/v) was included as an oxidant at a 10:1 ratio relative to both Au and free benzenethiol, and 17:1 relative to the thiolates comprising the MPCs. The inclusion of H_2O_2 at this concentration leads to conversion of the 1.5 nm core MPCs to 1.1 nm core diameter in two to three hours at room temperature with an insoluble white byproduct presumed to be $(Au^{(I)}SPh)_x$ and/or DPDS also generated. This process requires *six days* under air in the absence of H_2O_2. This same stoichiometry does not reduce the core size of 1.7 nm $Au_x(SPh)_y$ MPCs. Instead, twice as many equivalents of H_2O_2 are required form 1.1 nm core MPCs from these larger core clusters. The most likely explanation for this is lower average oxidation state of the 1.7 nm MPCs (+2 to 3) compared to the 1.5 nm MPCs (+4 to 6). Details of charge state determination for the MPCs are given in Chapter 2. The 1.1 nm core MPC has the nominal composition $TOA_2[Au_{44}(SPh)_{28}]$. A detailed description of the conditions used to generate these 1.1 nm core $Au_{44}(SPh)_{28}$ MPCs from 1.5 nm $Au_x(SPh)_y$ MPCs follows.

In pure tetrahydrofuran (15 mL) are dispersed 1.5 nm core clusters (31.9 mg, ~118 μmol Au) with continuous stirring. Benzenethiol (12 μL, 118 μmol) and 30 % aqueous hydrogen peroxide (120μL, 1.18 mmol) are added. The reaction completes within three hours, indicated by a complete color change from dark brown to pale olive and is further verified by optical spectroscopy. The solution is dried by rotary evaporation

and the MPCs are transferred to a .16 μm syringeless filter with acetonitrile and rinsed thrice with acetonitrile (50 mL) to remove by-products. Acetone (80 mL) is injected through the syringeless filter to remove any residual diphenyldisulfide. The solids are then eluted with toluene (50 mL), yielding 12.0 mg of 1.1 nm MPCs. They are soluble at 400 μM in dichloromethane and 700 μM in toluene. The product yield with respect to gold is 34 %. Further study and optimization of this reaction may improve the yield.

The conversion of 1.7 nm $Au_x(SPh)_y$ MPCs to 1.1 nm core $Au_{44}(SPh)_{28}$ MPCs is achieved similarly to the previously outlined method. In pure tetrahydrofuran (50 mL) are dispersed 1.7 nm core clusters (20.7 mg, ~77 μmol Au) with continuous stirring. Benzenethiol (77 μL, 747 μmol) and 30 % aqueous hydrogen peroxide (154 μL, 1.5 mmol) are added. The reaction completes within three hours, indicated by a complete color change from dark brown to pale olive, further verified by optical spectroscopy. The solution is dried by rotary evaporation and the MPCs are transferred to a .16 μm syringeless filter with acetonitrile and rinsed thrice with acetonitrile (50 mL) to remove by-products. Acetone (80 mL) is injected through the syringeless filter to remove any residual DPDS. Methylene chloride (10 mL) elution of the filter obtains 13.6 mg of 1.1 nm MPCs. The yield of gold in the isolated product is 61 %.

3.2 Physical Properties of $TOA_2[Au_{44}(SPh)_{28}]$ Quantum Dots

3.2.1 Optical Properties

Before any insight was gained into the composition of the $TOA_2[Au_{44}(SPh)_{28}]$ MPCs, their olive green coloration hinted they might be similar to the commercially available Nanogold®, which has nominal composition $Au_{73\text{-}75}(PR_3)_{15\text{-}17}Cl_x$.[5] Unlike Nanogold®, the etched $Au_x(SPh)_y$ MPCs lack sp-sp intraband transitions below 1.7 eV and most closely resemble the much smaller Au_{18}(glutathionate)$_{14}$ cluster or the $Au_{11}(PPH_3)Cl_3$ undecagold compound.[6,7] The $Au_{44}(SPh)_{28}$ MPCs are compared to $Au_{110}(SPh)_{62}$ and several well-defined smaller clusters in Figure 3.1. These spectra clearly show the $Au_{44}(SPh)_{28}$ gold core possesses a far simpler electronic spectrum than similarly sized Au_{75}(S-hexyl)y or ~Au_{38}(S-hexyl)$_{24}$ MPCs. The well-defined optical absorbance onset (bandgap) at 1.6 eV and absence of sp-sp intraband transitions below 1.7 eV are unique, given that even Au_{25}(glutathionate)$_{18}$ MPCs possess weak sp-sp intraband transitions with absorbance onset at 1.3 eV .

There are two plausible explanations for a large bandgap and lack of intraband transitions. The first and simplest explanation is metal to ligand charge transfer (MLCT) from the gold sp molecular orbital(s) to benzenethiolate. Oxidation of surface gold atoms by hydrogen peroxide during etching might contribute to increased polarity between the surface gold atoms and benzenethiolate. Such an effect would impart larger ionic character on the gold-thiolate bonds, giving greater stability. Unlike the larger 1.5 and 1.7 nm $Au_x(SPh)_y$ MPCs, these smaller clusters do not readily degrade in dichloromethane within a week. Another explanation for an unusually high bandgap is a high symmetry structure, such as tetrahedral (T_d) or octahedral (O_h). A known high symmetry tetrahedral

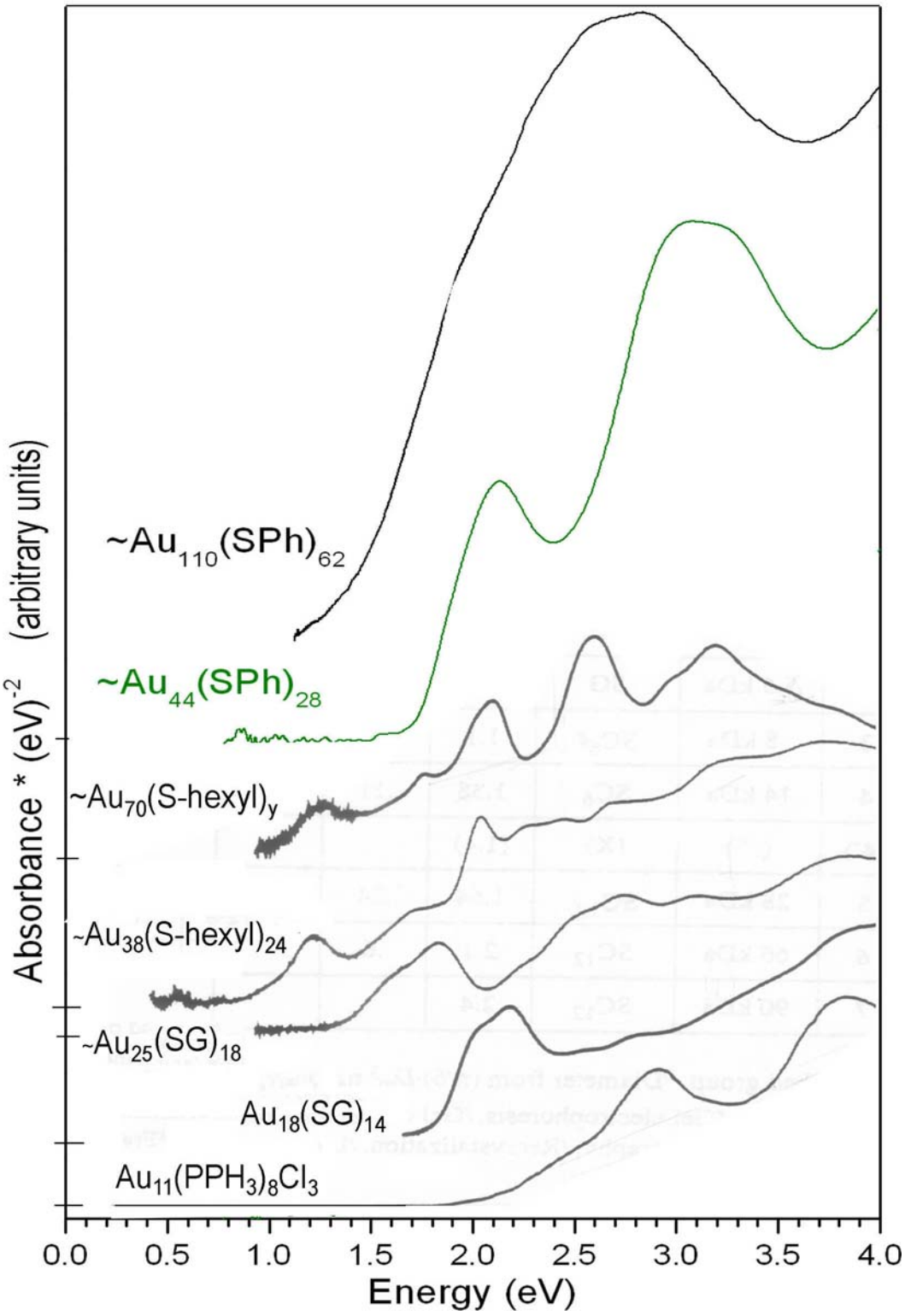


Figure 3.1 Optical spectra of $Au_{44}(SPh)_{28}$ clusters (green) shown with its precursor before etching (top) and similarly sized clusters (below). The Au_{25} and Au_{18} MPCs are passivated by glutathionate (SG). Tick marks on the Y-axis indicate the zero absorbance value for each spectrum. Spectra for smaller clusters were adapted from reference 8.

(T_d) Au_{20} cluster generated in the gas phase has a 1.6 eV bandgap, while icosahedral (I_h) C_{60} possesses a 1.57 eV bandgap.[9,10] Unfortunately, the precise structure of this interesting molecule is currently unknown, as crystallization efforts have been unsuccessful. One interesting possibility that could explain the similarity of this cluster and the Au_{20} cluster[9] is that $[Au_{44}(SPh)_{28}]^{2-}$ is actually a truncated tetrahedral $[Au_{16}]^{2-}$ core, surrounded by 28 $(AuSPh)^0$, with one (AuSPh) at each truncated vertex , two per edge, and three on each tetrahedral face. Theoretical models of this quantum dot are currently being evaluated.[11]

The characteristic olive color of the $TOA_2[Au_{44}(SPh)_{28}]$ quantum dot is due to an absorption minima at 2.4 eV (517 nm) between its two broad absorption features centered at 2.1 eV (590 nm) and 3.1 eV (400 nm). This is graphically illustrated and contrasted with the optical spectrum of the $TOA_{4\text{-}6}[Au_{110}(SPh)_{62}]$ precursor in Figure 3.2. The estimated energy dependent molar absorptivity coefficients of $Au_{44}(SPh)_{28}$ are plotted in Figure 3.3, but they are only initial estimates, as only at most 20 mg of this material have been available at a time. Accurate molar absorptivity coefficient estimation is further complicated by quantum dot solutions above 100 μM in concentration absorbing so strongly that their coloration is nearly black and they do not obey Beer's law. The derivative of the optical spectrum reveals the full richness of the electronics states, shown in Figure 3.4. The derivative plot of absorbance as a function of energy reveals the room temperature density of states, which are numerically listed in Table 3.1. The data clearly shows the metallic core possesses accessible, discrete electronic states separated in energy by at least 470 meV, a quantity which is 18 times greater than the 26 meV

ambient thermal energy (k_BT). This definitively shows the materials are quantum dots, rather than colloids.

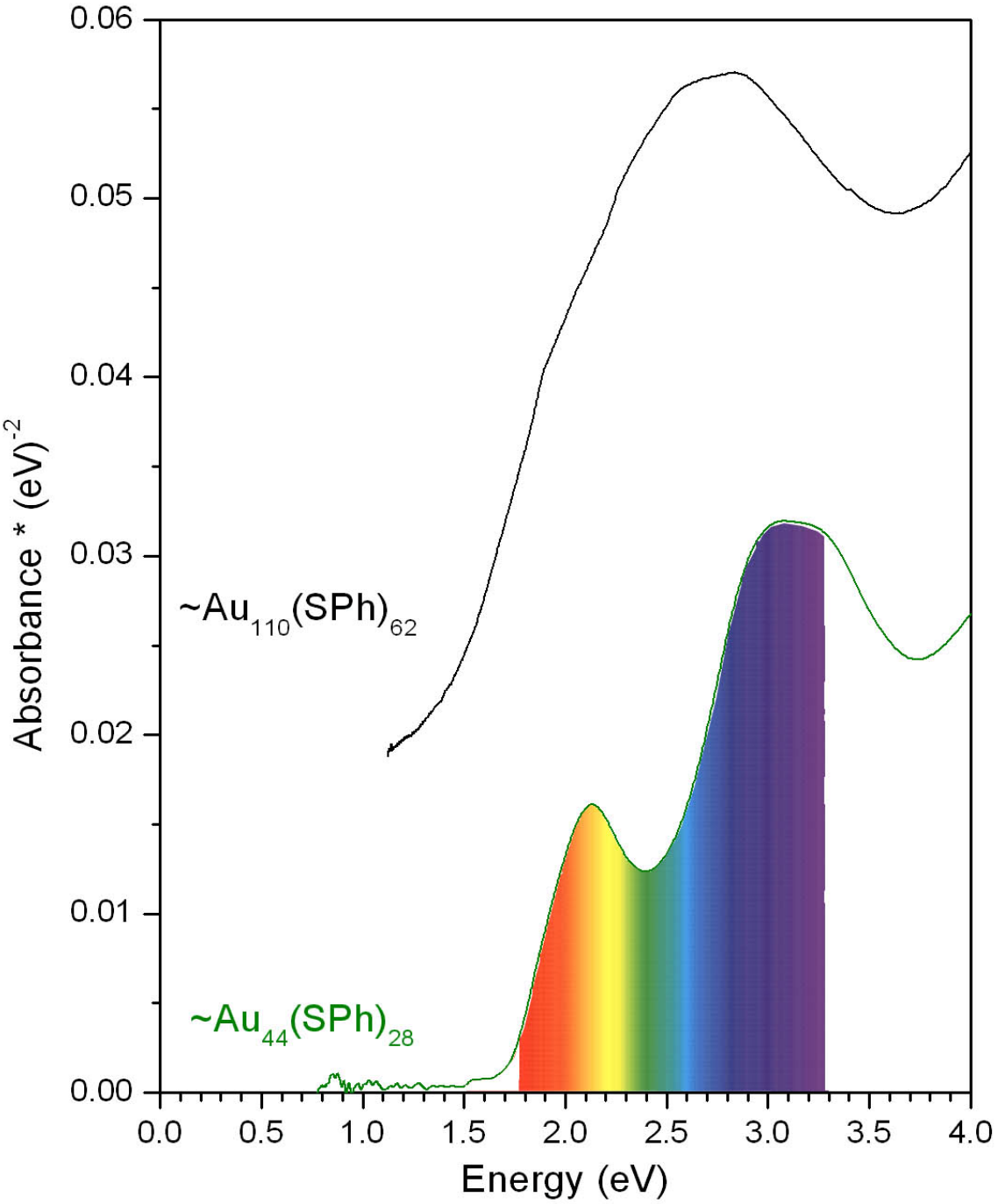


Figure 3.2 Optical spectra of Au_{44} quantum dots and their reaction precursor, ~$TOA_6[Au_{110}(SPh)_{62}]$. The spectra were collected in-sutu for the etching reaction. Only 2.4 eV (green) light is not strongly absorbed by the QDs, thus green light is selectively transmitted through cluster solutions with all other visible colors strongly absorbed.

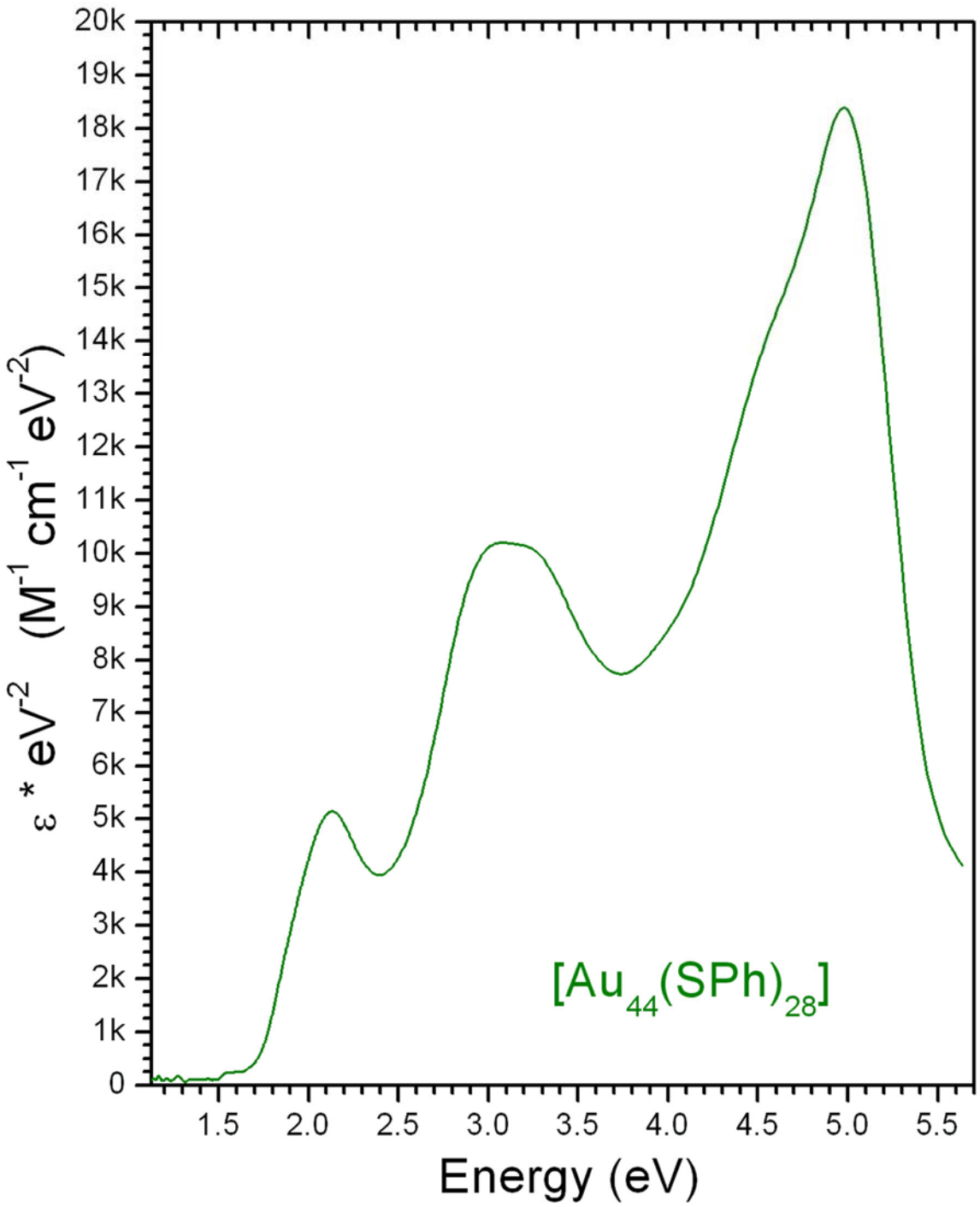


Figure 3.3 Molar absorptivity coefficient (ε) plot as a function of photon energy for a 3.15 μM solution of $TOA_2[Au_{44}(SPh)_{28}]$ in tetrahydrofuran (solvent cutoff = 5.63 eV). Concentrations above 100 μM do not yield useful ε plots.

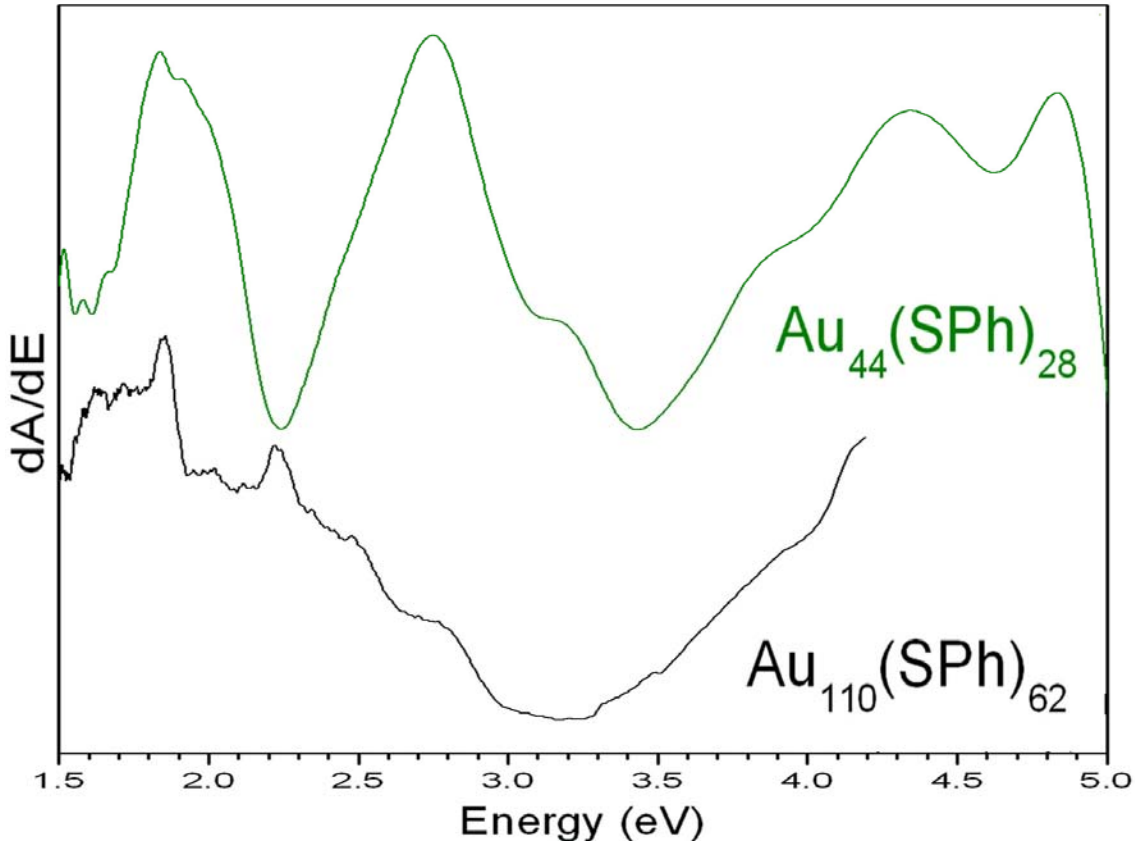


Figure 3.4 Derivative plot of optical spectra for 1.1 (Au_{44}) and 1.5 nm (Au_{110}) $Au_x(SPh)_y$ MPCs. The smaller cluster possesses more well-defined transitions from 1.5 to 4.2 eV than the 1.5nm precursor. This is evidenced by its *five* minima which include the two onsets for the peak "shoulders" at 3.1 and 3.9 eV.

Table 3.1 Dominant bands from the derivative electronic spectra (Figure 3.4) of $TOA_2Au_{44}(SPh)_{28}$. Band edge onsets, absorbance maxima, and energy difference between maxima are shown. The energy differences between adjacent electronic states are clearly an order of magnitude in excess of the .026 eV room temperature value for k_BT. Further electrochemical and/or STM characterization at cryogenic temperatures would undoubtedly reveal an even more structured density of states. LMCT denotes ligand to metal charge transfer. The absorption maxima for the π to π* transition of pure benzenethiol was measured at 5.17 eV.

Possible Band Assignments	Band Onset (eV)	Band Maxima (eV)	Energy to next highest state (eV)
Filled 1D shell → open 1F shell	1.61	1.84	1.61
Au 5d → Au 6sp	2.24	2.75	0.91
Au 5d → Au 6sp	3.08	3.20	0.45
S 3p → Au 6sp (LMCT)	3.43	4.35	1.15
aromatic π → π*	4.63	4.82	0.47

3.2.2 Powder X-Ray Diffraction

3.2.2.1 Large Angle Diffraction (LAXRD)

Powder X-ray diffraction in the large angle region ($2\theta = 10^{o} - 140^{o}$, s = 1.1 – 12.0) for $Au_{44}(SPh)_{28}$ yields data that matches well with the hypothetical diameter approximated using a spherical geometry and the bulk density of gold (59 atoms/nm^3). A spherical geometry combined with the bulk density of gold yields the relation:

$$D = \left(\frac{N_{Au}}{31}\right)^{\frac{1}{3}}$$

where **D** is the cluster diameter in nanometers and $\mathbf{N_{Au}}$ is the number of gold atoms in the cluster. Applying this relation to an Au_{44} cluster predicts a 1.1 nm diameter. The LAXRD data presented in Figure 3.5 indicates a 1.11 ± .09 nm diameter.

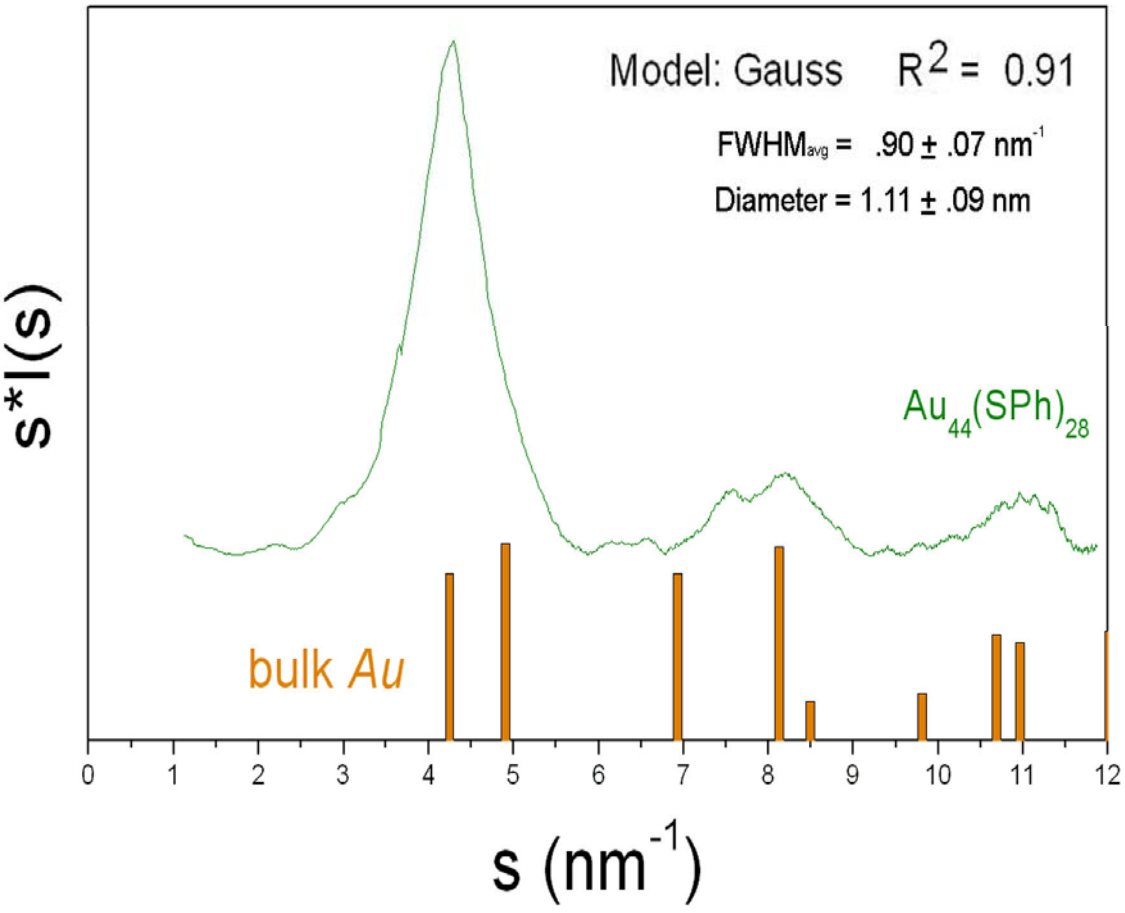


Figure 3.5 LAXRD for $TOA_2[Au_{44}(SPh)_{28}]$. The peaks were evaluated with Gaussian fits as described in the previous chapter or the larger $Au_x(SPh)_y$ MPCs. The average FWHM and average diameter are shown on the figure. The anticipated peak heights for bulk gold are provided to demonstrate the extreme difference between bulk and size-quantized gold.

3.2.2.2 Small Angle Diffraction (SAXRD)

Powder diffraction in the low angle region reveals poor mid range ordering in the $TOA_2[Au_{44}(SPh)_{28}]$ MPCs, on the same scale as the larger 1.5 nm $Au_x(SPh)_y$ MPCs. The presence of the disordered cation TOA^+ appears to limit the distance between adjacent cores and prevent long range ordering that might lead to macroscopic crystal formation as discussed in the previous chapter. The core-core distance between clusters is estimated at 1.69 nm from the reciprocal of the small angle diffraction peak. Subtracting the 1.11 $\pm$ .09 nm core diameter gives an estimated edge-edge distance of .58 $\pm$ .09 nm, a value very near the .63 nm estimated for the 1.5 nm $Au_x(SPh)_y$ MPCs. The small angle diffraction plot is shown in Figure 3.6.

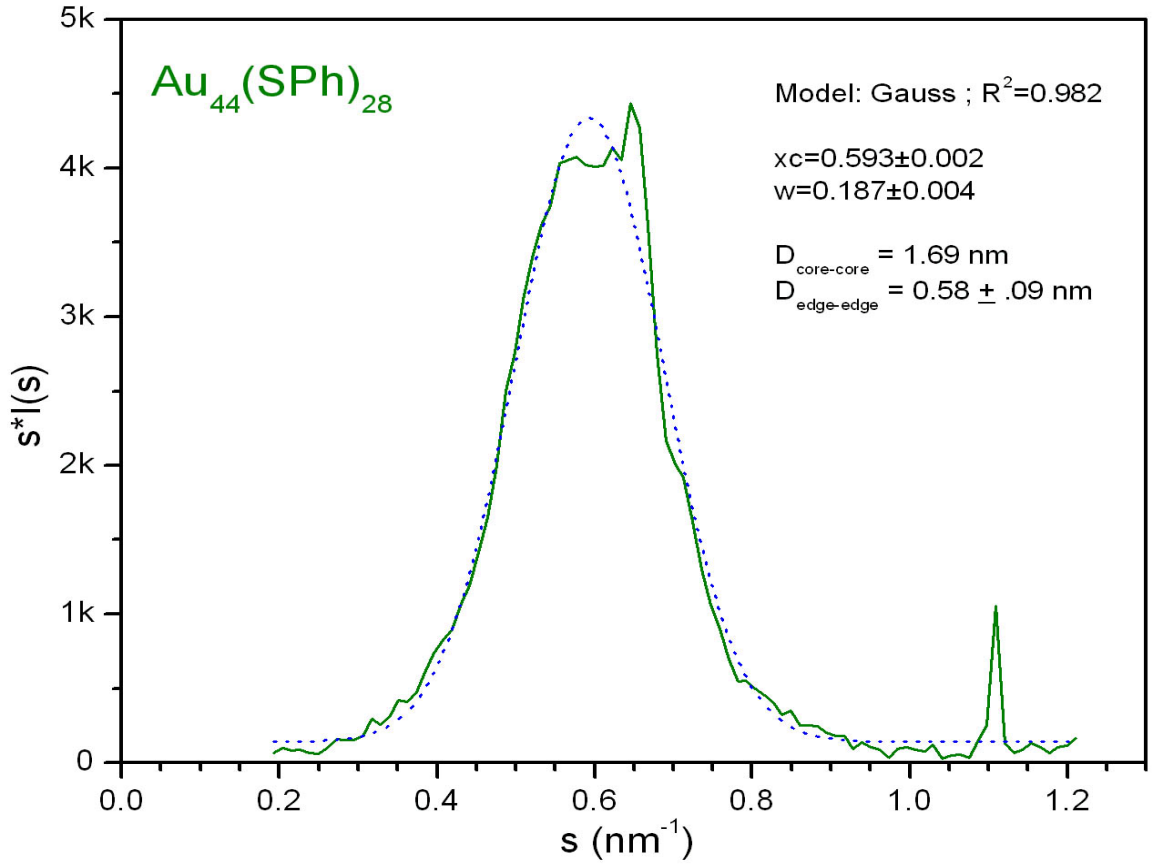


Figure 3.6 SAXRD for $TOA_2[Au_{44}(SPh)_{28}]$. The edge-edge distance between adjacent clusters is calculated to be .58 ± .09 nm. The Gaussian peak fit is shown in blue.

3.2.3 MALDI Mass Spectrometry of $TOA_2[Au_{44}(SPh)_{28}]$

After optical and diffraction data were obtained for these interesting clusters, mass spectral data was collected by the methods outlined in Chapter 2. The full mass spectrum (Figure 3.7) obtained showed the clusters to be pure, as a dimer anion peak was resolved at nearly twice the mass of the dominant molecular fragmentation pattern for the clusters. The complex fragmentation pattern from 7 kDa to 13 kDa immediately indicated that molecules were present. The molecular fragmentation pattern for this cluster from 7 kDa to 13 kDa is shown in Figure 3.8. The fragmentation is dominated by a series

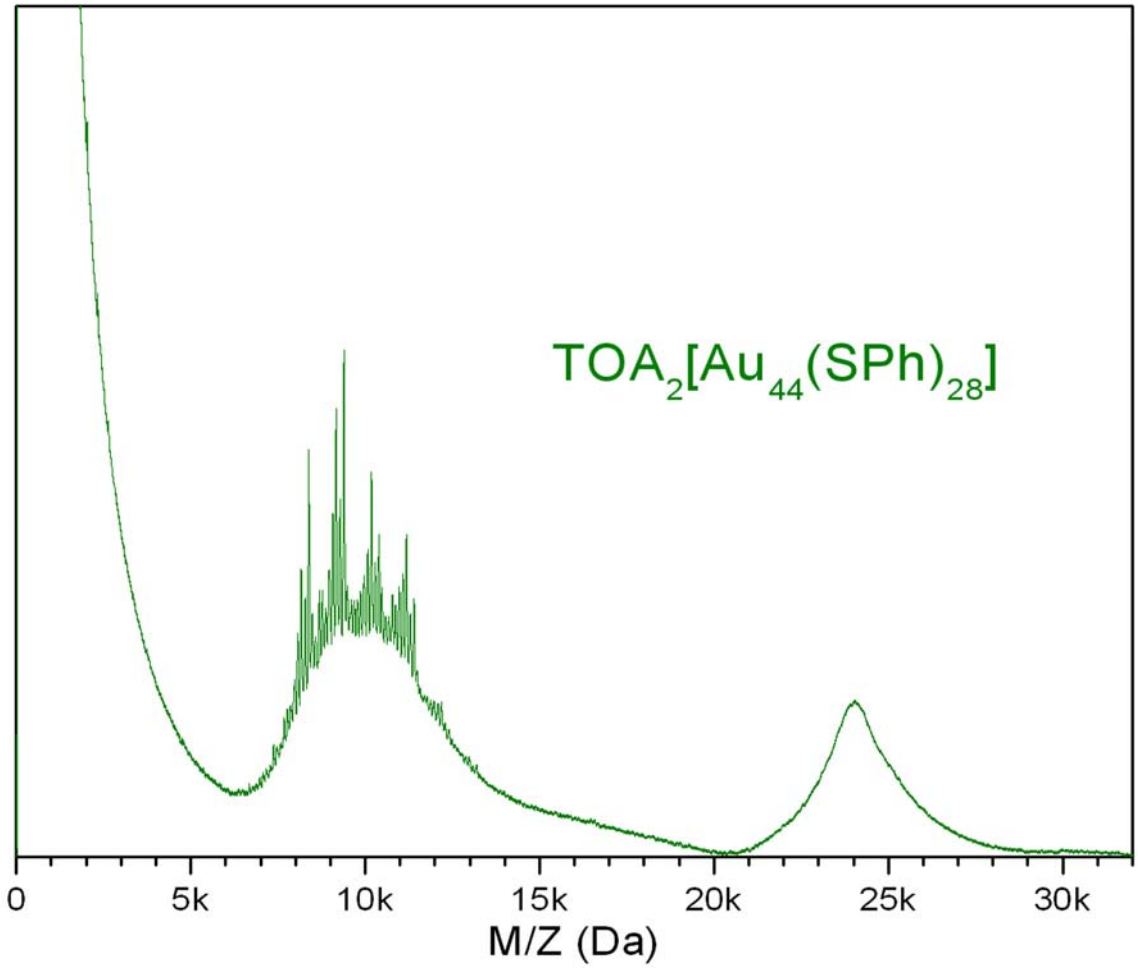


Figure 3.7 MALDI-MS for $TOA_2[Au_{44}(SPh)_{28}]^{2-}$. The x-axis shows the full range initially evaluated. Data below 5 kDa is noise, while the peak at 24 kDa is the gas phase dimer anion of the molecule.

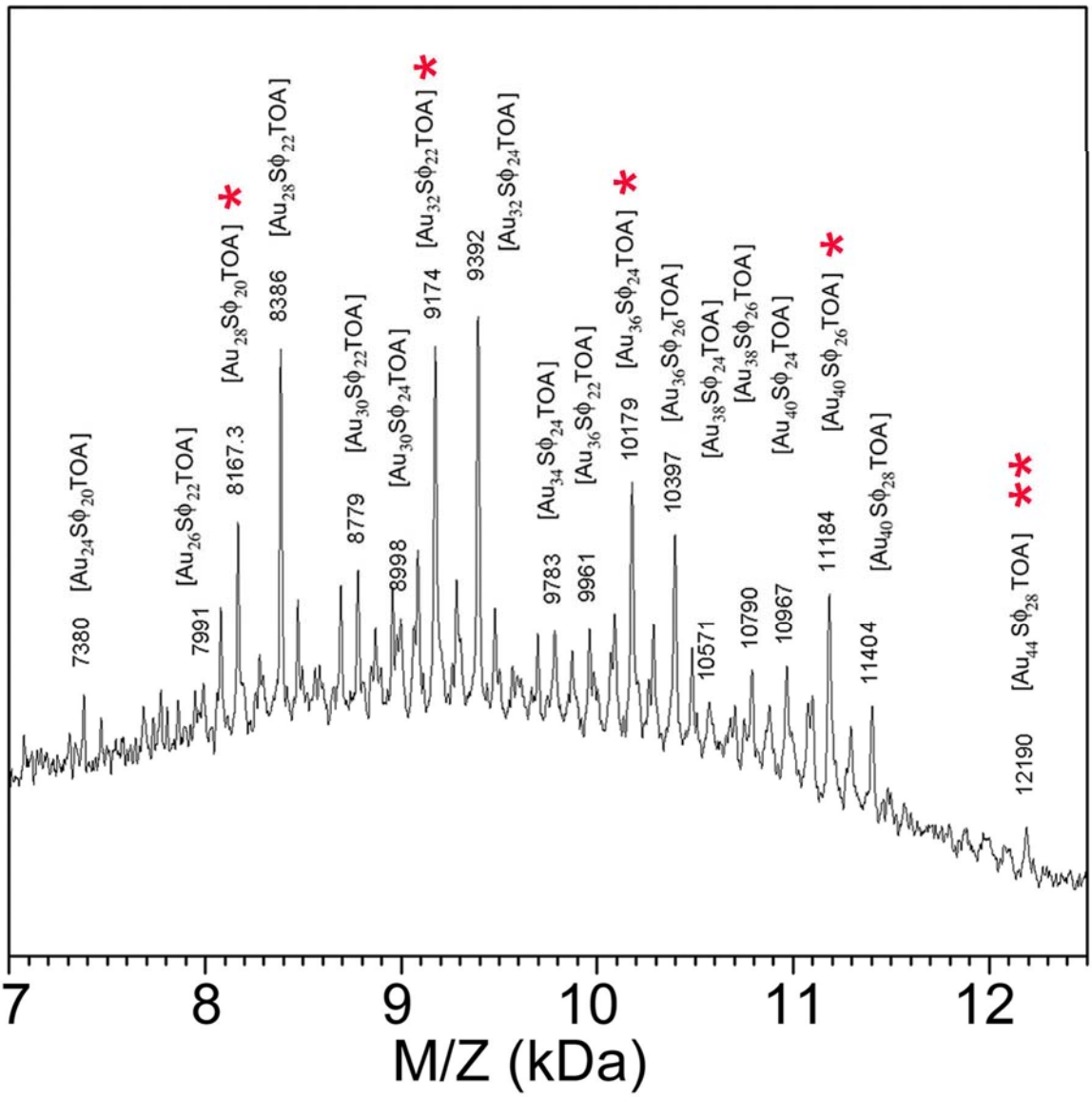


Figure 3.8 Fragmentation pattern (anions) for $(TOA)_2[Au_{44}(SPh)_{28}]$**.** An asterisk indicates masses separated by ~1006 Da with two asterisks denoting the parent peak.

of peaks separated by 1006 $\pm$ 2 Da at 12190, 11184, 10178, 9174, and 8176. This 1006 Da mass loss represents $(Au_4(SPh)_2)$, lost in three steps as two Au_2 fragments and one $(PhS)_2$ fragment. Additional peaks between these major fragmentations show loss of Au_4 and $Au_2(SPh)_2$ fragments occurring as well. The highest mass peak is the parent ion at 12190, corresponding to $TOA[Au_{44}(SPh)_{28}]^-$, and the neutral compound is presumed to

have an additional TOA^+ to preserve charge balance, similar to the larger clusters detailed in the previous chapter. This gives the molecular formula $TOA_2[Au_{44}(SPh)_{28}]$ for these quantum dots.

The *intact* C-S bonds in this mass spectrum is exceptional with regard to both alkanethiolate clusters previously characterized by mass spectrometry (described in Chapter 1) and the $Au_x(SPh)_y$ MPCs (Chapter 2). A major factor contributing to this initially surprising behavior is that these clusters likely absorb at least four times less energy than their larger counterparts. Their ε (molar absorptivity) is ~ 580 at the laser desorption energy of 3.67 eV, while the 1.5 and 1.7 nm $Au_x(SPh)_y$ clusters have ε of ~2300 and ~4600, respectively. Additionally, if the 'surface' interactions between gold and sulfur are greater (more polar) in these smaller clusters due to transfer of s electrons from gold to the sulfur atoms, the C-S bond of benzenethiol could be polarized and atypically stronger. While the precise reason may remain unknown for the C-S bond remaining intact in this cluster, this boon provided a nearly absolute determination of the molecular formula of the clusters. The spectra have been reproduced on-campus by the Georgia Institute of Technology mass spectrometry facilities, as well as at Vanderbilt University by Dr. Ken Shriver.

3.2.4 Nuclear Magnetic Spectroscopy

Integration of the ^{1}H-NMR spectrum of these quantum dots reveals a 15:1 ratio of benzenethiolate to TOA^{+}, closely agreeing with the 14:1 ratio determined from mass spectrometry. A fully integrated spectrum for $TOA_2[Au_{44}(SPh)_{28}]$ is provided in Figure 3.9.

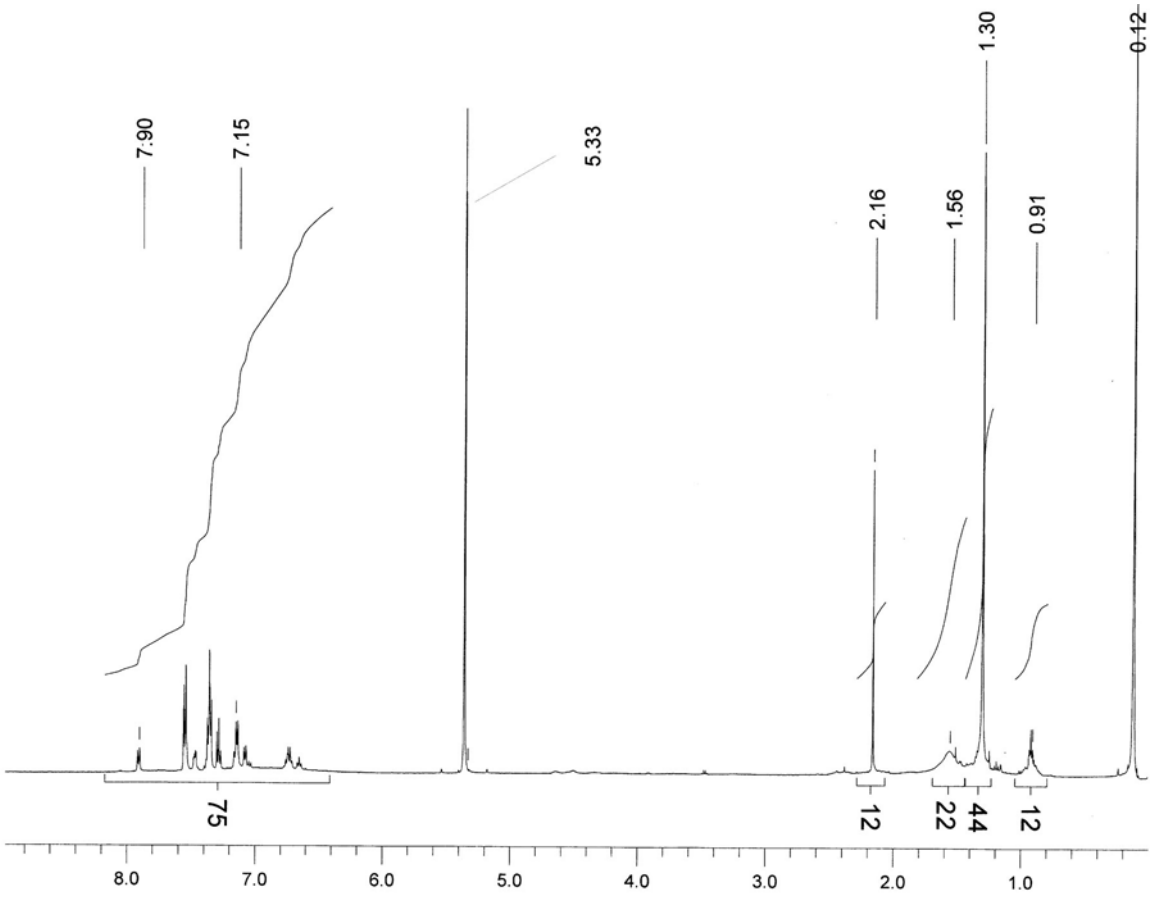


Figure 3.9 Integrated ^{1}H-NMR spectrum of $TOA_2[Au_{44}(SPh)_{28}]$. The methyl resonances at 0.91 ppm are scaled to represent the 12 hydrogen atoms of a TOA cation, giving 75 aromatic hydrogens, equivalent to 15 benzenethiolates. Contamination from ubiquitous vacuum grease is apparent at 0.15 ppm and 1.56 ppm. The peaks at .91, 1.30 and 2.16 ppm show expected 68 hydrogens of TOA^{+}, although the α hydrogens are at 2.1 ppm, rather than at the 3.1 ppm found in TOABr.

The aromatic region in the ^{1}H-NMR of these clusters has no analog in the literature for gold thiolate MPCs, but similar largely spaced features bearing little semblance to benzenethiol or diphenyldisulfide have been reported for

$Cd_{32}S_{14}(SPh)_{36}$*DMF_4 quantum dots.[12] The aromatic region is compared with benzenethiol and diphenyldisulfide in Figure 3.10. The number of hydrogen resonances and their multiple chemical shifts are not surprising if there are multiple binding sites on the cluster surface (vertices, faces, and edges), ring polarization when bound to gold, and/or orientation of the ring relative to the surface to yield ortho hydrogen atoms that are magnetically non-equivalent (differing electronic environments). The varying types of

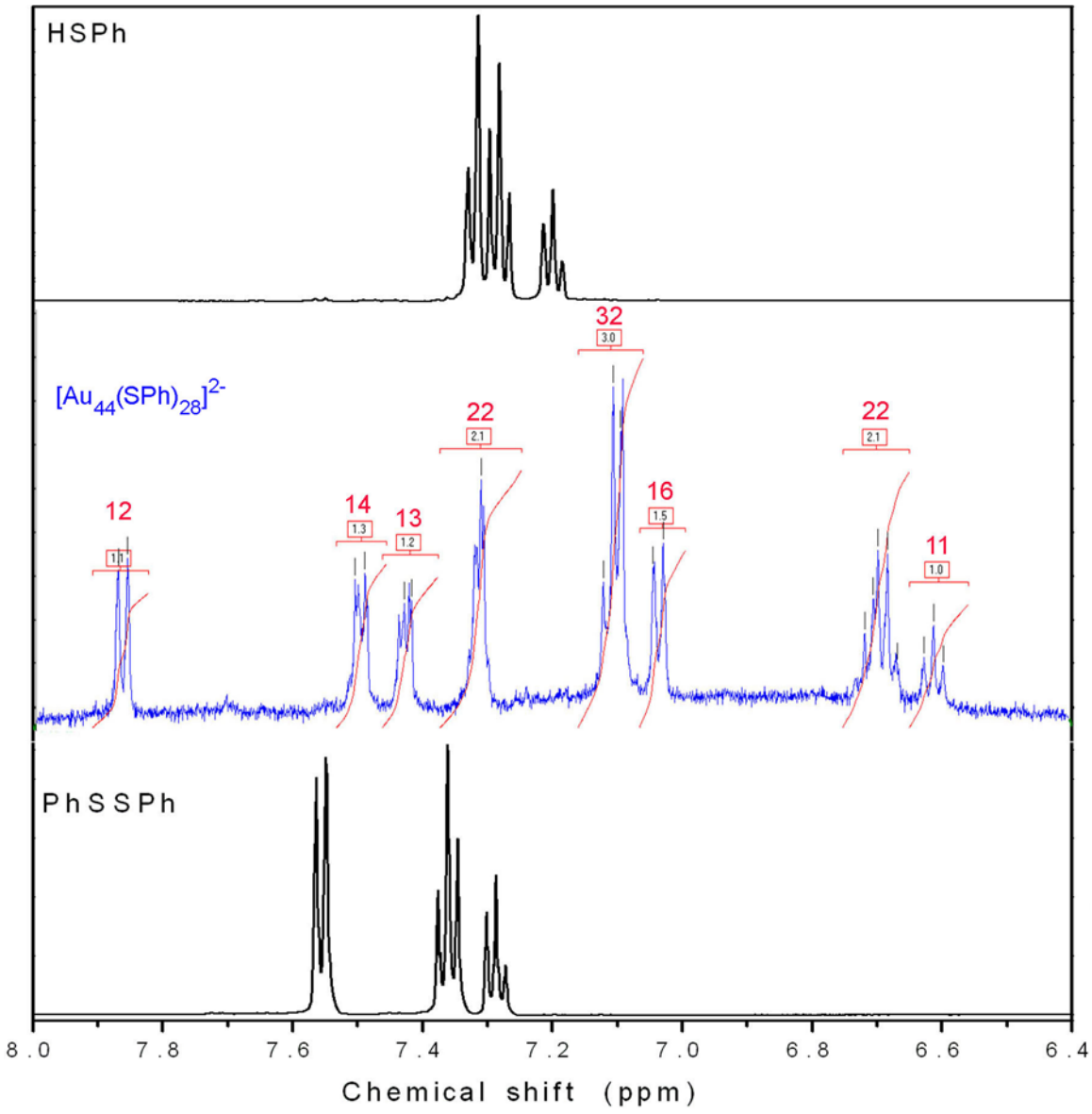


Figure 3.10 Aromatic ^{1}H-NMR spectrum of benzenethiol,$[Au_{44}(SPh)_{28}]^{2-}$, and diphenyldisulfide (top to bottom). Integrated peak areas for $[Au_{44}(SPh)_{28}]^{2-}$ are labeled in red and the areas written above each peak are scaled to represent the expected 140 hydrogen atoms of 28 benzenethiolate ligands. The integrated peak areas for benzenethiol and diphenyldisulfide are simply 2:2:1 from left to right, corresponding to (o)rtho, m(eta), and p(ara) hydrogens of the aromatic ring.

benzenethiolate binding sites present in $TOA_2[Au_{44}(SPh)_{28}]$ were revealed by 2-D proton correlated spectroscopy (COSY ^1H). The COSY-^1H spectrum is shown in Figure 3.11. Three distinct benzenethiolate moieties are indicated. Their resonances, J_{H-H} coupling values, and quantity are tabulated in Table 3.2. No simple structural model is apparent

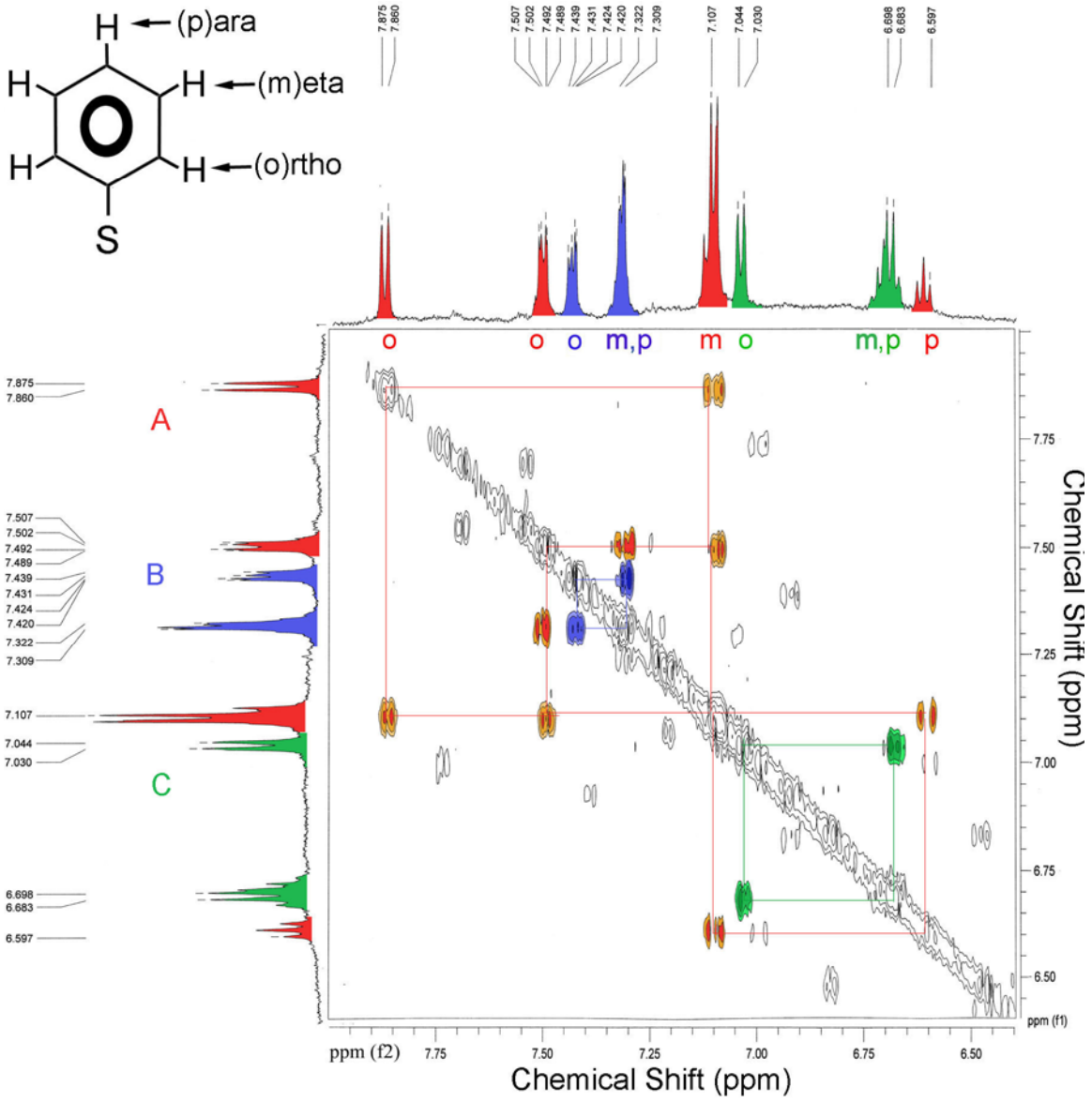


Figure 3.11 COSY-^1H spectrum of $[Au_{44}(SPh)_{28}]^{2-}$. The correlated hydrogen atoms for each type of benzenethiolate present are color-coded and labeled with letters to the left (A,B,C). The two axes are the same, with the colored squares connecting correlated hydrogens. The peak assignments (ortho, meta or para) are indicated under the appropriate peak on the x-axis for reference to the benzenethiolate molecule shown in the upper left corner.

Table 3.2 ^{1}H-NMR peak assignments, multiplicity and J_{H-H} coupling constants. In parenthesis are shown the multiplicities (d=doublet, t = triplet, dd = doublet of doublets, m = complex multiplet) and J_{H-H} coupling constants in Hz. The color coding for the $[Au_{44}(SPh)_{28}]^{2-}$ matches that used in Figure 3.11 to ease viewing and interpretation.

Hydrogen Location	HSPh	PhSSPh	$[Au_{44}(SPh)_{28}]^{2-}$			1.5 nm $Cd_{32}S_{14}(SPh)_{36}$ ref. 12
			SPh A	SPh B	SPh C	
ortho	7.32 (d, 8.0)	7.56 (d, 3.8)	7.87,7.50 (d, 3.5)	7.43 (d, 4.3)	7.03 (d, 3.3)	7.91(d)
meta	7.28 (t, 4.0)	7.36 (t, 7.5)	7.11 (t, 7.3)	7.32 (m, 4.5)	6.88 (t, 7.0)	7.03 (dd)
para	7.20 (t, 8.0)	7.29 (t, 7.5)	6.61 (t, 7.3)	7.32 (m, 4.5)	6.72 (t, 7.0)	6.92 (t)
# SPh on cluster	N/A	n/A	14	7	7	36

for this cluster from the 14:7:7 benzenethiolate ratio for three differently bound benzenethiolates. The benzenethiolates labeled B and C have an overall spectral width near those of benzenethiol and diphenyldisulfide, respectively. This is demonstrated in Figure 3.12. Although the COSY-^{1}H spectrum shows the two aromatic rings of species B and C are not coupled, it is possible they are non-equivalent aromatic rings of a surface bound species resembling diphenylsidulfide, where binding to gold breaks the coupling between the two rings. This would result in only two types of species bound to the surface and unfortunately most structural models can accommodate two types of binding sites, thus preventing an absolute structural determination. A full structural determination by x-ray crystallography will no doubt resolve this matter in the future. Although ^{13}C-NMR failed to produce spectra of these clusters, 2-D heteronuclear ^{13}C-^{1}H NMR under high saturation quantum coherence excitation (HSQCE) conditions provided an indirect measure of some of the ^{13}C-NMR resonances for the aromatic rings. [13] This spectrum is displayed in Figure 3.13. The information provided by this spectrum is that the ortho

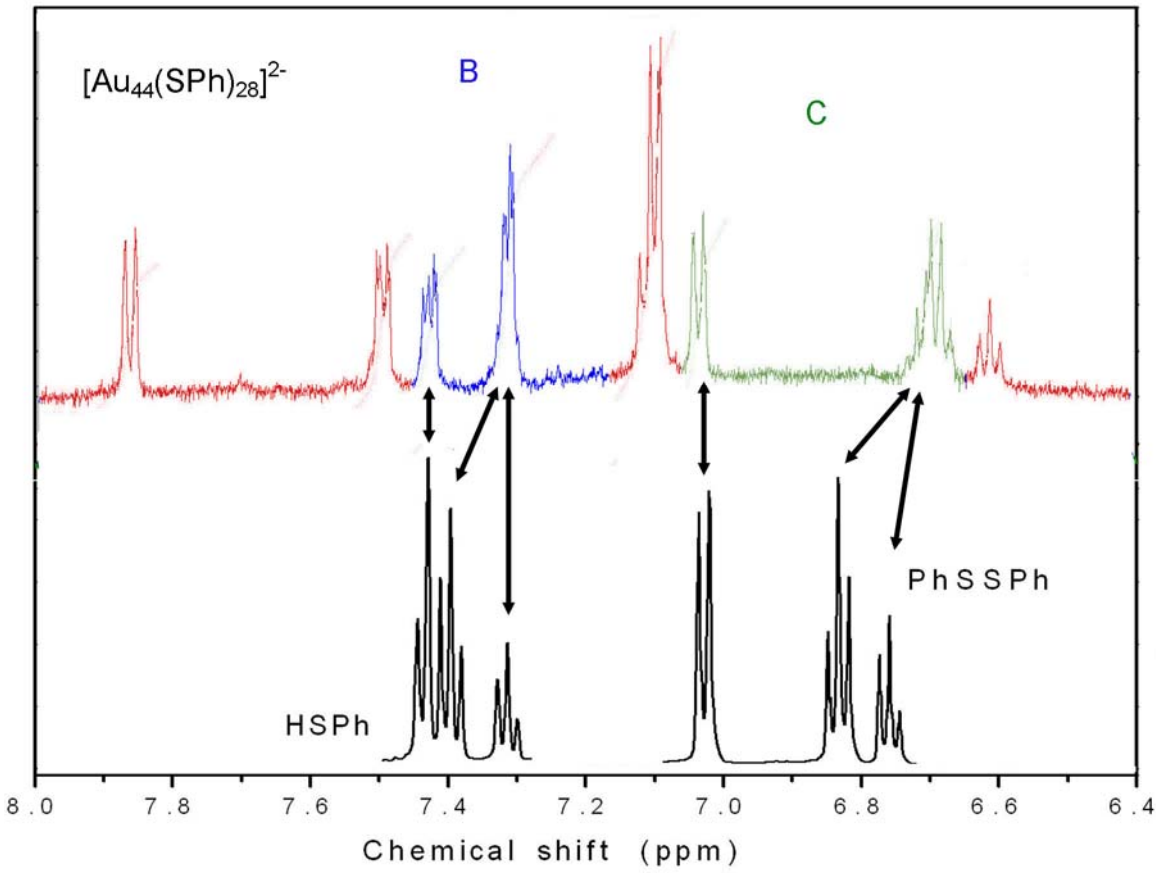


Figure 3.12 Comparison of specific $[Au_{44}(SPh)_{28}]^{2-}$ to benzenethiol (HSPh) and diphenyldisulfide (PhSSPh). The two lower reference spectra are shifted from their normal locations and ortho hydrogens are aligned between the cluster and reference spectra. Arrows are included to indicate the matches between peaks, which admittedly may be coincidental.

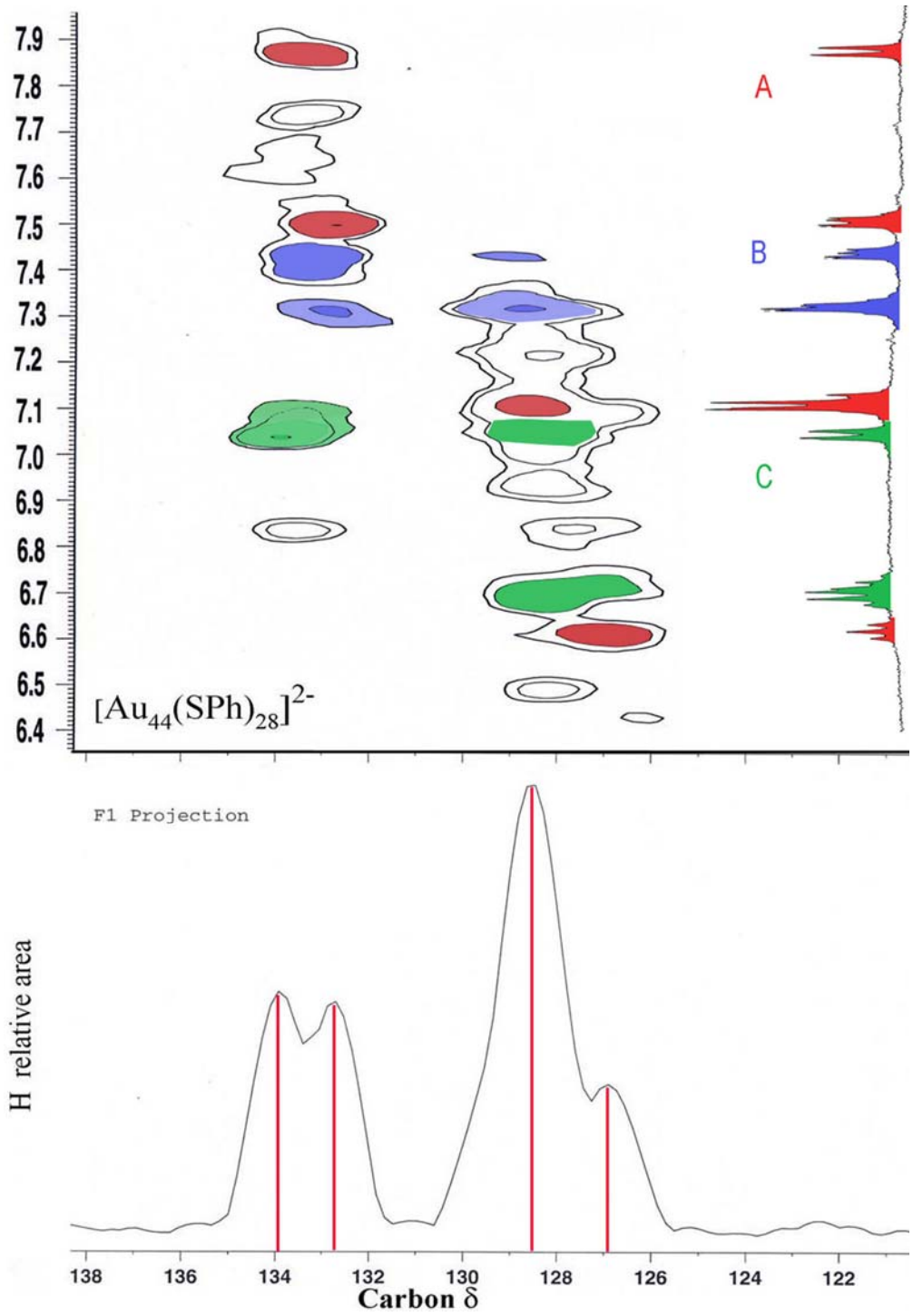


Figure 3.13 HSQCE ^{13}C-^{1}H NMR spectrum for $[Au_{44}(SPh)_{28}]^{2-}$ (top) with ^{1}H-NMR on right for reference. The vertical axis indicates the ^{1}H chemical shifts and the horizontal the ^{13}C chemical shifts. The lower plot is a projection of the ^{1}H signal areas as a function of ^{13}C-NMR chemical shift, thereby estimating the ^{13}C-NMR resonances. In all cases ortho hydrogens are on non-equivalent carbon atoms. Additional hydrogen resonances emerge under saturation conditions, implying a fourth, minor binding mode. Red vertical lines are provided to guide the eye to approximate dominant ^{13}C chemical shifts.

hydrogens on each aromatic ring are bound to magnetically nonequivalent carbons. For each type of benzenethiolate there is always at least one ortho carbon chemical shift downfield by 3.0 or more ppm than either benzenethiol or diphenyldisulfide. The meta and para chemical shifts are all downfield by 1.0 ppm or more as well. In the case of benzenethiolate A, both ortho resonances are downfield from those of benzenethiol or diphenyldisulfide, while the meta is upfield and the para is downfield. The B and C benzenethiolates both possess an ortho hydrogen that appears upfield from either benzenethiol or diphenyldisulfide, while their difficult to distinguish meta and para chemical shifts are downfield these two reference materials. This information is provided in tabular form in Table 3.3. All spectra were collected by the method outlined in the previous chapter with a Bruker DRX-500 NMR spectrometer in the Georgia Institute of Technology NMR lab with or by Dr. Les. Gelbaum. The spectrum was consistently reproduced for seven different synthetic batches of this material.

Table 3.3 ^{13}C-NMR of $[Au_{44}(SPh)_{28}]^{2-}$ compared to benzenethiol (HSPh) and diphenyldisulfide (PhSSPh). Nearly all resonances are shifted downfield to higher chemical shifts due to deshielding effects upon binding to gold.

C ring location	PhSSPh	HSPh	$[Au_{44}(SPh)_{28}]^{2-}$		
			A PhS-	B PhS-	C PhS-
ortho	131.0	129.5	133.9 132.5	132.5 129.0	134.0 128.3
meta	129.1	129.4	133.5 128.5	132.4	~127.0
para	126.9	125.9	127.0	128.5	~127.0

3.2.5 Infrared and Raman Spectroscopy

3.2.5.1 Infrared Spectroscopy

The infrared spectrum of the TOA2[$Au_{44}(SPh)_{28}$] quantum dots is unremarkable, being dominated by six benzenethiolate ring mode absorption bands at 617, 734, 1025, 1478, 1583, and 1653cm^{-1} with a weak band for the aromatic C-H stretching at 3073 cm^{-1}. The relative intensity enhancement of the asymmetric in-plane ring vibration ($b_{2\ mode}$) at 617 cm^{-1} is common to all $Au_x(SPh)_y$ clusters. The alkane C-H stretches of TOABr are prevalent at 2963, 2916, and 2847 cm^{-1}. The spectrum is presented in Figure 3.14. The IR bands are not significantly shifted in frequency relative to pure benzenethiol. This material is free of unbound benzenethiol, as evidenced by the lack of a S-H stretch at 2567 cm^{-1}.

3.2.5.2 Raman Spectroscopy

Applying the techniques outlined in Chapter 2.3.6.2 did not provide vibrational spectra of surface bound benzenethiolates in the $TOA_2[Au_{44}(SPh)_{28}]$ quantum dots. A broad luminescence rather than a Raman spectrum was obtained and is shown in Figure 3.15. The absence of Raman scattering features for benzenethiolate on this MPC likely results from a significantly enhanced luminescence within the cluster relative to larger clusters. There are numerous reports of broad near-infrared photoluminescence over the spectral range .75 to 1.9 eV for 0.9 to 1.9 nm core gold MPCs protected by a variety of non-aromatic thiolates. Raman spectra of these surface species remain unreported or undetected.[14a-g] The 1.1 nm $\sim Au_{38}(SCH_2CH_2Ph)_{24}$ MPC has been reported to have a photoluminescence quantum efficiency of .012 , whereas values between ~$4.4x10^{-5}$ and

$1.8x10^{-4}$ are reported for 1.7 nm ~Au_{140}(S-alkyl)$_{53}$ MPCs.[14a,g] This represents an ~10^2 enhancement of photoluminescence processes for 1.1 nm clusters compared to 1.7 nm clusters and could easily obscure Raman scattering with its typical quantum efficiency of only ~10^{-7}. The net effect of these efficiencies would mean the quantum efficiency of luminescence for 1.1 nm clusters would be $12x10^3$ greater than that of Raman scattering, but photoluminescence would only be 44 to 180 times more efficient in 1.7 nm clusters. Any scattering features present could be completely obscured by the luminescence under these conditions, as observed. Despite the clusters absorbing little energy at 1.165 eV (ε = 222 from Figure 3.3), as a solid they are very concentrated (~396 mM from the XRD volume of 4.19 nm^3 per cluster), giving an absolute absorbance of ~8.79 per *millimeter* of sample. This strong absorbance could readily prevent scattering, further reducing the detectable Raman scattering.

3.3 Summary

This chapter entails the generation and characterization of a gold quantum dot with a discrete, known composition, discerned from MALDI-TOF mass spectrometry by its parent anion. Its molecular formula is $TOA_2[Au_{44}(SPh)_{28}]$ with a 1.1 nm core diameter evident from LAXRD data, matching the theoretical 1.1 diameter calculated by the approximation described in Figure 1.13. It has a rich optical spectrum showing quantum confinement of gold electrons and its highest energy transition is possibly a closed to open shell electronic transition (Figure 1.13 and Tale 3.1). It has a distinct ^{1}H-NMR spectrum characteristic of gold-thiolate interactions that are not fully understood at this

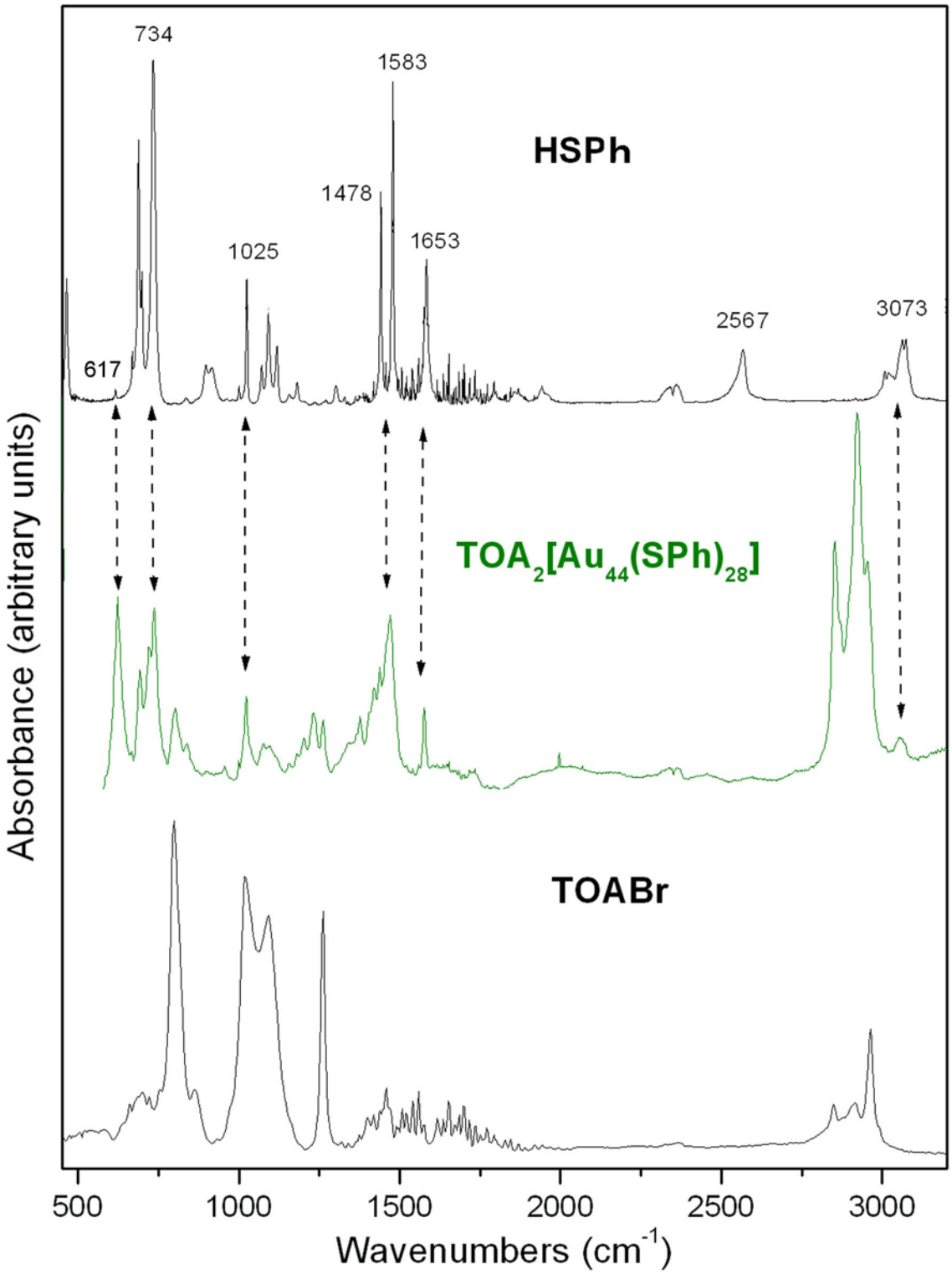


Figure 3.14 IR absorbance spectrum of $TOA_2[Au_{44}(SPh)_{28}]$ with benzenethiol (above) and TOABr (below) for reference. Arrows correlate prevalent benzenethiolate features.

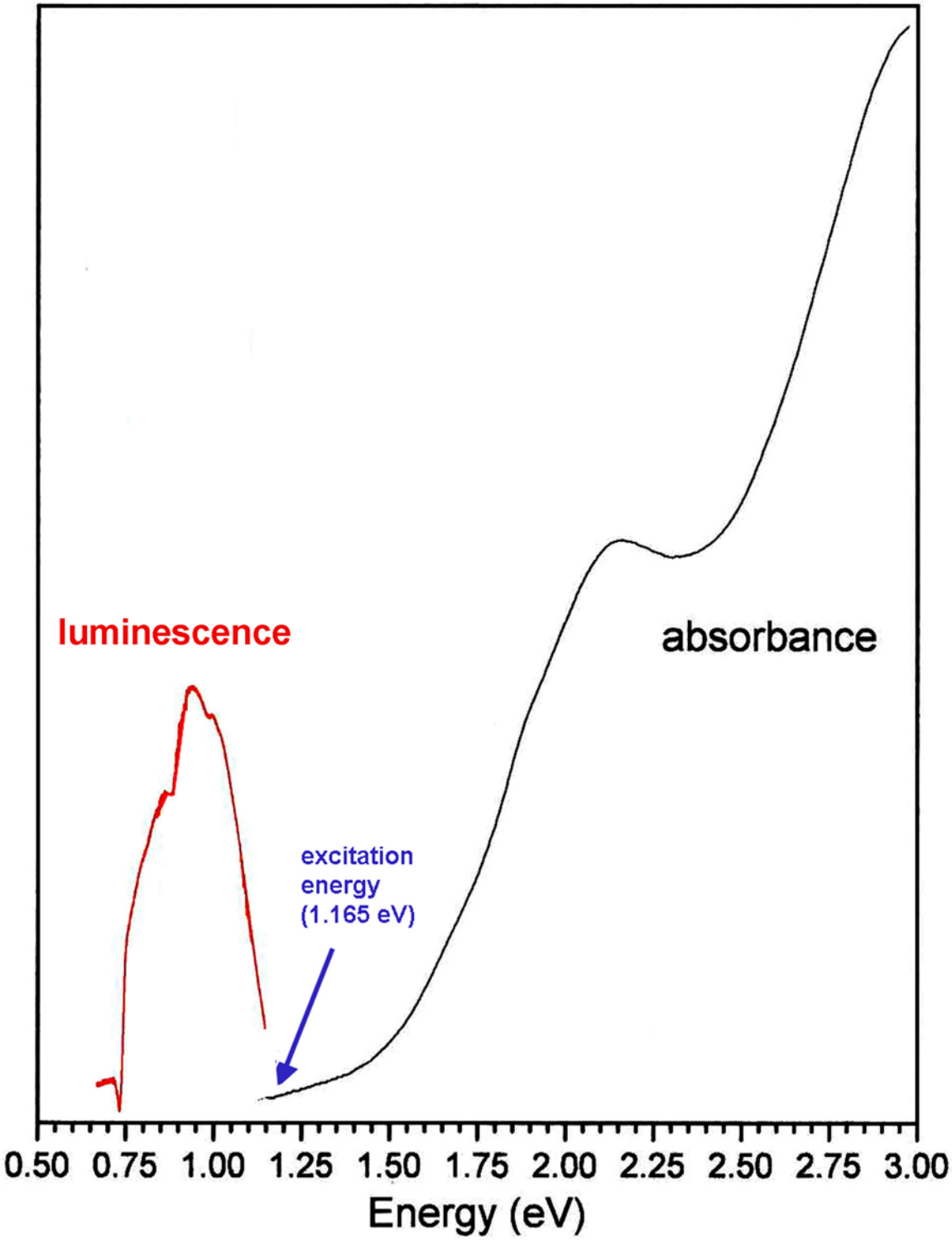


Figure 3.15 Photoluminescence of $TOA_2[Au_{44}(SPh)_{28}]$. Luminescence feature shown (red) is scaled arbitrarily to absorbance to show the peak profile of the luminescence and the lowest energy electronic transition. The actual photoluminescence intensity has not been measured. The high energy cutoff for luminescence detection is fixed at 1.147 eV by a notch filter.

time, but may be resolved in the future by total structure determination (x-ray crystallography). The clusters emit a broad diffuse light from .75 eV to the instrumental detection limit of 1.147 eV photoluminesce upon 1.165 eV (1064 nm) photoexcitation. A photograph of a dilute solution of this cluster is shown in Figure3.16. A new, efficient synthesis of this interesting material would prove valuable for understanding quantum confined metallic clusters, as well as for electronic device research.

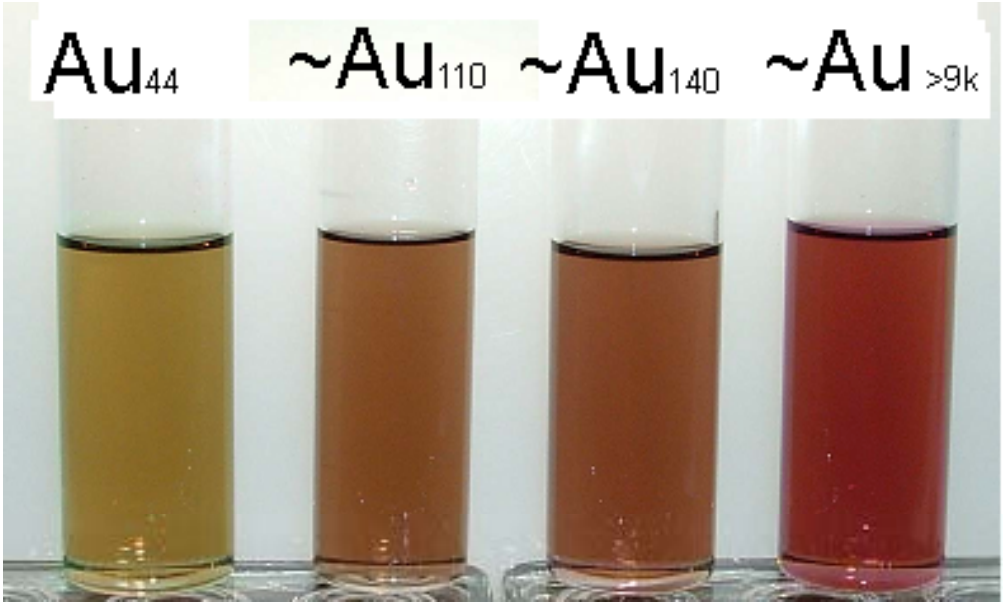


Figure 3.16 Photographs of gold quantum dot dilute solutions. (Left to right) $TOA_2[Au_{44}(SPh)_{28}]$, $\sim TOA_{4\text{-}6}[Au_{110}(SPh)_{62}]$,~ $TOA_{2\text{-}3}[Au_{140}(SPh)_{78}]$, and colloidal 6.8 nm $Au_x(S\text{-hexyl})_y$ in dilute toluene solution. Note the lack of reddish-purple coloration from the surface plasmon in the three small ($\leq$ 1.8 nm) clusters, as well as the olive coloration of the $TOA_2[Au_{44}(SPh)_{28}]$ clusters.

Chapter 3 References

(1) Schaaff, G.; Whetten, R. *J. Phys. Chem B* **1999**, *103*, 9394

(2) Wilcoxon, J.; Provencio, P. *J. Phys. Chem. B* **2003**, *107*, 12949

(3) Shon, Y.; Mazzitelli, C.; Murray, R. *Langmuir* **2001**, *17*, 7735

(4) Song, Y.; Murray, R. *J. Am. Chem. Soc.* **2002**, *124*, 7096

(5) Bigioni, T.; Harrell, L.; Cullen, W.; Guthrie,D.; Whetten, R.; First, P. *Eur. Phys. J. D.*, **1999**, *6*, 355

(6) Negishi, Y.; Katsuyuki, N.; Tsukuda, T. *J. Am. Chem. Soc.* **2005**, *127*, 5261

(7) Vollenbroek, F.; Van den Berg, J.; Van der Velden, J.; Bour, J. *Inorg. Chem.* **1980**, *19*, 2685

(8) Khoury, J. *Ph.D. Dissertation* **1999**, University of California Los Angeles

(9) Li, J.; Li., X; Zhai, H.; Wang, L. *Science* **2003**, *299*, 864

(10) Ajie H., Alvarez M., Anz S., Beck R., Diederich F., Fostiropoulus K, Huffman D., Kratschmer W., Rubin Y., Schriver K., Sensharma D., Whetten R. *J. Phys. Chem.* **1990**, *94*, 8630

(11) H. Hanniken, *Private communication **2005***

(12) Torimoto T., Kontani H., Shibutani Y., Kuwabata S., Sakata T., Mori H., Yoneyama H. *J. Phys. Chem. B.* **2001**, *105*, 6838

(13) *Structural Methods in Inorganic Chemistry 2nd Ed.*; CRC Press, **2004**, 8-52

(14) (a) Bigioni, T.; Whetten, R.; Dag, O. *J. Phys. Chem. B.* **2000**, *104*, 6983 (b) Huang, T; Murray, R. *J. Phys. Chem. B.* **2001,** *105*, 12498 (c) Link, S.; Beeby, A.; Fitzgerald, S.; El-Sayed, M.; Schaaff, T.; Whetten, R. *J. Phys. Chem. B.* **2002**, *106*, 3410 (d) Lee, D.; Donkers, R.; Wang, G.; Harper, A.; Murray, R. *J. Am. Chem. Soc.* **2004**, *126*, 6193 (e) Negishi, Y.; Takasugi, Y.; Sato, S.; Yao, H.; Kimura, K.; Tsukuda, T. *J. Am. Chem. Soc.* **2004**, *126*, 6518 (f) Negishi, Y; Nobusada, K.; Tsukuda, T. *J. Am. Chem. Soc.* **2005**, *127*, 5261 (g) Wang, G.; Huang, T.; Murray, R.; Menard, L.; Nuzzo, R. *J. Am. Chem. Soc.* **2005**, *127*, 812

CHAPTER 4

SMALLER GOLD:ALKANETHIOLATE MPCS BY ETCHING

4.1 Size Reduction of 2.0 ± 0.5 nm Au_x(dodecanethiolate)$_y$ MPCs

The production of smaller $Au_x(SPh)_y$ clusters from larger clusters by oxidative etching described in the previous chapter suggested the same conditions could be applied to the more widely known Au_x(alkanethiolate)$_y$ MPCs. To test this hypothesis, Au_x(dodecanethiolate)$_y$ clusters were generated by well-known methods with no size separation performed.[1] This yielded 2.0±0.5 nm core ~$Au_{100\text{-}400}$(dodecanethiolate)$_y$ MPCs with at least half of the MPC cores having a 1.7 nm diameter. These clusters were oxidatively etched by using the procedure described below.

Polydisperse Au_x(dodecanethiolate)$_y$ MPCs (83 mg, ~1.95 μmoles) were dissolved in tetrahydrofuran (15 mL). Next, dodecanethiol (4.2 mmol, 1 mL) and 30 % aqueous H_2O_2 (50 μL, 489 μmoles) were added, followed by stirring for 24 hours at room temperature. The solution was brown-violet after 24 hours, indicating no visible change. An additional 50 μL (489 μmoles) of 30 % aqueous H_2O_2 was added and stirred overnight. This step was undertaken with the assumption that a long, well-packed alkyl chain on the MPC would be more effective at protecting the cluster surface from oxidation than benzenethiolate. The reaction solution was turbid and green after another 24 hours, similar to the reaction described in the previous chapter.

The reaction solution was dried and dispersed in acetone (100 mL), then injected through a .2 μm syringeless filter. The acetone insoluble products were eluted from the

filter with hexanes, dried, and massed at 8.7 mg. Optical absorption spectroscopy of the product showed much more structure between 1.5 and 3.0 eV than the starting material, as well as no evidence of a plasmon absorbance. A strong absorbance onset at ~3.8 eV with a maxima at ~4.4 eV suggested contamination from (Au:dodecanethiolate)$_x$ polymeric material. To purify the MPCs, the mixed products were dispersed in hexanes (10 mL) and acetone (15 mL). Addition of 10 mL every 24 hours for two days (35 mL total acetone) precipitated a white-gray solid. The remaining soluble greenish brown material was injected through a .2 μm syringeless filter for comparison with the precipitated solids and starting material by optical spectroscopy. The yield of soluble clusters was 3.2 mg, limiting characterization to optical absorbance spectroscopy. Further investigation could optimize this reaction or at the very least produce more sizeable quantities for further characterization.

4.2 Optical Characterization of Etched Au_x(dodecanethiolate)$_y$ Quantum Dots

The clusters have a unique optical spectrum, somewhat similar to $TOA_2[Au_{44}(SPh)_{28}]$, but with lower energy electronic transitions as shown in Figure 4.1. The most evident optical features for this cluster closely resemble known Au_{25}(glutathionate)$_{18}$ and ~Au_{38}(dodecanethiolate)$_{24}$ or even a mixture of these two core sizes.[3,4] Figure 4.2 compares this cluster to other known clusters it resembles, which include ~1.3 nm Au_x(hexanethiolate)$_y$ clusters previously observed.[4] The etching reaction has only been applied with thiols identical to those already bound to the cluster surface. Using a thiol that differs from the bound thiolates may produce clusters passivated by thiols that are normally unobtainable under the harsh reducing conditions used to form gold MPCs

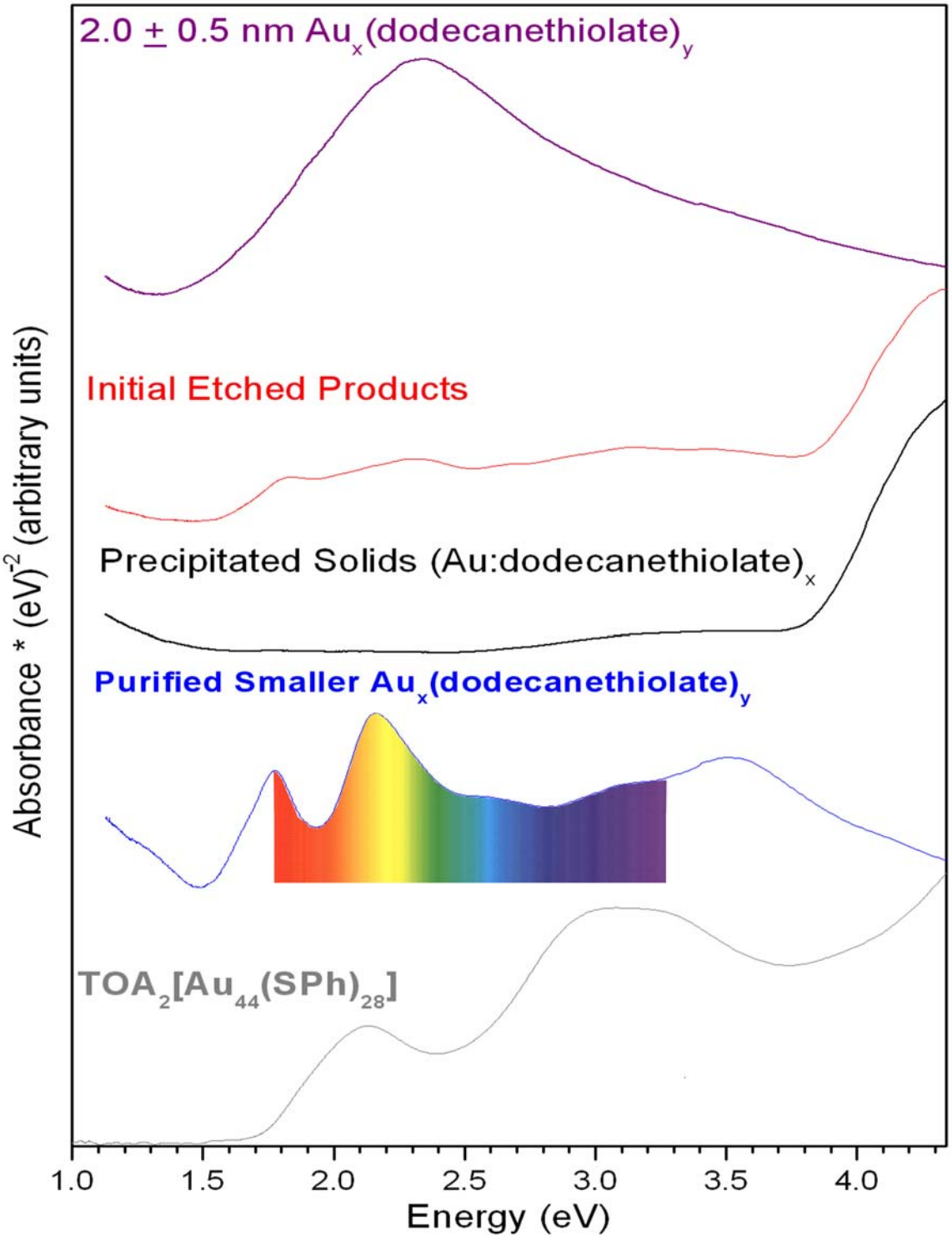


Figure 4.1 Optical spectra (top to bottom) of starting clusters, mixed etch products, precipitated impurities, small $Au_x(dodecanethiolate)_y$ quantum dots, and $TOA_2[Au_{44}(SPh)_{28}]$ quantum dots. No evidence of the starting material is present in the etched product. The brown-green coloration arises from transmission of red, green, and some violet light, as shown by the visible spectrum provided.

(described in Chapter 2). Thiols fitting this description that have failed to produce non-colloidal $Au_x(thiolate)_y$ MPCs include perfluorobenzenethiol, linear fluorocarbons, 4-aminobenzenethiol, 4-nitrobenzenethiol, and a variety of thiolated DNA bases that includes purinethiol,2-thiouracil, 2-mercaptopyridine, and 2-mercaptopyrimidine. This preliminary investigation shows oxidative etching as a general approach for generating gold quantum dots of fewer than 100 atoms from larger gold MPCs with more than 100 core atoms.

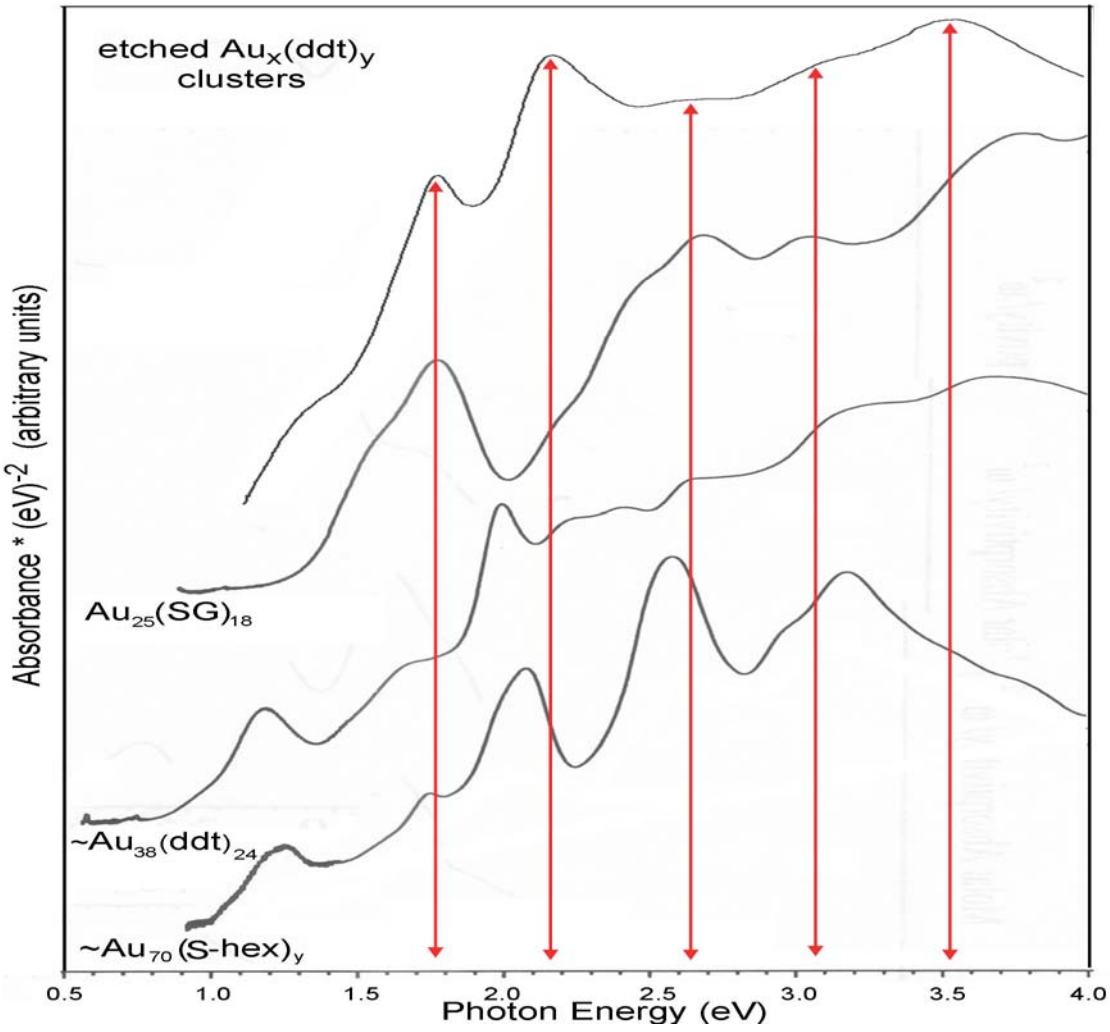


Figure 4.2 Optical spectrum of oxidatively etched $Au_x(dodecanethiolate)_y$ clusters compared with similar gold clusters. Red lines denote dominant absorbances. Similar clusters shown are passivated with glutathionate (SG), dodecanethiolate (ddt), or hexanethiolate (S-hex). Lower three optical spectra taken from reference 2.

Chapter 4 References

(1) Schaaff, G.; Shafigullin, M.; Khoury, J.; Vezmar, I.; Whetten, R. *J. Phys. Chem. B* **2001**, *105*, 8785

(2) Khoury, J. *Ph.D. Dissertation* **1999**, University of California Los Angeles

(3) (a) Schaaff, G.; Knight, G.; Shafigullin, M.; Borkman, R.; Whetten, R. *J. Phys. Chem. B* **1998**, *102*, 10643 (b) Negishi, Y.; Takasgui, Y.; Sato, S.; Yao, H.; Kimura, K.; Tsukuda, T. *J. Am. Chem. Soc.* **2004**, *126*, 6518

(4) Schaaff, G.; Shafigullin, M.; Khoury, J.; Vezmar, I.; Whetten, R.; Cullen, W.; First, P. *J. Phys Chem. B* **1997**, *101*, 7885

CHAPTER 5

ALKANETHIOL PASSIVATED 1.5 NM GOLD CORE QUANTUM DOTS

5.1 Production of 1.5 nm Au_x(tert-butylmercaptan)$_y$ MPCs

The use of benzenethiolate as a protective monolayer for generating smaller gold clusters than normally produced through the use of linear alkanethiols detailed in chapter 2 prompted the use of tert-butyl-mercaptan (tbm) for the same purpose. It is reasonable to believe thiols with sufficient steric hindrance (cone angle), such as tbm and benzenethiol, yield smaller core sizes than less bulky alkane and arene thiols. Small gold clusters with average diameter ~1.5 nm were prepared with tert-butylmercaptan (2-methyl-2-propanethiol), thereby demonstrating the viability of kinetic control of gold cluster size by simple thiols. The MPCs were generated by the Brust method with stoichiometric modification previously reported by Whetten et. al. [1,2] The synthesis was performed at room temperature as follows and is shown schematically in Chapter 2, Figure 2.1.

Tetraoctylammonium bromide (.3348 g, .6 mmol) and *tert*-butyl mercaptan (174.5 *u*L, 1.5 mmol) were combined in toluene (40 mL). Aqueous $HAuCl_4$ (10 mL, .05 M) was added and the mixture was stirred vigorously for two hours until the aqueous phase was clear with a turbid, white toluene phase. Aqueous sodium borohydride (10 mL, .50 M) was added rapidly and stirred for 24 hours. The reaction mixture was dried to a minimal volume and an excess (200 mL) of ethanol added, followed by storage for 72 hours at 0 ^{o}C to allow cluster precipitation. The light brown supernatent was decanted and the remaining solids were filtered and rinsed on a fine frit with excess ethanol (~500 mL).

The MPCs were eluted from the frit with toluene. The isolated toluene soluble MPCs massed 53 mg. This mass represented a gold mass yield of ~ 43.7 %, determined using the molecular weight estimated from the MPC mass spectrum.

This synthesis proved surprisingly simple, proceeding exactly as would be expected with primary alkanethiols, with the exception of a small quantity of ethanol soluble clusters being present (~2.0 mg). The clusters generated are readily dispersed in toluene or dichloromethane, but not in hexanes. They are air-stable as a powder for at least a week, but unstable after about three weeks. The decomposition produces a distinct odor in sealed vials of the dry clusters that resembles ethanethiol, a molecule added to natural gas for rapid detection of gas leaks. In toluene solution, these MPCs decompose completely after about a week. Despite this instability, it is encouraging to find that thiols with sufficient steric hindrance (cone angle) can yield smaller core sizes than less bulky alkane and arene thiols under Brust-type synthetic conditions. This shows promise for kinetically controlling the growth of small metallic clusters. The lability of tert-butylmercaptan may actually be an asset for oxidative etching reactions (described in Chapters 3 and 4) incorporating thiols that are incompatible with the Brust-sythesis to displace tbm. Additionally, coupling this methodology with thermodynamic control (low temperatures) as reported by Murray, et. al may further reduce the average diameter of the clusters.[3-5]

5.2 Physical Properties of $Au_x(tbm)_y$ MPCs

5.2.1 Optical Spectroscopy

The optical spectrum of the $Au_x(tbm)_y$ MPCs closely resembles similarly sized ~$TOA_{4\text{-}6}[Au_{110},(SPh)_{62}]$ detailed in chapter 2 and Au_x(hexanethiolate)$_y$ MPCs.[6] The $Au_x(tbm)_y$ MPCs possess a gradual absorption onset in the near-infrared below 1.5 eV with an absorbance maxima near 2.4 eV that has lower intensity than a surface plasmon. The optical spectrum is shown with optically similar MPCs in Figure 5.1. The spectra all possess subtle inflection points that are most evident from the derivative plot of the optical spectra, shown in Figure 5.2. The optical properties of these clusters very clearly match those of ~1.5 nm Au_x(hexanethiolate)$_y$ MPCs, which is not surprising given the similarity in core size and that they are both passivated with alkanethiols. The differential optical plot also shows that slight variations in the metallic density of states occur with different thiols. Further development of this concept could lead to tuning of the gold core states by selecting thiols with the desired properties (electron rich or withdrawing). All optical spectra were collected as detailed in Chapter 2.

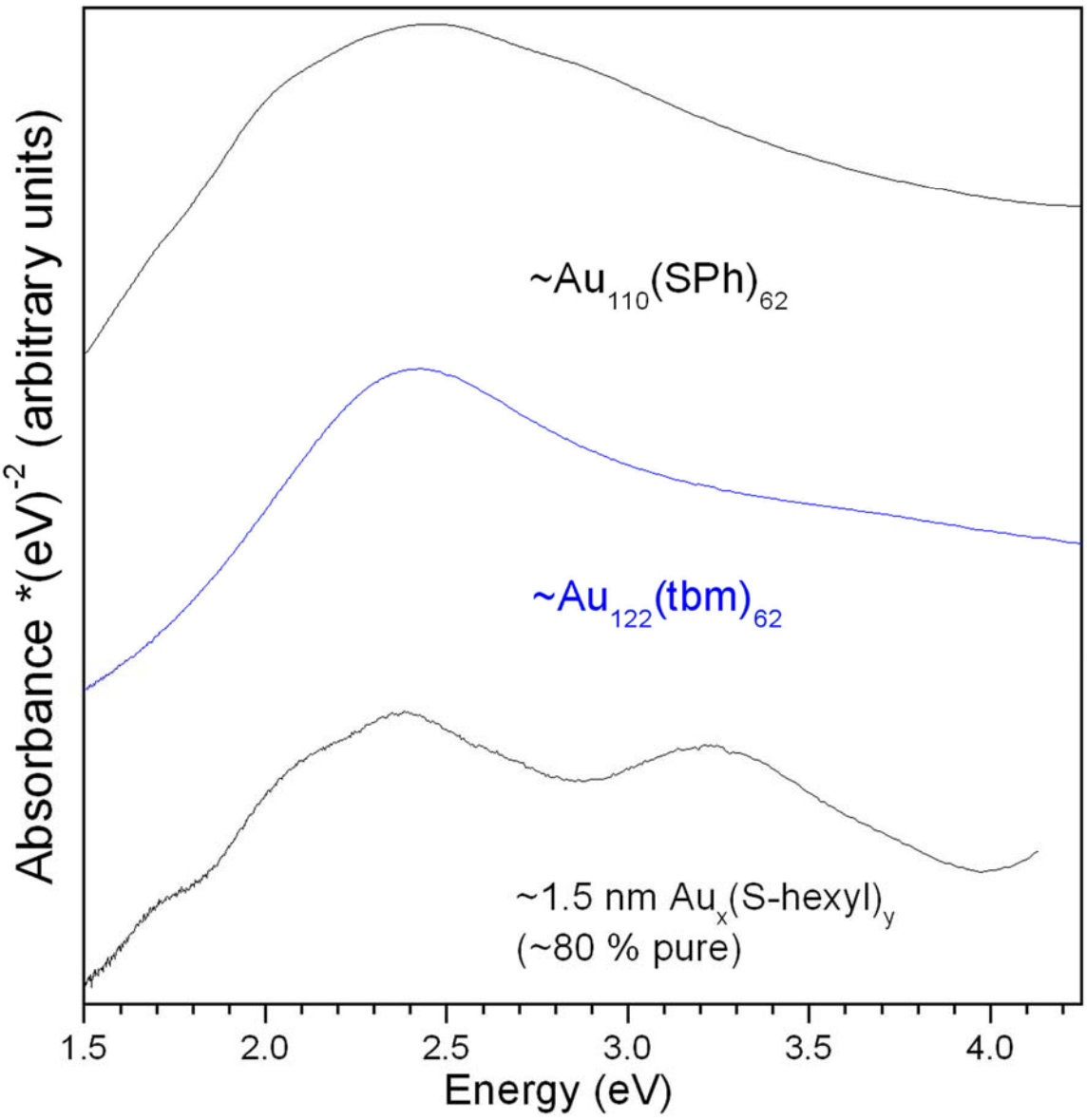


Figure 5.1 Optical spectra (top to bottom) of ~$Au_{110}(SPh)_{62}$, $Au_x(tbm)_y$, and ~$Au_{110}(S\text{-hexyl})_y$. The optical spectrum of the clusters was collected from a dilute (< 100 μM) dichloromethane solution.

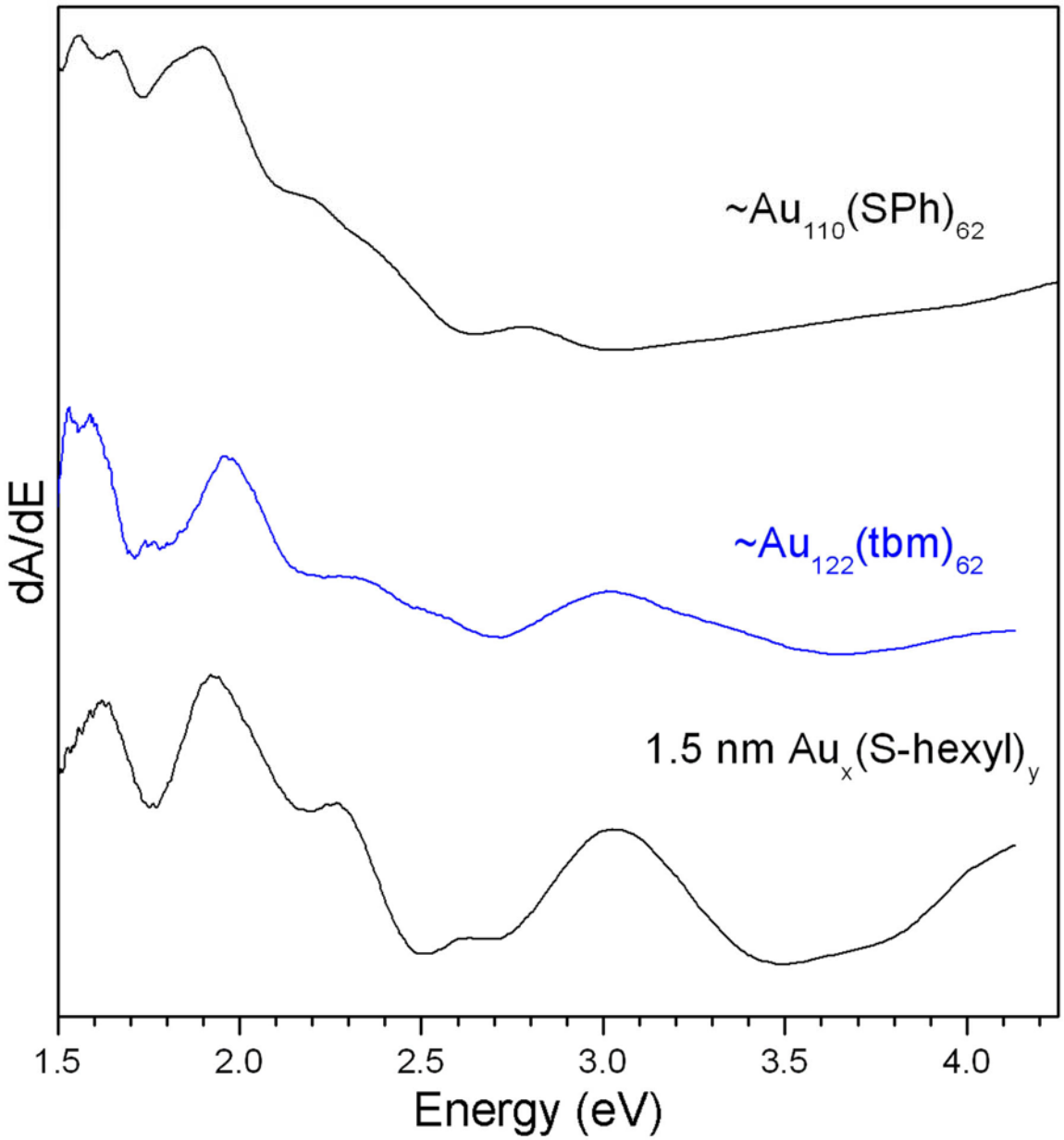


Figure 5.2 Differential optical spectrum (top to bottom) of ~$Au_{110}(SPh)_{62}$, $Au_x(tbm)_y$, and ~$Au_{110}(S\text{-hexyl})_y$. The close resemblance between the lower two spectra and their variance from the top spectrum shows the influence the thiolate protective monolayer can have on the core electronic properties. The higher absorbance at 3.0 eV in the ~$Au_{110}(S\text{-hexyl})_y$ MPCs likely arises from the 20 % ~$Au_{140}(S\text{-hexyl})_{56}$ contamination in the sample.[6]

5.2.2 Powder X-ray Diffraction

5.2.2.1 Large Angle Diffraction (LAXRD)

Large angle x-ray diffraction ($2\theta = 10 - 140^0$; $s = 1.1 - 12.2\ nm^{-1}$) was utilized to estimate the average core size of the $Au_x(tbm)_y$ clusters by the experimental method outlined in Chapter 2.3.2.1. These MPCs produce a LAXRD pattern quite similar to $Au_x(SPh)_y$ MPCs and their $Au_x(S\text{-}hexyl)_y$ analogs. The diffraction pattern for the $Au_x(tbm)_y$ MPCs is shown in Figure 5.3. As the diffraction pattern resembles similarly sized alkyl passivated clusters, they likely possess the same decahedral core structure (described in Chapter 2.3.2.1). The diffraction peaks are also narrower than expected for a cluster with the number of core atoms present (determined by mass spectrometry in Chapter 5.2.3), just as observed with $Au_x(SPh)_y$ and $Au_x(S\text{-}hexyl)_y$ MPCs.

5.2.2.2 Small Angle Diffraction (SAXRD)

The $Au_x(tbm)_y$ have some long range ordering between nanocrystalline cores, evident by small angle x-ray diffraction ($2\theta = 0\text{-}10^0$; $s = 0\text{-}1.13\ nm^{-1}$). Only one small angle diffraction peak is present at $.491\ nm^{-1}$, indicating an average core-core distance of ~2.0 nm. Subtracting the 1.5 nm core diameter from this value yields a 0.5 nm edge to edge distance between adjacent gold cores. This distance is consistent with the shorter chain length of tert-butylmercaptan relative to the 0.8 nm spacing observed in $Au_x(butanethiolate)_y$.[2] The $Au_x(tbm)_y$ MPCs are .3 nm closer than $Au_x(butanethiolate)_y$ and ~.28 nm is expected due to it being shorter by two C-C bonds. Figure 5.4 shows the SAXRD patterns for the $Au_x(tbm)_y$ MPCs. The .54 nm edge to edge distance of these MPCs is near the .63 nm of the $\sim TOA_{4\text{-}6}[Au_{110}(SPh)_{62}]$ MPCs (Chapter 2.3.2.2), further

indicating the size similarity between tert-butylmercaptan and benzenethiol protective monolayers. The reciprocal of the small angle peak widths at half maximum indicates an average grain size of 6.0 nm thus the extended crystalline domains are ~ 3 nanocrystals in each dimension or about 27 nanocrystalline units in total volume. This volume of 27 nanocrystals per 216 nm^3 corresponds to a cluster density of 5.8 g/cm^3, compared to 19.3 g/cm^3 for bulk gold. Unfortunately these grain sizes are too small for x-ray crystallography.

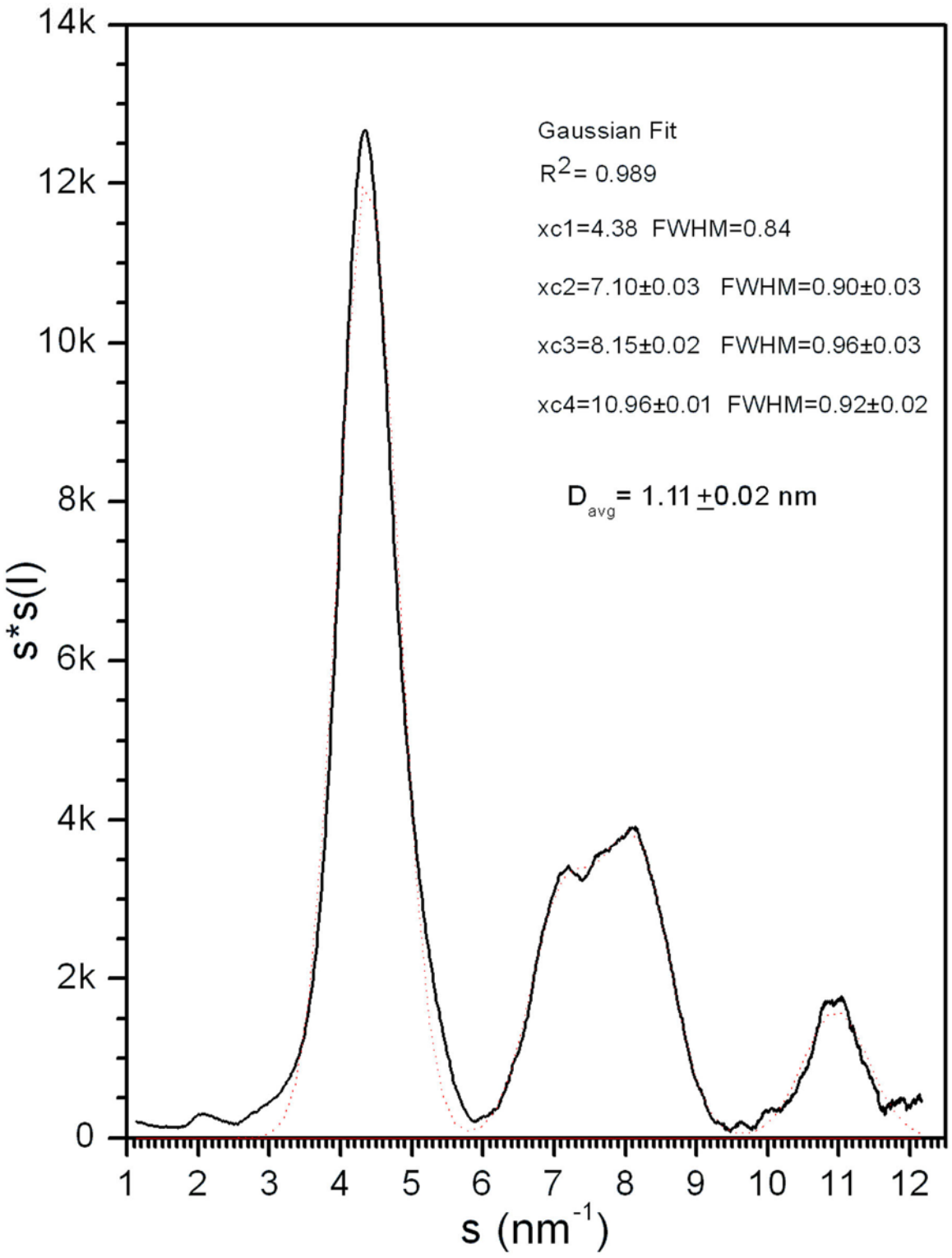


Figure 5.3 LAXRD for 1.5 nm $Au_x(tbm)_y$ MPCs. The location of the diffraction peaks (s) and their full widths at half maximum (Δs) are listed at the top right. A lower than expected diameter estimate is typical for gold MPCs below 2.0 nm diameter (as discussed in Chapter 2). The dotted red line represents the Gaussian function fitting the experimental plot.

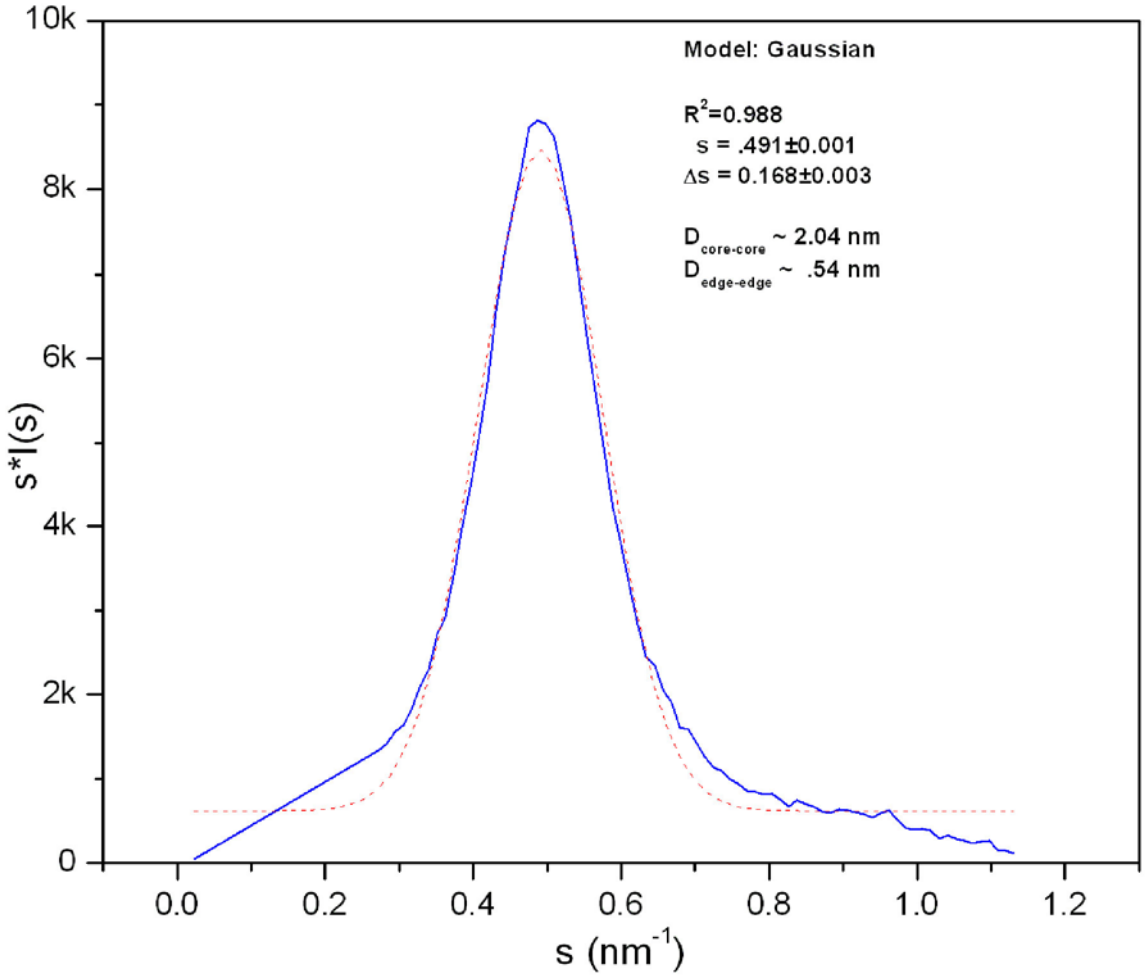


Figure 5.4 SAXRD for 1.5 nm $Au_x(tbm)_y$ MPCs. The peak location and its FWHM (Δs) are listed at the top right. The dotted red line represents the Gaussian function fitting the experimental plot.

5.2.3 MALDI-MS

The $Au_x(tbm)_y$ MPCs were evaluated by matrix assisted laser desorption ionization time of flight mass spectrometry (MALDI-TOF-MS) by the Georgia Institute of Technology Mass Spectrometry Facility as described in Chapter 2.3.3. The mass spectrum of these clusters strongly resembles that of the 1.5 nm $Au_x(SPh)_y$ MPCs detailed in Chapter 2. The mass spectral peak of the $Au_x(tbm)_y$ MPCs is centered at ~2.3 kDa higher mass than the corresponding $Au_x(SPh)_y$ MPCs, but has a similar peak width (FWHM) of 1987 Da. These values are consistent with a $Au_{122}S_{62}^-$ anion, giving the cluster a nominal molecular formula of $Au_{122}(tbm)_{62}$. The mass spectrum for these clusters and the analogous $Au_x(SPh)_y$ MPCs are shown in Figure 5.5. The spectrum also showed evidence of considerable fragmentation of the cores during ionization, implying that these clusters may be less stable than their aromatic analogs. This is shown by the rising mass peak near 20 kDa with a maxima near 17 kDa (not shown) and a complex fragmentation pattern near 10 kDa from secondary fragmentation of the $Au_xS_y^-$ ions (not shown).[7]

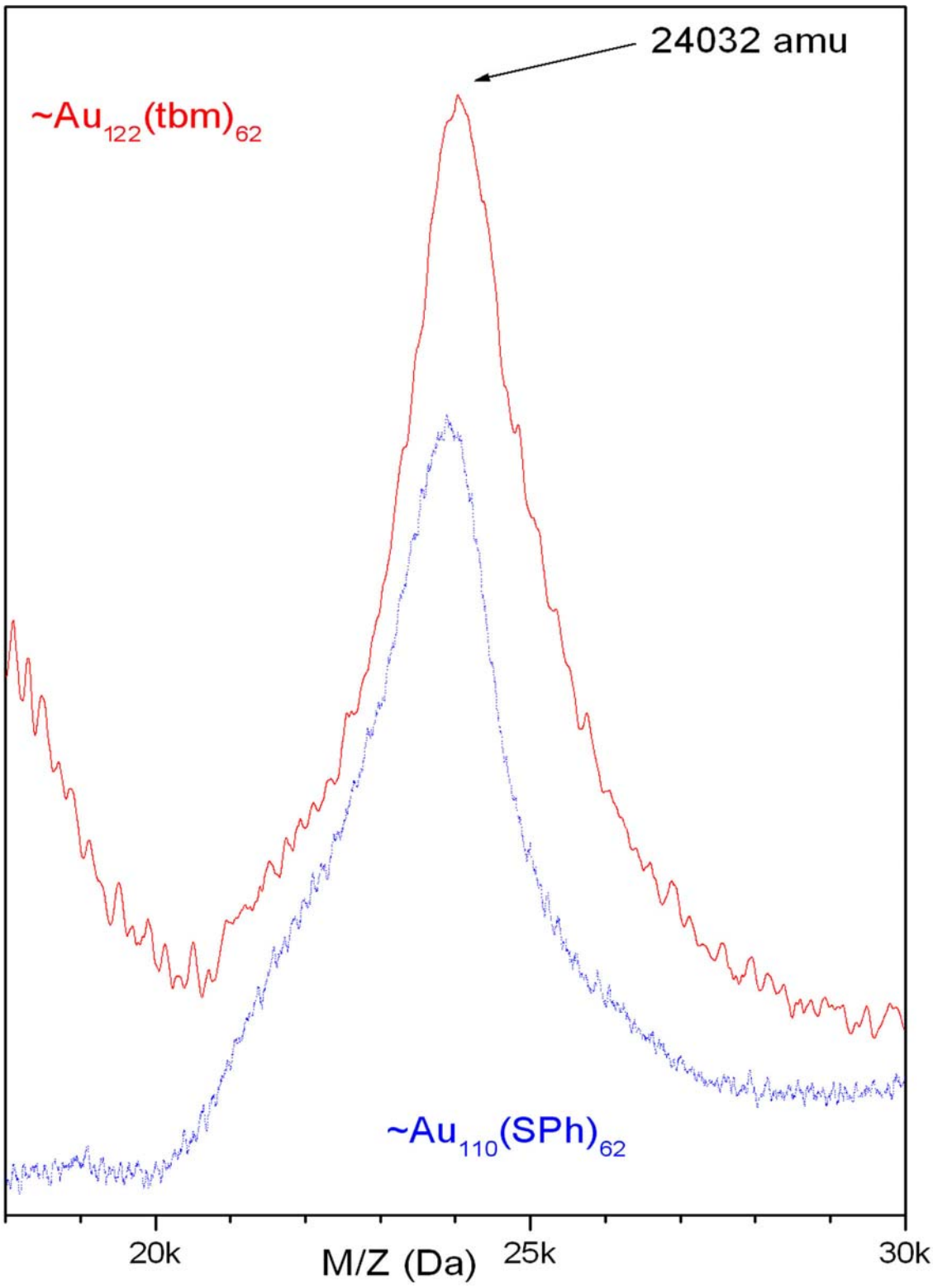


Figure 5.5 MALDI mass spectrum of $Au_x(tbm)_y$ MPCs (red) and ~$Au_{110}(SPh)_{62}$ (blue)**.** The two peak widths at half max are nearly identical**,** signifying the same number of surface-bound sulfur atoms. The spectral peak center of $Au_x(tbm)_y$ is indicated at the top.

5.2.4 ^{1}H-NMR Spectroscopy

The ^{1}H-NMR spectrum of ~$Au_{122}(tbm)_{62}$ should be quite simple given that tert-butylthiolate possesses 9 equivalent alkyl hydrogens with a 1.43 ppm chemical shift.[8] The broadening and loss of sharp spectral features characteristic of $Au_x(alkylthiolate)_y$ is quite noticeable in the spectrum of these clusters (Figure 5.6). The sharp alkyl resonances at .88, 1.28, 1.43, and 1.55 ppm indicate that TOA^+ is also present in the clusters, lacking only the α-methylene resonances normally observed in TOABr at 3.1 ppm (see Figure 2.16 for reference). The convolution of the tbm and TOA^+ spectral peaks prevented a

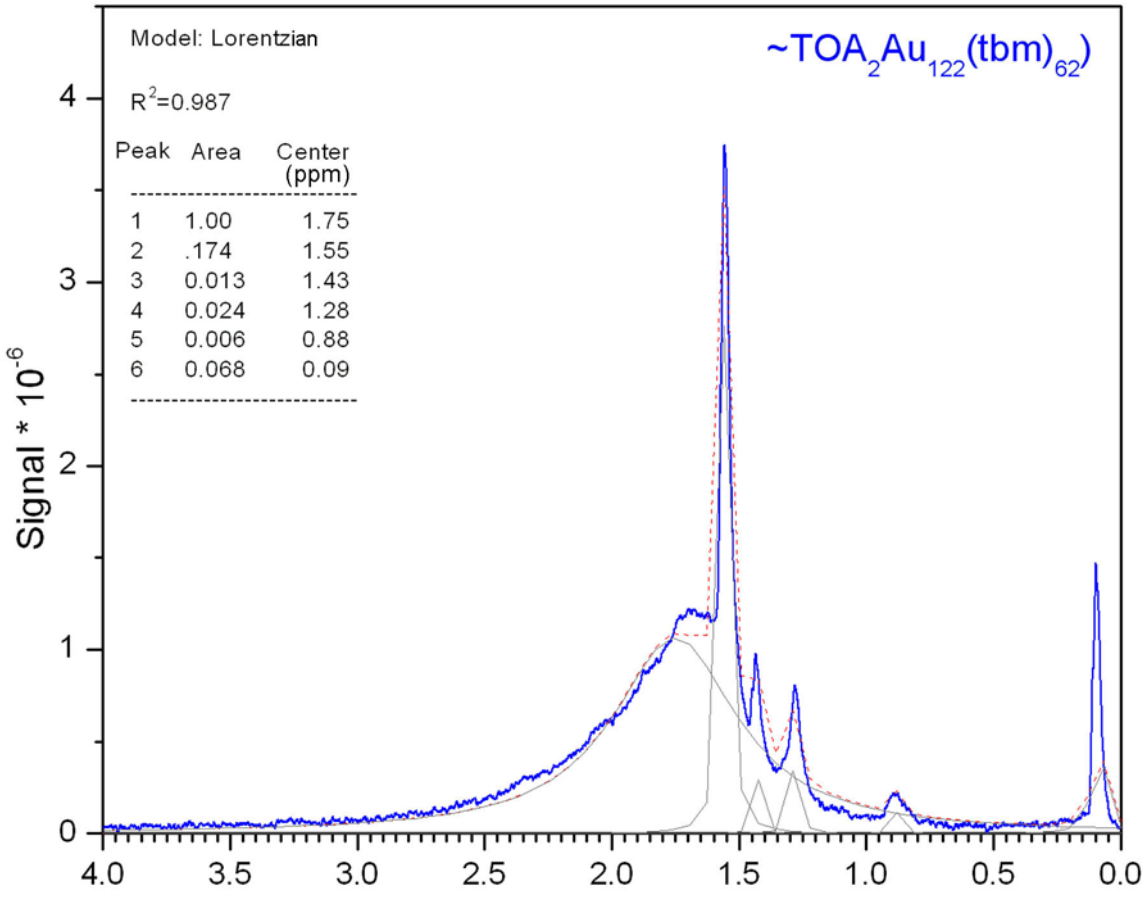


Figure 5.6 ^{1}H-NMR spectrum of ~$TOA_2[Au_{122}(tbm)_{62}]$. The spectral peaks were estimated with a six peak Lorentzian function, shown as a red dotted line. Individual peaks are in gray. The peak at .09 ppm is the ubiquitous peak of vacuum grease (polydimethylsiloxane). The peak areas estimate 100 hydrogens for the broad tbm feature and 22 hydrogens for the hydrogens of TOA (excluding α methylenes). Multiplying these values by 5.58 yields 62:2 ratio of tert-butyl mercaptan to TOA^+. Spectra were collected at <100 μM in dueterated dichloromethane.

simple integration of the peak areas to determine the tbm:TOA^+ ratio, so a Lorentzian peak fit was applied with Origin Software by Microcal to obtain an estimate of 62 tbm to 2 TOA^+. The ^{1}H-NMR spectrum was collected as detailed in Chapter 2.

The presence of TOA^+ in these Au_x(alkylthiolate)$_y$ MPCs implies that other MPCs generated in the presence of TOABr may also be anionic cores charge balanced by TOA^+ cations. This new understanding of gold MPCs has only recently been reported for the $Au_x(SPh)_y$ clusters.[10] Many of the alkanethiolate clusters discussed in Chapter 1 may contain TOA^+ counteractions which would be difficult to distinguish from linear alkanes by ^{1}H-NMR. It could definitely contribute to the negatively charged "as prepared" state of Au_x(alkylthiolate)$_y$ MPCs noted by Murray et. al, although they favor the notion that TOABr is adsorbed intact on the clusters.[4,11] If this were the case, it is unlikely that the stoichiometry of such species would be consistent between different synthetic batches of clusters, as detailed in Chapter 2. This knowledge should facilitate crystallization attempts, presuming conditions whereby rigid cations, such as tetraphenylphosphonium bromide (TPPBr), can be used to generate $TPP_NAu_x(SPh)_y$ MPCs that are anticipated to have good crystallization properties within pure samples.

5.2.5 Infrared Spectroscopy

Infrared spectroscopy of the $TOA_2[Au_{122}(tbm)_{62}]$ MPCs yields little new insight about the clusters, but is included for completeness. The FTIR spectrum of these clusters shares features with both tert-butylmercaptan (tbm) and tetraoctylammonium (TOA^+), further confirming their presence. The clusters clearly lack the ~2560 cm^{-1} S-H stretching vibration of tbm. Figure 5.7 shows the FTIR spectrum of the MPCs with tbm and TOABr for comparison. The strong absorbance peaks of TOA+ between 900 and 1200 cm^{-1} are clearly prevalent in the MPC spectrum as are the characteristic methyl absorbances of tbm between 2800 and 3100 cm^{-1}.

5.2.6 Summary

This chapter demonstrates 1.5 nm core diameter gold MPCs or “quantum dots” can be generated and isolated using a well established procedure by simply choosing an appropriate thiol, such as tert-butylmercaptan (tbm). The MPC cores have properties similar to other clusters of this core size and show clear evidence by ^{1}H-NMR that TOA^+ is present in the clusters, most likely as a counter cation to $[Au_{122}(tbm)_{62}]$ anionic cores. The clusters have accurately estimated compositions and are non-colloidal. They are inherently less stable than clusters passivated by linear alkanethiolates or benzenethiolate, as even dried MPs degrade within a month due to the lability of tbm. This may actually be an asset for the production of small gold MPCs passivated by thiols that are incompatible with the strong reducing conditions normally employed to generate gold clusters (as discussed in Chapter 4.2).

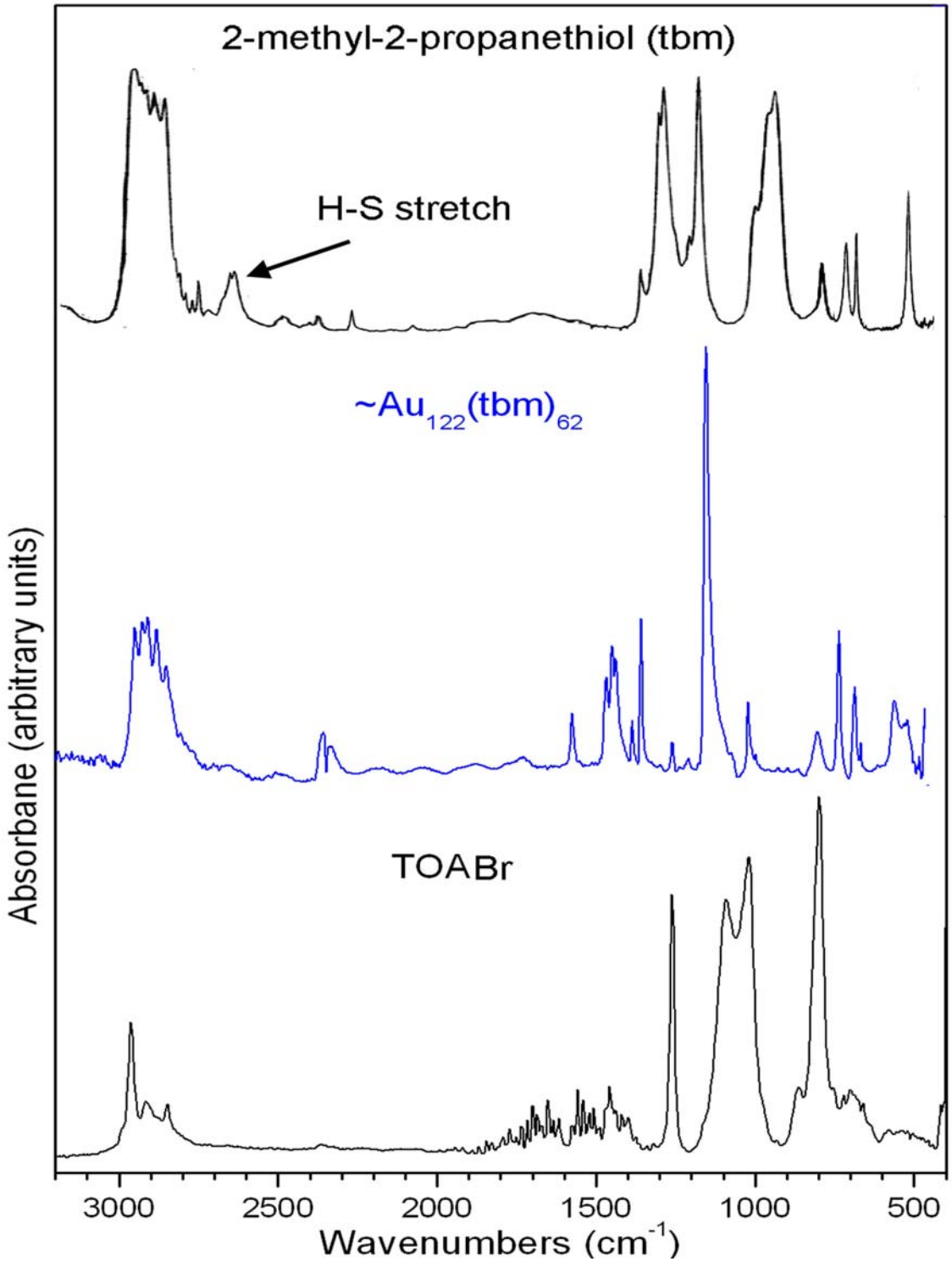


Figure 5.7 FTIR spectrum of $Au_x(tbm)_y$ MPCs with reference materials. Tert-butylmercaptan (2-methyl-2-propanethiol) spectrum adapted from reference 11.

Chapter 5 References

(1) Brust, M.; Walker, M.; Bethell, D.; Schiffrin, D.; Whyman, R. *J. Chem. Soc., Chem. Comm.* **1994**, *7*, 801

(2) Schaaff, G.; Shafigullin, M.; Khoury, J.; Vezmar, I.; Whetten, R. *J. Phys. Chem. B* **2001**, *105*, 8785

(3) Lee, D.; Donkers, R.; Wang, G.; Harper, A.; Murray, R. *J. Am. Chem. Soc.* **2004**, *126*, 6193

(4) Donkers, R.; Lee, D.; Murray, R. *Langmuir*, **2004**, *20*, 1945

(5) Donkers, R.; Song, Y.; Murray, R. *Langmuir*, **2004**, *20*, 4703

(6) Schaaff, G.; Shafigullin, M.; Khoury, J.; Vezmar, I.; Whetten, R.; Cullen, W>; First, P.; Gutierrez-Wing, C.; Ascensio, J.; Jose-Yacaman, M. *J. Phys. Chem. B* **1997**, *101*, 7885

(7) Schaaff, T. *Anal. Chem.* **2004**, *76*, 6187

(8) Pouchert, C.; Behnke, J. *The Aldrich library of ^{13}C and ^{1}H FT NMR Spectra Ed. 1.* **1993** Aldrich Chemical Co.

(9) Price, R.; Whetten, R. *J. Am. Chem. Soc.* **2005**, *127*, 13750

(10) Pietron, J.; Hicks, J.; Murray, R. *J. Am. Chem. Soc.***1999**, *121*, 5565

(11) Pouchert, C. *The Aldrich library of FT-IR spectra Ed. 2.* **1997** Aldrich Chemical Co.

CHAPTER 6

CONCLUSIONS

The goal of this report was to provide detailed instructions for the preparation of thiolate monolayer protected clusters (MPCs) containing fewer than 200 core gold atoms. The highest level of characterization necessary is provided to show they are discrete molecular compounds similar in molecular weight to proteins ranging 12 to 40 kDa. Their optical spectra are clearly size dependent below 2.0 nanometer core diameter, displaying electronic energy level quantization analogous to semiconductor quantum dots (QDs). The precise effect core structure, ligand shell, and charge state play in determining the electronic properties of gold QDs has yet to be resolved, but a crystal structure for any small gold cluster with 18 to 200 atoms would expedite this understanding, allowing construction of better theoretical models.

This work sought to produce a $Au_x(SPh)_y$ cluster suitable for crystallization based on the successful structural determination of the similarly passivated $Cd_{32}S_{14}(SPh)_{36}*DMF_4$ quantum dot.[1] Previous efforts in our laboratory had failed to produce cores below 2.0 nm with a benzenethiolate protective monolayer.[2] The seemingly simple step of changing the reaction solvent from toluene to dichloromethane provided the means to generate benzenethiolate passivated gold quantum dots of mostly 1.5 nm diameter that were readily separable from the 1.7 nm core minor reaction product. Attempts to purify the MPCs allowed the discovery that 1.5 to 2.5 nm gold MPCs can be oxidatively etched to produce smaller, more robust cores of 1.1 nm in the case of $Au_x(SPh)_y$ and perhaps even smaller cores in the case of Au_x(dodecanethiolate)$_y$ clusters.

It was serendipitously discovered through rigorous analysis and against the prevalent paradigm that all of the clusters were actually $[Au_x(SPh)_y]$ anions charge balanced by tetraoctylammonium (TOA^+) cations.[3] This surprising knowledge led to the production of gold clusters passivated with tert-butylmercaptan, which has a similar steric hindrance to benzenethiol and produces mostly 1.5 nm core MPCs as well. These alkanethiolate protected gold quantum dots also contained TOA^+ as a countercation, strongly suggesting that all Au MPCs may be anionic. This is certainly not unreasonable given that most preparations of non-colloidal gold clusters utilize ten equivalents of reducing agent per gold atom present. The primary evidence for this insight came from ^{1}H-NMR spectroscopy, yielding consistent ratios of TOA^+ within the samples, rather than random amounts indicative of contamination. The 1.1 nm $TOA_2[Au_{44}(SPh)_{28}]$ cluster actually possesses a mass spectral parent peak consistent with $TOA[Au_{44}(SPh)_{28}]^-$, with exclusion of the 467 amu mass of TOA^+ preventing identification of the parent peak. Additionally, the first ever Raman spectra of benzenethiolate on size-quantized gold cores were collected to better understand gold-thiolate bonding in these materials. The spectra indicate the 1.5 nm $\sim TOA_{4\text{-}6}[Au_{110}(SPh)_{62}]$ MPCs may contain bound disulfide-like species, whereas the 1.7 nm cores do not, showing the cluster surface area may influence the thiolate surface binding.

It is hoped this work will prompt the generation of $(PPh_4)_N[Au_x(SPh)_y]^{N-}$ clusters, although other rigid cations may be suitable. Such a nanocrystalline salt should possess enhanced crystallinity relative to clusters containing tetraoctylammonium. While structural models fitting powder x-ray patterns of gold MPCs strongly suggest decahedral core structures[4], higher symmetry structures are known for small clusters such as

$(AsPh_4)_4[Pt_{44}(CO)_{47}]^{4-}$ and $(AsPh_4)_4[Pt_{38}(CO)_{44}]^{2-}$ and may prove valid for gold quantum dots.[5]

Chapter 6 References

(1) Herron, N.; Calabrese, J.; Farneth, W.; Wang, Y. *Science* **1993**, *259*, 1426

(2) Schaaff, G.; Shafigullin, M.; Khoury, J.; Vezmar, I.; Whetten, R. *J. Phys. Chem. B* **2001**, *105*, 8785

(3) Price, R.; Whetten, R. *J. Am. Chem. Soc.* **2005**, *127*, 13750

(4) Cleveland, C.; Landman, U.; Schaaff, T.; Shafigullin, M.; Stephens, P.; Whetten, R. *Phys. Rev. Lett.* **1996**, *79*, 1873

(5) Roth, J.; Lewis, G.; Safford, L.; Jiang, X.; Dahl, L.; Weaver, M. *J.Am. Chem. Soc.* **1992**, *114*, 6159

APPENDIX

PRESENTATION OF OPTICAL AND X-RAY DATA

A.1 Optical Absorbance Spectra

The optical absorbance spectra presented were all initially collected in equal intervals of wavelength, typically from 1100 to 200 nm. To allow a more natural comparison to band structure or charging energies within the metallic cores, the spectral wavelengths were converted to energy. Since the conversion from wavelength to energy is reciprocal, rather than linear ($1\ eV = 1239.84\lambda^{-1}$), the data must be presented in a consistent and physically relevant manner.[1] The optical absorbance points are typically at equally spaced intervals in wavelength, which define absorbance as a function of wavelength, this function can be denoted as $A(\lambda)$, with units of cm^2 per mole. For an integrated optical absorbance band within an interval from λ_1 to λ_2, the plot area is expressed by following integral:

$$f(\lambda_1, \lambda_2) = \int_{\lambda_1}^{\lambda_2} A(\lambda) d\lambda$$

Photon wavelength is converted into photon energy by the relation $\lambda = hcE^{-1}$. This substitution makes $-d\lambda = hcE^{-2}dE$, thus when substituted into the previous expression, the integral necessarily becomes:

$$f(E_1, E_2) = \int_{E_1}^{E_2} \frac{A(E)}{E^2} d$$

This correction is implemented by simply dividing the absorbance at a given energy by that energy in units of eV^2, thereby preserving the relative peak areas in the energy spectrum from the original wavelength spectrum. This correction is noted on the y-axis label of every optical spectral plot in this work.

A.2 Powder Diffraction Patterns

X-ray diffraction data for colloids and microcrystalline samples are often displayed as plots of 2θ, with all diffractions peaks from bulk present and visible. This allows direct size estimation by the Scherrer formula, but is not applicable to small clusters, such as those within this work. Considerable size broadening due to size effects is evident in the diffraction patterns and the clusters may posses a five-fold decahedral symmetry composed of ~6 atomic layers, thus simple Bragg diffraction is applied to estimate size. This is achieved by converting the 2θ values into scattering vector amplitudes by the relation:

$$s = \frac{2\sin\theta}{\lambda}$$

where θ = half of 2θ and λ is the wavelength of the x-rays diffracted (.15406 nm). The scattering intensity at a given s value is multiplied by s to eliminate any peak asymmetry, followed by fitting Gaussian functions to the peaks with Microcal Origin software to minimize error.

Diffraction peaks observed at a given s value in the large angle region are readily indexed to the Miller indices (crystalline planes) giving rise to their intensity by the relation:

$$s = s_0 + a^{-1}(h^2 + k^2 + l^2)^{1/2}$$

where s_0 is a free parameter correcting for zero-angle offset and vertical sample displacement, *a* is the lattice constant (in nm) of the crystallite, and h,k,l are the Miller indices giving rise to each observed diffraction peak. This plotting method produces a series of diffraction peaks of similar width that are wavelength independent. Averaging the reciprocals of the peak widths at half maximum (FWHM) produces an average crystallite diameter. This methodology has been detailed previously[2-5]

Appendix References

(1) Khoury, J. *Ph.D. Dissertation* **1999**, *University of California Los Angeles*

(2) Schaaff, G.; Shafigullin, M.; Khoury, J.; Vezmar, I.; Whetten, R.; Cullen, W.; First, P. *J. Phys Chem. B* **1997**, *101*, 7885

(3) Whetten, R.; Shafigullin, M.; Khoury, J.; Schaaff, G.; Vezmar, I.; Alvarez, M.; Wilkinson, A. *Acc. Chem. Res.* **1999**, *32*, 397

(4) Schaaff, G.; Shafigullin, M.; Khoury, J.; Vezmar, I.; Whetten, R.; *J. Phys Chem. B* **2001**, *101*, 8785

(5) Shafigullin, M. *Ph.D. Thesis* **1999**, *Georgia Institute of Technology*